TU Delft

Delft University of Technology

Document Version
Final published version

Citation (APA)
Li, Z. (2026). *Solid-State Transformers for Large-Scale H2 Electrolyzers*. [Dissertation (TU Delft), Delft University of Technology]. https://doi.org/10.4233/uuid:0a07f422-83d1-40d1-b97c-939a227cd009

Important note
To cite this publication, please use the final published version (if applicable).
Please check the document version above.

Copyright
In case the licence states “Dutch Copyright Act (Article 25fa)”, this publication was made available Green Open Access via the TU Delft Institutional Repository pursuant to Dutch Copyright Act (Article 25fa, the Taverne amendment). This provision does not affect copyright ownership.
Unless copyright is transferred by contract or statute, it remains with the copyright holder.

Sharing and reuse
Other than for strictly personal use, it is not permitted to download, forward or distribute the text or part of it, without the consent of the author(s) and/or copyright holder(s), unless the work is under an open content license such as Creative Commons.

Takedown policy
Please contact us and provide details if you believe this document breaches copyrights.
We will remove access to the work immediately and investigate your claim.

This work is downloaded from Delft University of Technology.

Solid-State Transformers for Large-Scale H_2 Electrolyzers

Zhengzhao Li

Solid-State Transformers for Large-Scale H_2 Electrolyzers

Solid-State Transformers for Large-Scale H_2 Electrolyzers

Dissertation

for the purpose of obtaining the degree of doctor
at Delft University of Technology,
by the authority of the Rector Magnificus Prof. dr. ir. H. Bijl,
chair of the Board for Doctorates,
to be defended publicly on
Thursday 19 February 2026 at 12:30 o'clock

by

Zhengzhao LI

This dissertation has been approved by the promotors.

Composition of the doctoral committee:

Rector Magnificus,	chairperson
Prof. dr. ir. P. Bauer,	Delft University of Technology, promotor
Dr. Z. Qin,	Delft University of Technology, promotor
Independent members:	
Prof. ir. P. T. M. Vaessen,	Delft University of Technology
Dr. ir. A. M. van Voorden,	Delft University of Technology
Prof. Dr.-Ing. M. Liserre,	Christian-Albrechts-Universität zu Kiel, Germany
Dr. ir. Y. Sun,	Eindhoven University of Technology, the Netherlands
Prof. dr. ir. A.H.M. Smets,	Delft University of Technology, reserve member
Other member:	
Dr. ir. M. Ghaffarian Niasar,	Delft University of Technology

ISBN 978-94-6518-242-1

An electronic version of this dissertation is available at
http://repository.tudelft.nl/.
Copyright © 2026 by Zhengzhao Li

Contents

Summary vii

Samenvatting xi

Abbreviation xv

1 Introduction 1
- 1.1 Background of Green Hydrogen . . . 1
- 1.2 FlexH2 Project and Solid-State Transformer Concept . . . 2
- 1.3 Existing Solid State Transformer Project . . . 5
- 1.4 Thesis Objective and Research Questions . . . 9
- 1.5 Major Contributions . . . 10
- 1.6 Outline of the Thesis . . . 10

2 Topology Evaluation of Solid-State Transformers for Hydrogen Electrolyzers 13
- 2.1 Introduction . . . 14
- 2.2 Performance Metrics for MMC-SST . . . 16
  - 2.2.1 Parameter Design of the Complete System . . . 17
  - 2.2.2 Thermal Modelling and Loss Estimation of Power Converters . . . 19
  - 2.2.3 Size and Weight Estimation of MMC Converter . . . 20
  - 2.2.4 Design of the Medium-Frequency Transformer for MMC-SST . . . 23
  - 2.2.5 Performance Metrics at Different Frequencies . . . 32
- 2.3 Performance Metrics for MMR-SST . . . 34
  - 2.3.1 Loss, Size, and Weight Estimation of the Power Converters . . . 34
  - 2.3.2 Design of the Medium-Frequency Transformer for MMR . . . 39
  - 2.3.3 Performance Metrics at Different Frequencies . . . 40
- 2.4 Performance Metrics for ISOP-SST . . . 40
  - 2.4.1 Loss, Size, and Weight Estimation of the Power Converters . . . 40
  - 2.4.2 Design of the ISOP MFT . . . 43
  - 2.4.3 Performance Metrics at Different Frequencies . . . 44
- 2.5 Topologies Comparison Results . . . 45
  - 2.5.1 Frequency Sweep Analysis . . . 45
  - 2.5.2 Analysis of Topologies at Optimal Frequencies . . . 46
- 2.6 Conclusion . . . 47

3 Control Strategy for Enhanced Performance of MMR-SST 49
- 3.1 Introduction . . . 50
- 3.2 Basic Operation and Existing Control Method for MMR-SST . . . 52
  - 3.2.1 Fundamental Operation Principle . . . 52
  - 3.2.2 Existing Control Method . . . 54

3.3 Proposed Control Method for MMR-SST . . . 60
3.3.1 Proposed Modulation Method . . . 60
3.3.2 Gate Signal Generation and Overall Control Loop . . . 63
3.4 Simulation Results and Comparison with Previous Method . . . 70
3.4.1 Simulation Results . . . 70
3.4.2 Comparison with Phase-Shift Control Plus Discontinuous Modulation Index Control . . . 73
3.4.3 MMR Resonant Current THD Analysis of Two Control Methods . . . 76
3.5 Experimental Verification . . . 79
3.6 Conclusion . . . 87

4 Data-Driven Modeling of Magnetic Losses for SST Design Optimization 89
4.1 Introduction . . . 90
4.2 Provided Dataset and Proposed Neural Network . . . 92
4.2.1 MagNet Challenge Provided Dataset . . . 93
4.2.2 Proposed FFT+FNN Method . . . 95
4.2.3 Training Process of the Proposed Method . . . 96
4.2.4 Design of Input Layer . . . 98
4.3 Comparison with the State of the Art . . . 100
4.3.1 Sequence-to-Scalar: LSTM + FNN Model . . . 100
4.3.2 Sequence-to-Sequence: Encoder-Projector-Decoder Model . . . 100
4.3.3 Comparison Results and Analysis . . . 102
4.4 Multi-Objective Optimization, Transfer Learning and Comparison . . . 103
4.4.1 Multi-Objective Optimization . . . 103
4.4.2 Transfer Learning . . . 107
4.4.3 Results with and without Transfer Learning Comparison . . . 108
4.5 Conclusion . . . 112

5 Conclusion 113
Recommendations for Future Work . . . 115

Bibliography 117

Curriculum Vitæ 131

List of Publications 133

Acknowledgments 135

Summary

The increasing urgency of global decarbonization has accelerated the transition toward renewable-based energy systems. Among various technological pathways, green hydrogen has emerged as a critical energy vector due to its potential for large-scale storage and carbon-neutral applications. However, the current production of hydrogen remains largely dependent on fossil fuels, which undermines its environmental benefits and long-term sustainability. To fully realize the promise of green hydrogen, scalable and efficient power conversion systems are needed to interface renewable energy sources with electrolyzer systems.

In particular, large-scale onshore hydrogen production requires power conversion systems that are compact, modular, and capable of operating at medium to high voltage levels. Solid-state transformers (SSTs), which employ medium-/high-frequency galvanic isolation and integrated power electronic converters, provide a promising solution to meet these requirements. Compared to conventional line-frequency transformers, SSTs enable reduced volume and weight and enhanced controllability. This thesis investigates the optimal design, control strategy development, and loss modeling of solid-state transformers tailored for hydrogen electrolyzer systems, addressing key challenges in topology selection, loss estimation, and system performance optimization.

Topology Evaluation of Solid-State Transformers

In hydrogen electrolyzer systems, the power converter must efficiently step down medium-voltage AC to low-voltage DC while meeting stringent constraints on volume and weight. Conventional solutions based on line-frequency transformers are excessively bulky and therefore unsuitable for compact installations. To overcome these limitations, this thesis evaluates three representative solid-state transformer (SST) topologies, each exhibiting different characteristics in terms of size, weight, and loss performance.

The selected topologies include: (1) the Input-Series Output-Parallel (ISOP) structure employing cascaded LLC converters; (2) the Modular Multilevel Converter (MMC)-based SST with a central medium-frequency transformer; and (3) the Modular Multilevel Resonant (MMR)-based SST, which incorporates resonant elements to reduce switching losses. Each topology is designed at the component level, with particular attention to insulation requirements and thermal management.

Detailed estimations of size, weight, and power loss are conducted for each topology. Semiconductor and magnetic losses are calculated using analytical equations and FEM-based simulations, while insulation requirements and chiller design are incorporated to enable realistic volumetric assessments. A frequency sweep is performed to identify the optimal operating frequency for each topology, balancing loss minimization and size/weight reduction.

Comparative results reveal that each SST topology presents distinct trade-offs in efficiency, size, and weight. The ISOP-SST is advantageous in space-constrained scenarios,

while the MMR-SST offers benefits in weight-sensitive applications. Centralized transformer designs generally lead to smaller and lighter transformer units. Moreover, reducing the number of submodules significantly contribute to compact converter design. Overall, the proposed evaluation framework provides a scalable methodology for diverse application requirements.

Control Strategy for Enhanced Performance of MMR-SST

For medium-voltage hydrogen electrolyzer systems, the control strategy of the solid-state transformer significantly affects power conversion efficiency, current quality, and thermal performance. In particular, the Modular Multilevel Resonant based SST topology presents unique opportunities for efficiency improvement by enabling soft-switching operation and multilevel voltage control. However, existing control methods often involve complex multi-loop structures and introduce substantial resonant current distortion due to high phase shift angles of the trapezoidal modulation waveform.

To address these challenges, this work proposes a simplified modulation scheme based on continuous modulation index control with a double-step staircase waveform. The control strategy operates at the resonant frequency, which allows the transformer to be designed with a larger magnetizing inductance, thereby reducing magnetizing current. Additionally, the fixed low phase shift angle among submodules significantly decreases resonant current distortion, resulting in improved current quality and lower switching losses.

The proposed control method is validated through both simulation and experimental results. Simulation results demonstrate improved overall efficiency and reduced total harmonic distortion in the resonant current. These improvements result in lower power loss, reducing the cooling system burden and contributing to overall system compactness. By simplifying the control loop structure while achieving comparable voltage regulation capability, this method provides a scalable and effective solution for MMR-based SSTs in hydrogen electrolyzer applications.

Data-Driven Modeling of Magnetic Losses for SST Design Optimization

Accurate modeling of magnetic losses is critical for the cooling design of transformer and inductor in SST systems, especially under medium-/high-frequency and variable operating waveform conditions. Traditional approaches based on empirical Steinmetz equations require large design margins due to limited prediction accuracy. To overcome this limitation, this work explores data-driven methods using neural networks to directly estimate magnetic losses from waveform and frequency data, offering a more precise and scalable modeling approach.

A feedforward neural network (FNN) architecture is proposed, utilizing the harmonic components of the flux density waveform obtained through Fast Fourier Transform (FFT). This input formulation effectively captures waveform shape characteristics while maintaining low model complexity. Furthermore, a multi-objective optimization (MOO) framework is implemented using Optuna to balance accuracy and parameter count, resulting in models with competitive accuracy and reduced training requirements. Compared with advanced

models such as LSTM and encoder-decoder architectures, the FFT+FNN model achieves comparable accuracy with significantly lower computational cost.

To address the challenge of limited data for new magnetic materials, transfer learning is incorporated into the modeling workflow. By reusing knowledge learned from well-characterized materials, the prediction accuracy for data-scarce materials is significantly improved with minimal increase in model complexity. Overall, this data-driven modeling framework enhances the accuracy of magnetic components power loss predictions.

Samenvatting

De toenemende urgentie van wereldwijde decarbonisatie heeft de overgang naar energiesystemen op basis van hernieuwbare bronnen versneld. Onder de verschillende technologische routes is groene waterstof naar voren gekomen als een cruciale energiedrager vanwege de potentie voor grootschalige opslag en koolstofneutrale toepassingen. De huidige productie van waterstof is echter grotendeels afhankelijk van fossiele brandstoffen, wat de milieuwinst en de duurzaamheid op lange termijn ondermijnt. Om de potentie van groene waterstof volledig te benutten, zijn schaalbare en efficiënte vermogensconversiesystemen nodig om hernieuwbare energiebronnen te koppelen aan elektrolysesystemen.

In het bijzonder vereist grootschalige waterstofproductie op land compacte en modulaire vermogensconversiesystemen die geschikt zijn voor bedrijfsspanningen in het midden- tot hoogspanningsbereik. Solid-state transformatoren (SST's), die gebruik maken van galvanische scheiding op middel-/hoogfrequentie en geïntegreerde vermogenselektronica, bieden een veelbelovende oplossing voor deze eisen. In vergelijking met conventionele transformatoren op netfrequentie maken SST's een lager volume en gewicht mogelijk, evenals verbeterde regelbaarheid. Dit proefschrift onderzoekt het optimale ontwerp, de regelstrategie en het verliesmodel van SST's voor elektrolysetoepassingen, waarbij belangrijke uitdagingen worden aangepakt zoals topologiekeuze, inschatting van de verliezen en prestatieverbetering van het systeem.

Topologie-evaluatie van solid-state transformatoren

In elektrolysesystemen moet de vermogensomzetter efficiënt de middenspanning-AC omzetten naar een laagspanning-DC, terwijl strikte eisen aan volume en gewicht worden nageleefd. Conventionele oplossingen op basis van netfrequentietransformatoren zijn te omvangrijk en daardoor ongeschikt voor compacte installaties. Om deze beperkingen te overwinnen, evalueert dit proefschrift drie representatieve SST-topologieën, elk met verschillende eigenschappen op het gebied van grootte, gewicht en vermogensverlies.

De geselecteerde topologieën zijn: (1) de Input-Series Output-Parallel (ISOP)-structuur met cascaderende LLC-converters; (2) de Modular Multilevel Converter (MMC)-gebaseerde SST met een centrale transformator op middenfrequentie; en (3) de Modular Multilevel Resonant (MMR)-gebaseerde SST, waarin resonante componenten zijn geïntegreerd om de schakelverliezen te verminderen. Elke topologie is op componentniveau ontworpen, met bijzondere aandacht voor isolatie-eisen en thermisch beheer.

Gedetailleerde schattingen van grootte, gewicht en vermogensverlies zijn uitgevoerd voor elke topologie. Halfgeleider- en magnetische verliezen zijn berekend met behulp van analytische vergelijkingen en FEM-simulaties, terwijl isolatie- en koelsysteemontwerp zijn geïntegreerd voor realistische volumeschattingen. Een frequentiesweep is uitgevoerd om de optimale werkfrequentie te bepalen, waarmee een balans wordt gevonden tussen het minimaliseren van verliezen en het verminderen van grootte en gewicht.

Vergelijkende resultaten tonen aan dat elke SST-topologie specifieke afwegingen kent in efficiëntie, afmetingen en massa. De ISOP-SST is voordelig in ruimtes met beperkte installatieruimte, terwijl de MMR-SST voordelen biedt in gewichtskritische toepassingen. Centrale transformatorontwerpen leiden over het algemeen tot kleinere en lichtere transformatoren. Daarnaast draagt het verminderen van het aantal submodules aanzienlijk bij aan een compact ontwerp. Het voorgestelde evaluatiekader biedt daarmee een schaalbare methode voor uiteenlopende toepassingen.

Regelstrategie voor verbeterde prestaties van MMR-SST

Voor elektrolysesystemen op middenspanning beïnvloedt de regelstrategie van de SST aanzienlijk de conversie-efficiëntie, stroomkwaliteit en thermische prestaties. In het bijzonder biedt de Modular Multilevel Resonant (MMR)-gebaseerde SST-topologie unieke mogelijkheden voor efficiëntieverbetering dankzij soft-switching en multilevel spanningsregeling. Bestaande regelmethoden zijn echter vaak complex door meerdere regelkringen en veroorzaken aanzienlijke vervorming van de resonantiestroom vanwege hoge faseverschuivingshoeken in de trapeziumvormige modulatiegolfvorm.

Om deze uitdagingen aan te pakken, wordt in dit werk een vereenvoudigd modulatieschema voorgesteld op basis van continue modulatie-indexregeling met een dubbele trapvormige golfvorm. De regelstrategie werkt bij de resonantiefrequentie, waardoor de transformator met een grotere magnetiserende inductantie kan worden ontworpen, wat leidt tot lagere magnetiserende stromen. Daarnaast vermindert een vaste, lage faseverschuiving tussen submodules de resonantiestroomvervorming, wat resulteert in een betere stroomkwaliteit en lagere schakelverliezen.

De voorgestelde regelmethode is gevalideerd via simulaties en experimentele resultaten. Simulaties tonen verbeterde algehele efficiëntie en verminderde harmonische vervorming van de resonantiestroom. Deze verbeteringen leiden tot minder vermogensverlies, waardoor de belasting op het koelsysteem afneemt en de algehele systeemcompactheid toeneemt. Door de regelstructuur te vereenvoudigen terwijl een vergelijkbare spanningsregeling behouden blijft, biedt deze methode een schaalbare en effectieve oplossing voor MMR-gebaseerde SST's in waterstofelektrolysetoepassingen.

Data-gedreven modellering van magnetische verliezen voor SST-ontwerpoptimalisatie

Nauwkeurige modellering van magnetische verliezen is essentieel voor het koelsysteemontwerp van transformatoren en inductoren in SST-systemen, vooral onder midden-/hoogfrequentieomstandigheden en variabele golfvormen. Traditionele methoden op basis van empirische Steinmetzvergelijkingen vereisen ruime ontwerpmarges vanwege beperkte nauwkeurigheid. Om deze beperking te overwinnen, worden in dit werk datagedreven methoden onderzocht waarbij neurale netwerken worden gebruikt om verliezen rechtstreeks te voorspellen op basis van golfvorm en frequentiegegevens.

Een Feedforward Neural Network (FNN)-architectuur wordt voorgesteld, waarbij gebruik wordt gemaakt van harmonische componenten van de fluxdichtheidsgolfvorm, verkregen via een snelle Fouriertransformatie (FFT). Deze inputformulering vat effectief de golfvormkarakteristieken samen met behoud van lage modelcomplexiteit. Verder wordt een multi-objectieve optimalisatie (MOO) uitgevoerd met Optuna, om een balans te

vinden tussen nauwkeurigheid en modelgrootte. Vergeleken met geavanceerde modellen zoals LSTM en encoder-decoder netwerken, bereikt het FFT+FNN-model een vergelijkbare nauwkeurigheid tegen aanzienlijk lagere rekenkracht.

Om het probleem van beperkte gegevens bij nieuwe magnetische materialen aan te pakken, wordt transfer learning toegepast in de modelleerstroom. Door gebruik te maken van kennis uit goed gekarakteriseerde materialen, wordt de nauwkeurigheid van voorspellingen voor nieuwe materialen met weinig gegevens aanzienlijk verbeterd zonder noemenswaardige toename in modelcomplexiteit. Deze data-gedreven modellering verbetert daarmee de nauwkeurigheid van het inschatten van de verliezen in magnetische componenten in SST-ontwerpen.

Abbreviation

CNN	Convolutional Neural Network
CTCs	Continuously Transposed Conductors
DAB	Dual Active Bridge
DRU	Diode Rectifier Unit
FEM	Finite Element Method
FFT	Fast Fourier Transform
FNN	Feedforward Neural Network
HF	High Frequency
IGSE	Improved Generalized Steinmetz Equation
IPOP	Input-Parallel Output-Parallel
IPOS	Input-Parallel Output-Series
ISOP	Input-Series Output-Parallel
LFT	Line-Frequency Transformer
LSTM	Long Short-Term Memory
M2DAB	Modular Multilevel Dual Active Bridge
MF	Medium Frequency
MFT	Medium-Frequency Transformer
MMC	Modular Multilevel Converter
MMR	Modular Multilevel Resonant Converter
MOO	Multi-Objective Optimization
MV	Medium Voltage
PI	Proportional-Integral
RES	Renewable Energy Sources
SE	Steinmetz Equation
SST	Solid-State Transformer
ZVS	Zero-Voltage Switching

1 Introduction

1.1 Background of Green Hydrogen

In recent years, although the global energy mix has begun to shift, fossil fuels remain the largest source of electricity generation. As of 2024, fossil fuels still accounted for approximately 60 % of global electricity generation, while renewable sources and nuclear power collectively contributed 40 % [1]. The continued reliance on fossil fuels remains a key contributor to global challenges, including climate change, environmental degradation, and air pollution. In addition, the finite availability and unequal geographical distribution of hydrocarbon resources continue to raise concerns regarding the long-term security and stability of energy supply [2].

To address these challenges, both academic and industrial communities have intensified efforts to develop low-carbon alternatives. In particular, the scientific community has devoted substantial effort to investigating pathways for transitioning from traditional energy systems to those primarily powered by renewable energy sources (RES). RES-based systems hold significant promise in mitigating the drawbacks of fossil fuels, particularly through the reduction of carbon emissions. Nonetheless, such systems face inherent limitations due to the intermittent and variable nature of renewable sources, leading to challenges in consistently balancing electricity supply and demand. To facilitate large-scale decarbonization while maintaining energy reliability, hydrogen is increasingly viewed as a critical enabler within renewable-integrated energy systems [3].

Recent bibliometric reviews tracking the development of the “Hydrogen Economy” highlight a sharp increase in scholarly publications over the past ten years [4]. Renewed interest in hydrogen has been driven by a combination of internal drivers and external pressures, such as the urgent need for global energy transition, falling renewable energy costs, and advances in related technologies [5].

Despite its promise, hydrogen’s current production landscape remains heavily fossil-fuel-dependent. As of 2023, less than 1% of global hydrogen production can be classified as low-emissions hydrogen, including blue and green hydrogen [6]. As depicted in Fig. 1.1, contemporary hydrogen generation primarily relies on steam methane reforming and coal gasification—techniques that yield “gray” and “brown” hydrogen, respectively [7]. Incorporating carbon capture into these processes can lead to the production of “blue”

1

hydrogen, which offers a relatively lower environmental impact. However, the most sustainable pathway involves generating "green" hydrogen via water electrolysis (WEl), using electricity sourced entirely from renewable energy systems (Fig. 1.2) [8]. Fig. 1.2 further outlines the infrastructure associated with green hydrogen logistics—such as transportation (via shipping, trucks, pipelines), storage—and its potential applications across key sectors including industry, transportation, heating, and electricity generation.

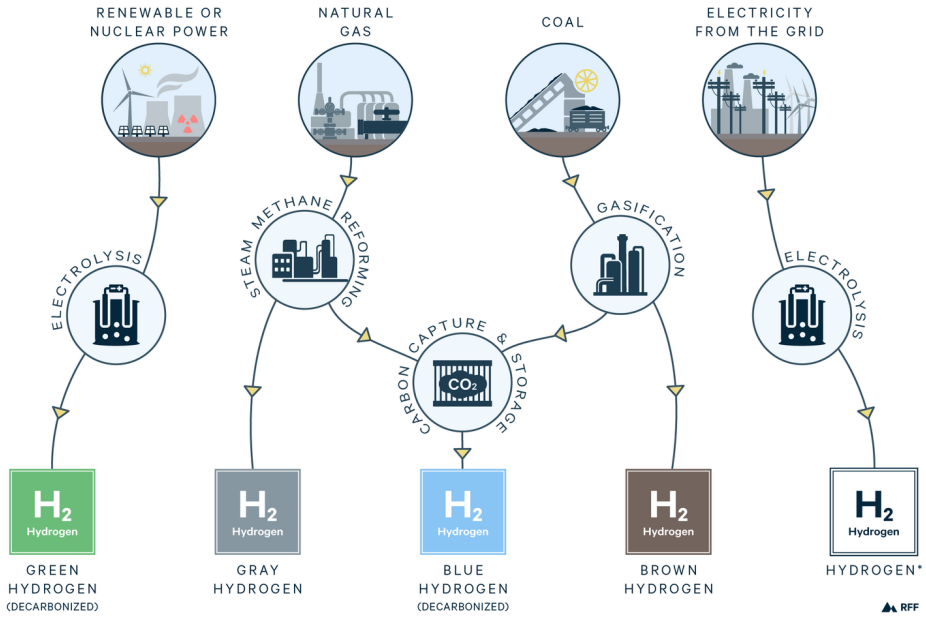


Figure 1.1: Overview of hydrogen production technologies and their classifications [7].

1.2 FlexH2 Project and Solid-State Transformer Concept

The increasing share of renewable energy, particularly offshore wind, presents significant challenges to grid stability and operation due to its inherent intermittency and limited forecasting accuracy. Without appropriate balancing strategies, the integration of large-scale renewables may either necessitate costly grid expansion or impose practical limits on their penetration, thereby threatening the Netherlands' CO_2 reduction targets [9].

Power-to-hydrogen is considered a promising solution to mitigate these challenges by converting excess renewable electricity into hydrogen, offering flexibility and long-term energy storage. In the Dutch context, both onshore and offshore hydrogen electrolysis are technically feasible pathways for utilizing offshore wind power. However, offshore electrolysis still requires further technological validation, particularly concerning spatial constraints and infrastructure deployment. In contrast, onshore electrolysis is comparatively mature and can be implemented at scale prior to 2030, as demonstrated by projects

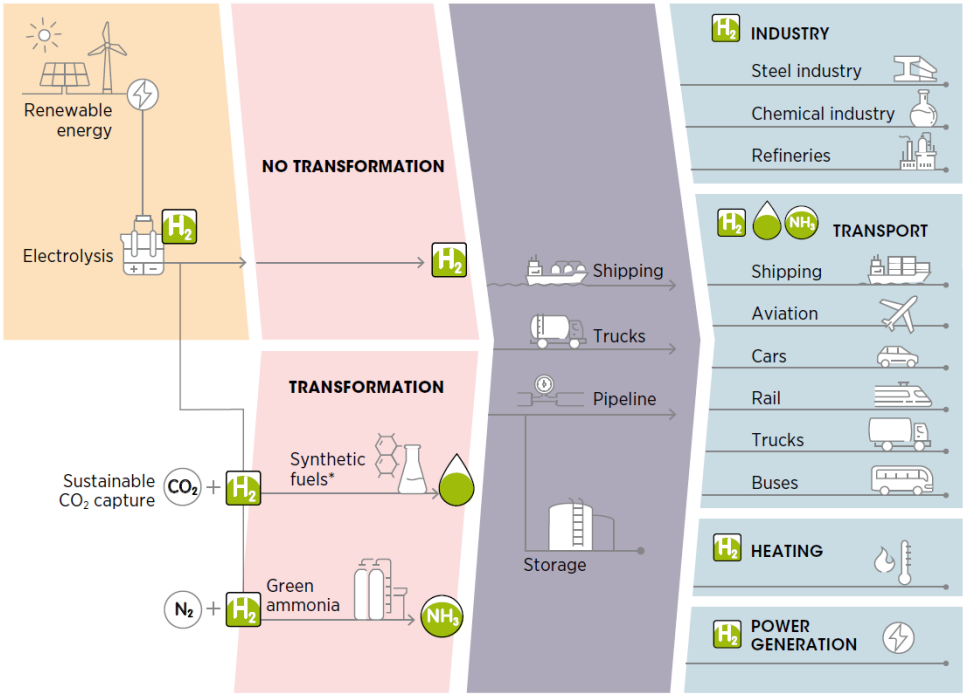


Figure 1.2: Green hydrogen: production, transport, and key applications [8].

like H-vision and NortH2. Moreover, onshore hydrogen production can benefit from the utilization of by-products such as oxygen and residual heat.

The FlexH2 project [10] addresses this integration challenge by linking offshore wind generation with onshore hydrogen production (see Fig. 1.3). The proposed system consists of three main components: (1) grid-forming offshore wind farms, (2) a high-performance solid-state transformer (SST) optimized for large-scale electrolyzers, and (3) a multi-terminal hybrid HVDC transmission network with integrated control. This thesis specifically focuses on the development and optimization of the second component—the solid-state transformer for hydrogen electrolyzer systems.

Traditional topologies for converting AC voltage into the DC voltage required by hydrogen electrolyzers typically employ line-frequency transformers combined with diode or thyristor rectifiers. Line-frequency transformers are static devices that have been deployed for over a century to transfer power at fixed grid frequencies (e.g., 50/60 Hz), offering high efficiency and low cost. However, their inherently low operating frequency results in large volume, making them unsuitable for applications where compactness is essential. This limitation is particularly relevant in densely populated and space-constrained countries such as the Netherlands.

In contrast, solid-state transformers utilize medium- or high-frequency transformer and power electronics to achieve galvanic isolation and power conversion across various voltage and frequency levels.

Increasing the operating frequency of a transformer enables a reduction in its physical

1

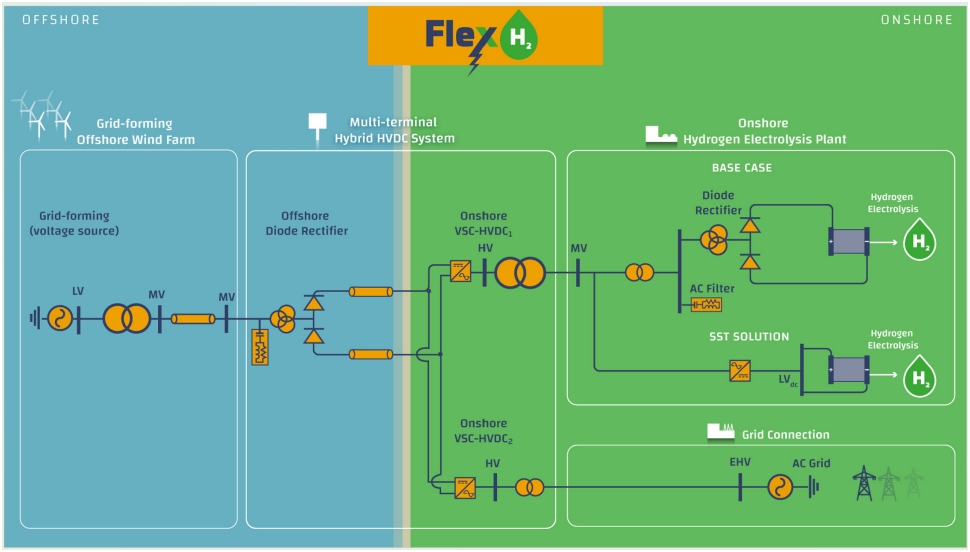


Figure 1.3: Overview of FlexH2 project.

volume and weight. This relationship can be derived from the area product expression, which establishes the relationship between the transformer's size and the amount of power it is designed to deliver. Specifically, the product of the magnetic core cross-sectional area A_{core} and the winding window area A_{Wdg} as shown in Fig. 1.4 is [11]:

$$A_{\text{core}} A_{\text{Wdg}} = \frac{\sqrt{2}}{\pi} \cdot \frac{P}{k_W J_{\text{rms}} \hat{B}_{\text{max}} f} \Rightarrow V \propto \left(A_{\text{core}} A_{\text{Wdg}}\right)^{3/4} \propto \frac{1}{f^{3/4}} \tag{1.1}$$

where f denotes the transformer's operating frequency, k_W is the winding window Utilization factor, J_{rms} is the winding current density and $\hat{B}_{\text{max}}$ is the peak core flux density. V denotes the overall transformer volume. Equation (1.1) illustrates that, for a given power level, increasing the operating frequency within a limit significantly reduces the required transformer volume. This characteristic is particularly valuable in applications with strict size and weight constraints, such as electric traction systems.

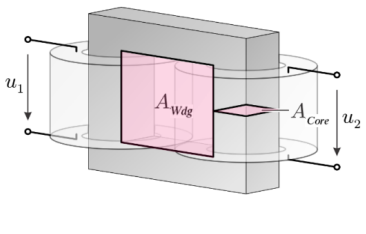


Figure 1.4: Illustration of the core cross-sectional area and the winding window area of the transformer [11].

As a result, SSTs offer compact size, increased power density, and enhanced functional flexibility, enabled by the integration of power electronics, allowing both DC and AC

operation across LV and MV networks. Unlike conventional transformers, SSTs are not direct replacements but rather advanced converters operating at medium-to-high frequencies, designed to meet modern power system demands such as advanced controllability and modular system architectures. In the context of SSTs, modularity primarily arises from architectures based on series–parallel combinations of power-electronic submodules, such as ISOP configurations, where system-level voltage and power ratings can be flexibly adjusted, while enabling continued operation in the presence of submodule failures.

To facilitate a more targeted design and analysis of the solid-state transformer investigated in this thesis—specifically within the context of large-scale hydrogen electrolyzer systems—the following Section provides a consolidated review of previously reported SST-based projects. Emphasis is placed on identifying representative implementations that highlight relevant technical parameters, application scenarios, and topological configurations. These selected cases serve as benchmarks to inform the subsequent design considerations.

1.3 Existing Solid State Transformer Project

Table 1.1 provides a comprehensive overview of real-world SST demonstrations and representative projects. It includes key information such as the associated institution, application scenario, voltage and power levels, adopted topology, and operating frequency. The application scenarios can be broadly categorized into railway systems, distribution power grids (primarily involving AC–AC conversion), DC grid interfaces (DC–DC conversion), electric vehicle (EV) chargers, hybrid grids with both AC and DC ports, and naval vessels. Most systems operate with medium-voltage input, and the majority are rated at the megawatt power level.

Two major topological categories are observed: cascaded structures, which incorporate multiple submodules and medium-frequency transformers, and MMC-based structures, typically employing a central transformer. These structural differences will be discussed in detail in Chapter 2. The reported operating frequency refers to the frequency of the medium-frequency transformer, which plays a critical role in determining the SST's size and weight. This frequency is not only influenced by the targeted power level but is also topology-dependent.

Though there are dozens of SST projects shown in Table 1.1, only a handful of them have shown size, weight, efficiency, and cost data comparison with the traditional line frequency transformer applications. The representative projects are detailed presented below.

The first SST demonstrators were mainly developed for railway applications, particularly before 2010. In conventional railway on-board electrical systems, low-frequency transformers operating at either 50 Hz or 16.7 Hz are commonly used for voltage step-down and galvanic isolation, depending on the region. While 50 Hz traction power systems are prevalent in most countries and offer relatively compact transformer designs, 16.7 Hz traction power systems—used in countries like Switzerland—require significantly bulkier and less efficient transformers. These conventional systems are typically oil-cooled, highly customized to specific train layouts, and operate at power levels below 15 MW [42].

A 1.5 MW e-Transformer prototype was developed by ALSTOM for 15 kV, 16.7 Hz railway applications in 2003 [12, 13]. Compared to a conventional tpology with 16.7 Hz

Table 1.1: Overview of Real-World SST Deployments

Project Name	Year	Institution	Application	Voltage	Power	Topology	Operating Freq.
E-Transformer [12, 13]	2003	Alstom	Railway	15 kV AC	1.5 MW	Cascaded	5 kHz
M^2LC [14]	2004	Siemens	Railway	15 kV AC	2 MW	MMC	10 kHz
MFT [15]	2007	Bombardier	Railway	15 kV AC	400 kVA	Cascaded	8 kHz
PECT [16]	2007	ABB	Railway	15 kV AC	1.2 MW	Cascaded	400 Hz
UNIFLEX-PM [17]	2009	UoN	Distribution power grids	3.3 kV AC	500 kVA	Cascaded	2 kHz
170 kVA SST [18]	2009	KTH	Railway	15 kV AC	170 kVA	Cascaded	4 kHz
SSPS [19]	2011	GE	Distribution power grids	13.8 kV AC to 268.5 V AC	1 MVA	Cascaded	20 kHz
DAB [20]	2013	RWTH Aachen	DC grid interface	5 kV DC to 5 kV DC	7 MW	Cascaded	1 kHz
PETT MV [21]	2014	ABB	Railway	15 kV AC	1.2 MVA	Cascaded	1.75 kHz
Fast charger for EVs [22, 23]	2016	Delta Electronics	EV charger	13.2 kV AC to 1 kV DC	400 kW	Cascaded	200 kHz
Swiss SST [24]	2018	ETH	Distribution power grids	6.6 kV AC to 400 V DC	25 kW	Cascaded	50 kHz
EPT [25]	2018	HUST	Distribution power grids	10 kV AC to 400 V AC	500 kVA	Cascaded	1 kHz
150 kW SST [26]	2018	Pusan National Univ.	Hybrid grids	13.2 kV AC to 0.75 kV DC	150 kW	Cascaded	10 kHz
HEART [27]	2019	Univ. of Kiel	Hybrid grids	10 kV AC to 0.4 kV AC	1 MVA	Not mentioned	20 kHz
MEGALink [28]	2019	ETH	Distribution power grids	10 kV AC to 0.4 kV AC	630 kVA	Cascaded	Not mentioned
PET [29]	2020	Tsinghua	Hybrid grids	10 kV AC and 10 kV DC input	1 MVA	Cascaded	30 kHz
TL-SRC [30]	2020	HIT	DC grid interface	2 kV DC to 0.75 kV DC	150 kW	Cascaded	10 kHz
PETT 3 kV [31]	2020	Gdańsk Univ.	Railway	3 kV DC	335 kVA	Cascaded	30 kHz
1 MW SST [32]	2020	TBEA Xinjiang	Hybrid grids	400-800 V DC to 10 kV AC	1 MW	Cascaded	20 kHz
Suzhou Tongli [33, 34]	2020	SGCC	Hybrid grids	10 kV AC and 380 V AC input	6 MVA	Cascaded	5 kHz
FUNDRESS [35]	2021	LAPLACE	Railway	1.8 kV DC	300 kW	Cascaded	15 kHz
DCSST [36]	2021	SGCC	DC grid interface	2 kV DC to 750 V DC	100 kW	Cascaded	10 kHz
LV Engine [37]	2022	UK Power Networks	Distribution power grids	11 kV AC to 0.4 kV AC	500 kVA	Shunt connection	20 kHz
ACT [38]	2022	ETH	DC grid interface	7 kV DC	166 kW	Cascaded	77.4 kHz
MUSE-SST [39]	2022	FREEDM	Naval vessels	4.16 kV AC to 0.48 kV AC	100 kW	Single module	20 kHz
TIGON [40]	2024	CIRCE	Hybrid grids	0.4 kV AC to 3 kV DC	300 kVA	Cascaded	83 kHz
ACDC [41]	2024	Eaton	DC grid interface	10 kV AC	2 MW	Cascaded	30 kHz

transformer, the prototype achieves a mass reduction of over 50 % (3.1 t vs. 6.8 t), while the total volume is 3.22 m^3. The system adopts a cascaded structure using 8 primary modules, followed by a multiwinding medium-frequency transformer and an output full-bridge converter to generate the DC voltage. The medium-frequency transformer operates at 5 kHz using ferrite cores and the e-Transformer achieves 94 % efficiency. However, the design involves a cost increase of approximately 50 % and faces reliability concerns due to the use of 48 high-voltage IGBTs on the primary side.

A 1.2 MVA medium-voltage power electronic traction transformer (PETT) was developed by ABB and installed on a 15 kV, 16.7 Hz railway grid-connected locomotive [21]. The system adopts an input-series–output-parallel (ISOP) modular structure with nine cascaded cells (eight active plus one redundant), each integrating a high-voltage AFE stage and an LLC resonant DC–DC converter operating at 1.75 kHz. The transformer uses nanocrystalline-core MFTs with oil cooling, while 6.5 kV and 3.3 kV IGBT modules are cooled via deionized water. The PETT achieves an overall efficiency of around 96 %, a total mass of approximately 4.5 t, and has completed over 13 000 km of service since 2012 without major failures. It is now displayed at the Swiss Museum of Transport. The PETT offers 2–4 % higher efficiency and improved power density (0.5–0.75 kVA/kg) compared to traditional traction chains (0.2–0.35 kVA/kg), making it particularly attractive for distributed propulsion platforms.

In summary, solid-state transformers offer several improvements over conventional systems for 16.7 Hz traction applications. They enable higher efficiency and significant weight reduction due to the use of medium-frequency operation and reduced raw material requirements. However, volume reduction remains challenging due to insulation constraints. Despite prototypes from major companies like ABB and Alstom, SSTs have not yet been commercially adopted, largely due to the conservative nature of the traction market, limited business incentives, and concerns around cost, reliability, and marginal performance gains in 50 Hz grids [42].

In the past decade, the focus of SST development has gradually shifted from railway applications toward grid-related applications, particularly as interfaces for distribution networks, DC grids, and hybrid AC/DC systems.

In 2011, a 1 MVA single-phase solid-state power substation (SSPS) was developed by GE to convert 13.8 kV to 465 V/ $\sqrt{3}$ using a four-stage AC–AC converter operating at 20 kHz [19]. The system adopts a fully modular phase structure with four modules connected in series on the input side and in parallel on the output side, utilizing 10 kV, 120 A SiC half-bridge MOSFET modules. A compact nanocrystalline-core transformer is employed, and the SiC modules operate only a few degrees above the 25 $^{\circ}C$ coolant temperature under 855 kVA load. Compared to conventional 60 Hz transformers used in North American distribution systems, the SSPS achieves a 75 % weight reduction and a 50 % volume reduction, with an operating efficiency of 97 %.

A 7 MW three-phase dual active bridge (DAB) converter was developed at RWTH Aachen University for high-power medium-voltage DC applications. The system transfers power between two 5 kV DC ports with ±10 % voltage tolerance and includes three medium-frequency transformers operating at 1 kHz. Each phase-leg employs series-connected 4.5 kV IGCTs. The system achieves 99.2 % peak efficiency during operation. The overall footprint is approximately 4 m × 1 m × 2 m, corresponding to a volumetric power density of 0.9 kW/dm^3.

1

This design demonstrates the feasibility of high-efficiency, compact MVDC converters based on soft-switching DAB topology and modular MFT integration.

A 500 kVA three-phase electronic power transformer (EPT) prototype was developed by HUST for a 10 kV/50 Hz distribution system, providing a 400 V/50 Hz output via an AC–DC–DC–AC topology [25]. Each phase consists of six cascaded modules in a series-input parallel-output configuration. Medium-frequency transformers with iron-based amorphous alloy cores operate at 1 kHz, contributing to a compact modular structure. The system demonstrated a peak efficiency of 93.72 % at 105 kW and integrates advanced control features such as inrush current limitation, harmonic blocking, and voltage balancing. Although the EPT currently incurs a cost approximately ten times that of a conventional transformer, its enhanced controllability and modular power interface suggest potential value for future smart grid applications.

A Megawatt-Level, four-port power electronic transformer (PET) prototype was developed by Tsinghua University based on a centralized high-frequency (HF) bus architecture [29]. It supports simultaneous interfacing with 10 kV MVAC, 10 kV MVDC, ±375 V LVDC, and 380 V LVAC ports, with 1 MVA rated capacity for AC ports and 1 MW for DC ports. The system integrates multiple power cell strings operating in ISOP, IPOS, and IPOP configurations, combining LFAC–DC–HFAC and HFAC–DC conversion stages with high-frequency transformers. At rated load, the PET achieved a peak efficiency of 96.3 % and demonstrates full port-to-port power transfer flexibility. Compared to conventional solutions, this architecture enables functional integration across AC and DC levels, supporting multi-port hybrid grids with enhanced modularity and compactness.

Beyond railway and grid applications, SST demonstrators have also been developed for fast charging systems. A 400 kW solid-state transformer (SST)-based extreme fast charger (XFC) system was developed by Delta Electronics [22, 23], featuring a 13.2 kV MVAC input and a DC output ranging from 200 V to 1000 V. The system adopts a cascaded input-series, output-parallel (ISOP) structure for medium-voltage interfacing. The SST enables a compact architecture with a total footprint of approximately 3.25 m^2 (35 ft^2), significantly smaller than the approximately 6.50 m^2 (70 ft^2) required by a conventional line-frequency transformer and charger combination. In full-power laboratory testing, the SST achieved a peak efficiency of 97.5 %, approximately 3 % higher than that of a conventional LFT-based charging system comprising a line-frequency transformer and low-frequency rectification.

In summary, across a wide range of demonstrators developed for different application scenarios, solid-state transformers have consistently demonstrated substantial reductions in size and weight. Reported weight reductions range from 50 % to 75 %, while volume reductions are typically around 50 %. Efficiency improvements of approximately 2 % to 4 % over conventional systems incorporating line-frequency transformers have also been observed. However, these benefits often come at the expense of significantly higher costs, with reported increases ranging from 50 % to up to ten times compared to traditional solutions.

Though these demonstrators have successfully proven the feasibility of solid-state transformers across various application scenarios, several key challenges remain—particularly in the context of electrolyzer application systems, where the deployment of SSTs is still relatively limited:

1. During the early stages of demonstrator development, the selection of topology and

operating frequency is often based on prior experience or heuristic choices, rather than a systematic methodology that compares different configurations in terms of performance, complexity, and suitability for the target application.

2. Once a specific topology and operating frequency are selected, developing an appropriate control strategy becomes essential to fully exploit the potential of the chosen architecture. In many cases, improved control methods are required to achieve improved system efficiency and reduced implementation complexity.

3. Accurate power loss estimation for magnetic components is critical for system-level design, particularly in thermal management and cooling system sizing. However, existing modeling approaches—such as those based on empirical Steinmetz equations—often fail to capture the nonlinear and temperature-dependent behavior of magnetic materials with sufficient accuracy. As a result, there is a growing need for more reliable and efficient loss modeling methods to support the design and optimization of high-performance SST systems.

1.4 Thesis Objective and Research Questions

As indicated previously, the research objective of this thesis is as follows.

"Optimal topology selection, performance-driven control design, and data-driven loss modeling to support the design of solid-state transformers for hydrogen electrolyzer applications."

To reach the objective, this thesis addresses the following research questions:

Q1 *What are the most suitable topology and operating frequency considering the size, weight, and loss performance for the solid-state transformer in MW-scale hydrogen electrolyzer applications?*

- Conduct a comprehensive literature review of existing SST topologies and their application contexts.
- Identify several candidate topologies suitable for hydrogen electrolyzer applications.
- Estimate converter and transformer volume using 3D design tools, weight using analytical methods, and loss using thermal modeling in Simulink.
- Perform frequency sweeps for each topology to determine their optimal operating frequencies.
- Compare all topologies at their respective optimal frequencies and select the most promising candidate for further development.

Q2 *How to develop a concise control strategy for the modular multilevel resonant-based solid-state transformer to improve performance while reducing control complexity?*

- Review existing control strategies for modular multilevel resonant converters and analyze their limitations.
- Identify key challenges related to implementation complexity and dynamic performance.

1

- Propose a new control method tailored to the chosen topology with reduced complexity.
- Validate the proposed method through simulation and theoretical comparison with existing approaches.
- Conduct real-time simulations using OPAL-RT and experimental verification on a prototype platform.

Q3 *How to push forward loss estimation accuracy of magnetic components with data-driven approaches?*

- Review existing loss modeling methods, including both equation-based and data-driven approaches.
- Develop a data-driven method capable of handling time-domain input with low computational complexity.
- Apply multi-objective optimization and transfer learning to improve prediction accuracy and generalization.
- Benchmark the proposed model against existing methods to assess its effectiveness.

1.5 Major Contributions

Targeting to give answers to the aforementioned research questions, the thesis has the contributions as follows.

- A comparative design study of the Modular Multilevel Converter-based (MMC-based), Modular Multilevel Resonant-based (MMR-based), and Input-Series–Output-Parallel (ISOP) solid-state transformer (SST) topologies is conducted for hydrogen electrolyzer applications, with a focus on efficiency, size, and weight. Practical factors such as insulation clearance are considered in volume estimations. (Chapter 2; Related publications: J1, C1 in the List of Publications at the end of the thesis)
- A concise control strategy for modular multilevel resonant SSTs is proposed, featuring continuous modulation index control with double-step staircase modulation to reduce control complexity. (Chapter 3; Related publications: J3, C2 in the List of Publications at the end of the thesis)
- A neural network-based power loss modeling method for magnetic materials is developed using limited data. The method incorporates multi-objective optimization and transfer learning to improve accuracy and generalization. (Chapter 4; Related publication: J2 in the List of Publications at the end of the thesis)

1.6 Outline of the Thesis

The thesis outline is presented in Fig.1.5. Chapter 1 provides the background for this research, beginning with an overview of the green hydrogen concept and the FlexH2

project. It then introduces the definition of solid-state transformers, along with a review of existing SST demonstrators. The chapter concludes by outlining the research objectives, key contributions, and the overall structure of the thesis.

Chapter 2 presents a comparative design study of three solid-state transformer topologies: MMC-based, MMR-based, and ISOP. For each topology, the key components are introduced and parameterized. The converter and transformer loss, size, and weight are estimated across different operating frequencies considering practical design considerations such as insulation clearance. Frequency sweep analyses are conducted to determine the optimal operating frequency for each topology, based on which a final comparison is performed under their respective best-performing frequency designs.

Chapter 3 focuses on control strategy development for the MMR-based SST. It begins with a review of the converter's operating principles and conventional control schemes, followed by the introduction of a continuous modulation index control method with a double-step staircase waveform. The proposed strategy is evaluated through simulation and experimental validation, demonstrating improved efficiency, reduced harmonic distortion, and simplified control loop design compared to existing methods.

Chapter 4 introduces a neural network-based modeling approach for power loss prediction in magnetic materials under limited data conditions. The chapter describes the feedforward neural network (FNN) architecture, input format selection, and harmonic representation. It compares the proposed method with other AI-based approaches and explores two training strategies—standard training and transfer learning—both enhanced with multi-objective optimization (MOO). The modeling results highlight the trade-off between model complexity and accuracy, with transfer learning offering improved generalization across materials.

Chapter 5 concludes the thesis by summarizing the key findings and contributions and answering the research questions.

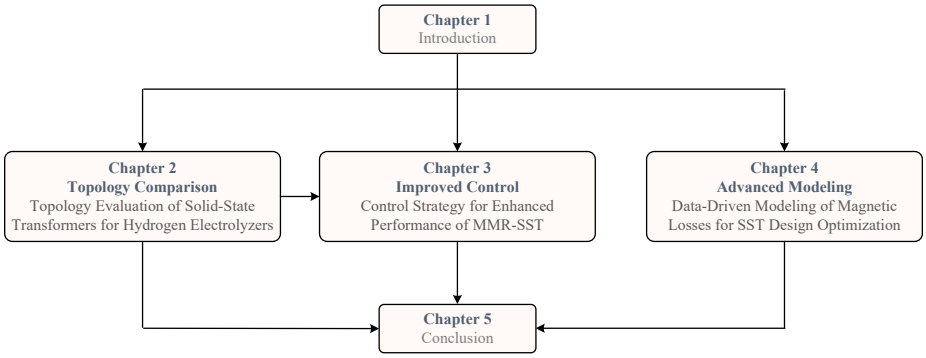


Figure 1.5: Outline of the thesis.

2

Topology Evaluation of Solid-State Transformers for Hydrogen Electrolyzers

In the production of green hydrogen, electrolyzers draw power from renewable energy sources. In this chapter, the design of SST (Solid State Transformer) for large-scale H2 electrolyzers is benchmarked. The three most promising topologies are chosen for design and comparison, including Modular Multi-level Converter (MMC) based SST, Modular Multilevel Resonant (MMR) converter based SST, and Input-Series-Output-Parallel (ISOP) based SST. The distance between converter towers for insulation and maintenance, the insulation system of the transformer, and the cooling system are designed with practical considerations in order to have an accurate estimation of the volume and weight of the SST. Losses in the switches are calculated based on equations, and losses in passive components are calculated based on FEM simulation. The operating frequency for each topology is optimized to minimize loss, weight, and volume. The best of each topology is then compared with each other to identify the most suitable one for large-scale H2 electrolyzers.

This chapter is based on:

-**Z. Li** et al., "Medium-Voltage Solid-State Transformer Design for Large-Scale H2 Electrolyzers," in IEEE Open Journal of Power Electronics, vol. 5, pp. 936-955, 2024

2.1 Introduction

Green hydrogen is recognized as a key enabling solution for facilitating large-scale renewable energy integration and alleviating grid congestion [43, 44]. For Green hydrogen, electrolyzers draw power from renewable sources. Green hydrogen can be further utilized in diverse applications, including the petroleum industry, transportation, and power generation via fuel cells or internal combustion engines. Moreover, hydrogen is seen as an eco-friendly energy storage solution due to its minimal environmental impact. Excess renewable energy can be efficiently converted and stored as hydrogen for later usage.

Typically, electrolyzers operate at tens of megawatts per unit, yet their input voltage is merely a few hundred volts DC. A transformer is essential to step down the voltage from a medium voltage bus, followed by the application of a rectifier to convert it to DC. The conventional solution often employs line frequency transformers plus diode rectifiers or thyristor rectifiers [45]. While these topologies have relatively low component costs, they tend to result in bulky overall systems. This is primarily attributed to the inclusion of line frequency transformers. In specific application scenarios where system size is of paramount importance, these conventional topologies are unacceptably large.

SST (Solid-State Transformer), on the other hand, is a promising solution to size and weight-restricted scenarios, e.g., tractions [46], nacelles of wind turbines [47, 48], future navy warships [49], underground distribution networks [50], etc. The concept of SST involves initially transforming line frequency power into medium- or high-frequency by using power converters. Subsequently, this allows for voltage conversion and galvanic isolation using a medium frequency transformer, which is notably more compact and lighter than conventional line frequency transformers. While this idea is not novel, it has recently gained increased interest and is emerging as a promising technology, particularly for medium-voltage applications, because significant advancements in semiconductor power switch manufacturing have enhanced power density, switching frequencies, and energy efficiency.

Different topologies are feasible for SST, and one frequently mentioned topology in the literature is the cascaded structure [51, 52]. The primary advantage of a cascaded structure lies in its modularity, which renders it versatile for various application scenarios with diverse voltage and current requirements.

In applications involving large-scale electrolyzers, the power conversion process commonly involves converting medium voltage input to low voltage output. For such scenarios, as depicted in Fig.2.1, adopting an ISOP (Input-Series Output-Parallel) configuration is deemed more advantageous. For power module selection, the Dual Active Bridge (DAB) converter and resonant converters are commonly employed. However, for unidirectional power flow applications in electrolyzers, the DAB's bidirectional capability is excessive, and its higher number of active switches leads to increased costs. Therefore, LLC resonant converters, being more cost-effective and efficient for such applications, are considered a better fit. Additionally, a twelve-pulse Diode Rectifier Unit (DRU) is employed for cost-effective medium voltage AC to DC conversion. A more detailed analysis and discussion will be provided in Section 2.5.

The primary limitation of the ISOP configuration lies in its requirement for numerous low-power transformers. These transformers must be insulated to withstand the entire high-level DC voltage, leading to significant increases in both volume and cost due to the

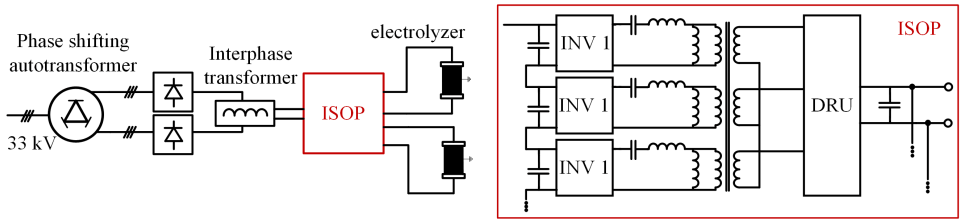


Figure 2.1: Cascaded structure SST for electrolyzer application. Instead of isolated transformer, autotransformer is used to generate the 30° phase shift angle for two DRUs, to save space and weight. The DC-DC cascaded structure uses three phase LLC modules with Input Series Output Parallel connection.

extensive need for insulation in their design. On the contrary, another suitable topology, Modular Multi-level Converter (MMC) based SST [53–55], as shown in Fig.2.2, tries to use central medium frequency transformers to solve the problems above for a more compact solution. A comparison between five different MMC-based SST topologies for AC-DC electrolyzer applications is conducted in [56]. DRU – three phase MMC-based SST is considered the best topology from the semiconductor rating and capacitor rating requirement point of view. Thus, this topology is analyzed in detail in Section 2.2.

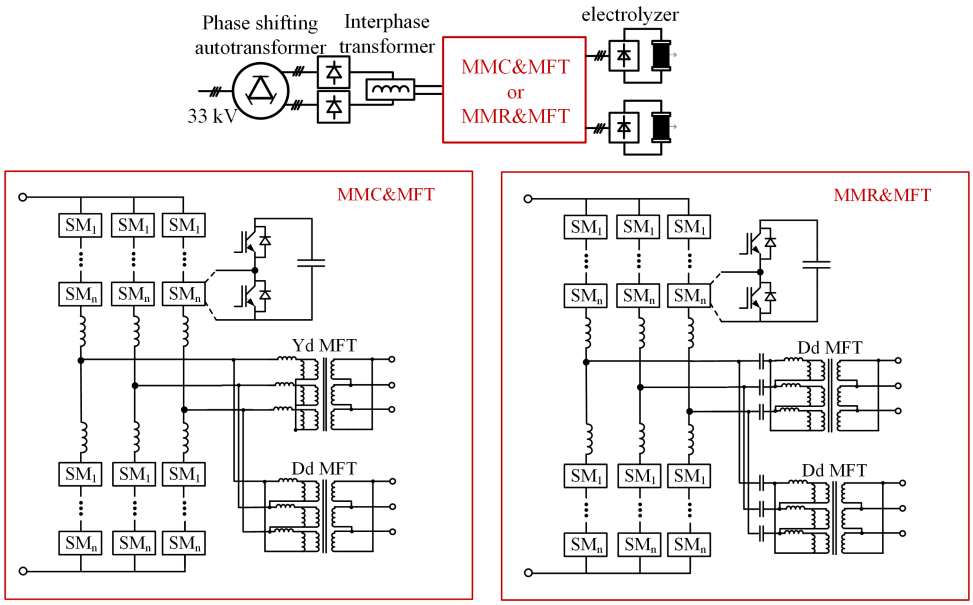


Figure 2.2: MMC-based and MMR-based SST configurations. Both systems utilize a DRU setup similar to the cascaded-structure SST. The MMC-SST employs Yd and Dd MFT configurations, creating a twelve-pulse structure that reduces conduction losses in the MMC. The MMR operates similarly to a two-level, three-phase LLC converter, utilizing two Dd MFTs. Due to the sinusoidal resonant currents of the MMR, which inherently have low total harmonic distortion (THD), the necessity for a twelve-pulse configuration is eliminated.

To reduce the switching losses of MMC-SST in medium and high-frequency applications, Modular Multi-level Resonant (MMR) converter is an effective solution [57, 58]. The MMR

resembles two-level resonant converters, e.g., LLC, where a string of modules replaces the single active switch in each bridge in the primary side, as shown in Fig.2.2. The overall structure is similar to MMC. However, additional resonant capacitors are inserted, and the modulation method is different.

Several studies have conducted comparative analysis on the topologies mentioned above [59, 60]. References [61, 62] theoretically analyze the high insulation requirement drawback of the cascaded structure. However, no detailed calculations are presented. An assessment of charging station converter structures is carried out in [63] by using MMC as an active front-end rectifier in three different topologies. However, the transformer size and insulation distance are not considered. References [64, 65] compared cascaded SST and MMC-SST, focusing only on the power converter parts analysis. Despite extensive studies in the field, there remains a noticeable lack of quantitative analysis comparing different SST topologies, especially regarding their insulation requirements. The contributions of this Chapter are:

1. This Chapter conducts a comprehensive quantitative comparison of MMC-based, MMR-based, and ISOP SSTs for electrolyzer applications, evaluating them from the perspectives of efficiency, size, and weight. This comparison provides valuable insights into the optimal choice of SST topology based on specific application requirements.

2. Detailed calculations of the size and weight of converter towers and transformers are performed, incorporating practical considerations such as insulation distance requirements. This approach ensures a realistic assessment of the spatial and structural implications of each SST topology.

3. The analysis identifies the significant impact of chiller size and weight in the overall size and weight comparison, highlighting the importance of cooling systems in the efficiency and feasibility of converter and medium frequency transformer designs.

To begin with, Section 2.2 first introduces the components of the MMC-SST and the parameter design methods. Power converter and transformer loss, size, and weight estimations are carried out consecutively. A comparison of the performance metrics at different frequencies is shown to decide the optimal operating frequency of the MMC-SST. Following a similar procedure, Section 2.3 and Section 2.4 indicate the MMR and ISOP SST loss, size, and weight estimations and these values at different frequencies, respectively. Additionally, Section 2.5 presents an analysis of the frequency sweep results and a comparison of the three topologies at their optimal operating frequencies. The Chapter concludes with Section 2.6.

2.2 Performance Metrics for Modular Multi-Level Converter-Based Solid-State Transformer

This Section presents a detailed evaluation of the MMC-based SST, including system parameter design as well as loss, size, and weight estimation. The modelling and calculation procedures established here form the basis for the MMR-based and ISOP-based SSTs presented in the subsequent Sections.

2.2.1 Parameter Design of the Complete System

The complete system, which includes two electrolyzers, has a total power rating of 45.4 MW. For this application, the input current ripple to the electrolyzer must be confined to within 3%, as specified by the industrial partner. Exceeding this threshold can reduce the lifespan of the electrolyzer and adversely affect the rate of hydrogen production. This requirement will be addressed in the subsequent design phase.

12-Pulse Rectifier System

To satisfy the IEC61000-3-6 current harmonics requirements of the 33 kV grid, a 12-pulse rectifier circuit should be used. To generate the $\pm 15^\circ$ voltage phase shift, usually a 3-winding isolated transformer is used. However, because of the isolation functionality and the fact that 50 Hz is implemented as the operating frequency, this isolated transformer will be bulky and heavy. To fulfill the purpose of size and weight reduction of solid-state transformers, an autotransformer can be used, as there is no galvanic isolation between the input and output ports. The vector diagram and the configuration are shown in Fig.2.3.

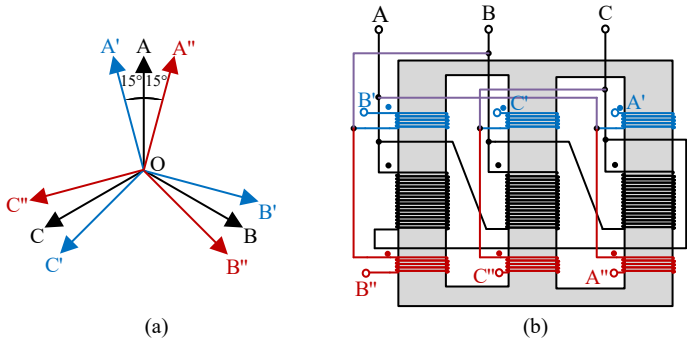


Figure 2.3: (a) Autotransformer vector graph. A' and A" represent the generated phase A voltages with a 30° phase shift. (b) Windings of an autotransformer on a three-limb core.

Based on the autotransformer vector diagram, the voltage transfer ratio of the 12-pulse autotransformer can be derived as $1/\cos(15^\circ) = 1.0353$.

Following the autotransformer, two 6-pulse diode rectifiers are connected to the output of the autotransformer. The voltage transfer ratio of the 6-pulse diode rectifier from the input three phase AC line to line peak voltage to output DC voltage is $3/\pi$. Diodes selection method is as follows: first, the diode peak reverse voltage and average current are measured in the simulation, which are 48.3 kV and 300 A, respectively. Then, a voltage safety factor of 2.25 and a current safety factor of 2 are applied, according to [66]. If the Infineon D471N diode with a voltage rating of 9000 V and current rating of 600 A is selected, then for each bridge $\left\lceil \frac{48.3\,\text{kV} \times 2.25}{9\,\text{kV}} \right\rceil = 13$ diodes should be connected in series. This calculation is intended for preliminary device sizing and loss estimation. Practical implementation aspects, such as voltage sharing among series-connected diodes, are not considered in this study.

The interphase transformer facilitates the parallel connection of two diode bridges, each fed by voltage sources with a phase difference [67]. Specifically, two interphase transformers

are needed in our applications: one for each voltage polarity. The configuration of an interphase transformer and its associated connections are depicted in Fig.2.4.

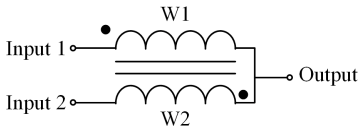


Figure 2.4: Interphase transformer diagram. W1 and W2 represents the two windings of the interphase transformer.

As a result, the output DC voltage of the interphase transformer is $U_{dc} = 33 \times \sqrt{2} \times 3/\pi \times 1.0353 = 46.2$ kV.

MMC System

The MMC design follows the design guidelines in [68, 69]. MMC's initially selected fundamental frequency is 400 Hz, but the design process could also be applied to other frequencies.

The maximum modulation index corresponding to the maximum operating point of the electrolyzer is set to 0.9 to leave a certain safety margin, accounting for possible variations in the grid input voltage. The maximum arm current value according to the simulation is 1050 A. With a current safety factor of 2, the 3.3 kV 1.2 kA ABB 5SNA 1200E330100 IGBT with a peak collector current of 2400 A is chosen, and the voltage rating is derated to 2 kV to have a safe margin for potential transient voltages. The number of submodules is calculated as 24. Half-bridge submodules are adopted in this SST application. When a DC-side short-circuit fault occurs, the DC-link voltage drops, and the downstream converter stages, including the MMC, MFT, and MFDRU, lose their energy source. Fault current limitation and isolation are therefore handled by upstream protection devices, such as circuit breakers, rather than by requiring the MMC to provide inherent fault blocking capability. The submodule capacitance is chosen as 1.45 mF to ensure that the submodule voltage variation is within the limit and the IGBT's power loss is minimal.

The arm inductance is calculated based on [27] as 0.9 mH. In this study, the losses attributed to arm inductance are neglected, as they contribute to only approximately 0.02% of the Modular Multi-level Converter's (MMC) rated power, according to [69].

Different modulation methods for MMC exist, including carrier-based PWM and Nearest Level Control (NLC) method. To reduce the unnecessary switching behavior and increase the efficiency, NLC plus advanced sorting algorithms have been applied to the MMC, i.e., the cell tolerance band (CTB) method [69]. Fig. 2.5(a) displays the submodule voltage waveforms, demonstrating the effectiveness of the CTB method. Additionally, Fig. 2.5(b) illustrates the MMC output currents with low harmonic content.

Medium Frequency Transformer

The medium-frequency transformer (MFT) is designed based on IEC 60076 [70]. The 12-pulse behavior seen by the MMC output is realized by phase shifting the transformer's primary windings. And there are two MFTs, one with Yd connection and another with Dd connection. According to the power limit per transformer in IEC 60076, and the demand of the two electrolyzers, the oil-immersed transformers with two active parts in one tank is chosen. Subsection 2.2.4 will elaborate on the transformer design.

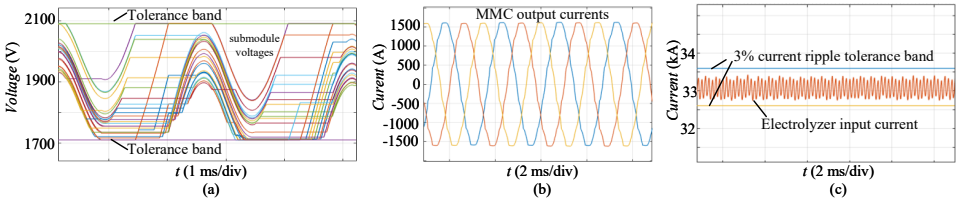


Figure 2.5: Key waveforms of the MMC-SST: (a) submodule voltages of phase A upper arm, balanced by the cell tolerance band (CTB) method, (b) MMC output currents, and (c) electrolyzer input currents maintained within a 3% current ripple band.

Medium Frequency DRU Rectifier

Two 6-pulse medium frequency DRUs are connected to the output of the MFT. The measured peak reverse voltage is 800 V, and the average current is 12 kA. With the same 2.25 voltage safety factor and 2 current safety factors, the 5SDF28L4521 medium frequency diode with a voltage rating of 4500 V and current rating of 2620 A is chosen, and for each bridge, a total of 10 diodes should be parallel connected. This assumption is adopted for the purpose of loss estimation, and practical current-sharing aspects are not considered. To ensure the electrolyzer input current ripple remains within the required 3%, a 50 μH inductor has been integrated prior to the connection with the electrolyzer. The resulting input current waveform is depicted in Fig. 2.5(c), demonstrating compliance with the ripple specifications.

2.2.2 Thermal Modelling and Loss Estimation of Power Converters

The loss estimations for power converters in MMC-SST include 50 Hz DRU losses, MMC losses, and medium frequency DRU losses. Thermal models are built in Simulink to calculate these losses.

For the 12-pulse DRU, only conduction losses need to be considered because of the fundamental frequency operation, based on [66]. The equation to calculate the conduction losses is [66]:

$$P_{\text{loss}} = U_{T0} \times I_{\text{FAV}} + r_T \times I_{\text{Frms}}^2 \tag{2.1}$$

where I_{FAV} is the average current through the diode, and I_{Frms} is the root mean square value of the current. The threshold voltage U_{T0} and the slope resistance r_T are given in the datasheet. For the cooling design, one needs to ensure that the junction temperature of the devices remains within 125 °C, as obtained from thermal modelling. Thus, the switches will not be damaged during operation. Due to the low losses in the DRU, forced air cooling is sufficient, and the heatsink of ASENERGI O343 with a thermal resistance of 0.1 K/W is chosen.

For MMC losses calculation, the IGBT/diode thermal resistance, thermal capacitance, turn-on, turn-off, and on-state characteristics are imported from the ABB 5SNA 1200E330100 switch datasheet. And the junction temperature is calculated based on the equivalent circuit shown in Fig.2.6. Liquid cooling is applied to MMC submodule, and the BK CP1426 heatsink from Baknor with a thermal resistance of 0.006 K/W at 7.5 L/min flow rate is chosen, and the inlet water temperature is assumed as 20 °C.

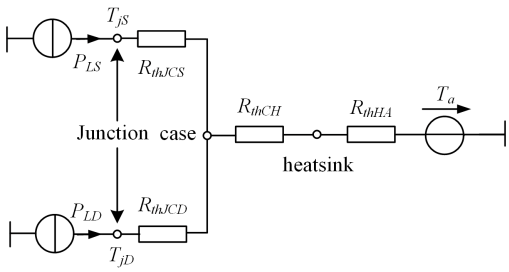


Figure 2.6: Equivalent thermal model of MMC switches. P_{LS}, P_{LD}, $R_{\mathrm{th}JCS}$, $R_{\mathrm{th}JCD}$, $R_{\mathrm{th}CH}$, $R_{\mathrm{th}HA}$, and T_a represent IGBT losses, diode losses, IGBT junction-to-case thermal resistance, diode junction-to-case thermal resistance, case-to-heatsink thermal resistance, heatsink-to-ambient thermal resistance, and ambient temperature, respectively.

For the medium-frequency diode rectifier, both conduction and turn-off losses need to be considered because of the medium-frequency operating conditions (in our case, it is 400 Hz). The conduction losses calculation method is the same as for the DRU, and the turn-off losses of the diodes are calculated as [66]:

$$P_{RQ} = Q_r \times u_R \times 0.5 \times f \tag{2.2}$$

where Q_r is the maximum recovery charge given in the datasheet, u_R is the driving voltage after commutation, and f is the operating frequency. Liquid cooling is needed for the medium-frequency DRU, and the heatsink of ASENERGI SS15 with a thermal resistance of 0.011 K/W has been chosen.

With the chosen cooling methods, the junction temperatures of the switches of input DRU, MMC, and medium frequency DRU are maintained well within 125℃. The losses are summarized in Table 2.1.

Table 2.1: MMC-SST loss breakdown at the rated power of 45.4 MW, including MMC, DRU at 50 Hz, and medium-frequency DRU

MMC losses (kW)			**50 Hz DRU losses (kW)**
switching loss	conduction loss	total loss	
214	235	449	49.5
Medium-frequency DRU losses (kW)			**SST total losses (kW)**
switching loss	conduction loss	total loss	
50	340	390	888.5

2.2.3 Size and Weight Estimation of MMC Converter

Since all three topologies have front-side diode rectifiers, their size and weight are not considered in the comparison. As for the secondary side DRU in each topology, these

passive switch sizes and weights are not comparable with front side modules. Thus, only the front-side modules size and weight of the three topologies are estimated and calculated.

In Subsection 2.2.5, the best operating frequency for MMC-SST is observed to be around 400 Hz, and the following analysis is for the 400 Hz scenario.

For MMC converter module, the size and weight of the 2 kV DC film capacitor are estimated by curve fitting with the data from manufacturer datasheet [71, 72]:

$$size(m^3) = 9.182 \times C + 4.195 \times 10^{-4} \tag{2.3}$$

$$weight(kg) = 11740 \times C + 16.17 \tag{2.4}$$

where C represents the value of capacitance in F. As a result, the size and weight estimations of the required 1.45 mF capacitance are 0.014 m^3 and 33 kg, respectively. This formulaic approach facilitates initial comparative assessments across various topologies at a preliminary design stage. Once the optimal topology and operating frequency are established, it is recommended to perform detailed capacitor selection based on component specifications. This step is essential for obtaining precise measurements of component size and weight, which are critical for the practical implementation of the design. The total size and weight of two IGBTs in one module are 1.56×10^{-3} m^3 and 2.4 kg, respectively, calculated directly from the datasheet.

Next, a size estimation of the converter tower is carried out. According to [73], the DC capacitor occupies half the volume of the Alstom Maxsine half-bridge submodule. Based on this observation, adding the size of IGBTs and capacitors and leaving some room for other components, the submodule size is estimated to be 0.04 m^3. Similarly, the submodule weight is estimated to be 50 kg. This estimation serves as a rapid calculation method for comparative stages, while a comprehensive consideration of all component volumes and weights should be done during the final design phase.

The weight value is multiplied by 144 submodules, and the total weight of the submodules is estimated to be 7.2 tons. For MMC converter valve tower size estimation, the insulation requirements need to be considered.

The MMC converter used for MMC-SST is shown in Fig. 2.7. The arrangement refers to [73]. The insulation designs refer to IEC 60071-1. Only the major parts of the MMC are shown, excluding the conductors, busbars, etc., because this analysis aims to estimate the MMC size considering the insulation distance. The red and blue cylinders represent the + and − DC inputs, respectively. The AC outputs are shown in Fig. 2.7(c), and the connection relationship between the modules of one converter tower is illustrated in Fig. 2.7(b).

Since the submodule size is estimated as 0.04 m^3, and it should be in a cuboid shape, the MMC submodule is estimated to be 0.45 m (length) × 0.3 m (width) × 0.3 m (height).

In the 3D design, four insulation distances, d_1–d_4, have been analyzed.

- The distance between modules d_1: Following the insulation coordination principles and standard withstand voltage levels defined in IEC 60071, a lightning impulse withstand voltage of 40 kV is selected for the voltage difference between adjacent submodules, given by $U_{dc}/2/N_{sm} = 23.1\,kV/24 = 0.96\,kV$. Based on this withstand level, the minimum required clearance is 60 mm, which is defined as d_1.

- The distance between the rows of the converter towers d_2: The voltage difference between rows is $23.1\,\text{kV}/24 \times 16 = 15.4\,\text{kV}$, and the required lightning impulse withstand voltage is 95 kV. An insulator is placed between different rows, and according to the manufacturer datasheet [74], the height corresponding to 95 kV is 255 mm, which is set as d_2.
- The distance between the lower row and the ground d_3: The maximum output phase voltage is $U_{\text{dc}}/2 = 23.1\,\text{kV}$, which is the voltage difference between the lower row and the ground. The required impulse withstand voltage is also 95 kV, thus d_3 is set as 255 mm, same as d_2.
- The distance between the converter towers d_4: The voltage difference between converter towers of the same phase is 46.2 kV DC, equivalent to an AC RMS voltage of 32.7 kV. The corresponding impulse withstand voltage is 170 kV, and the required clearance is 320 mm. This is increased to 1 m for maintenance purposes.

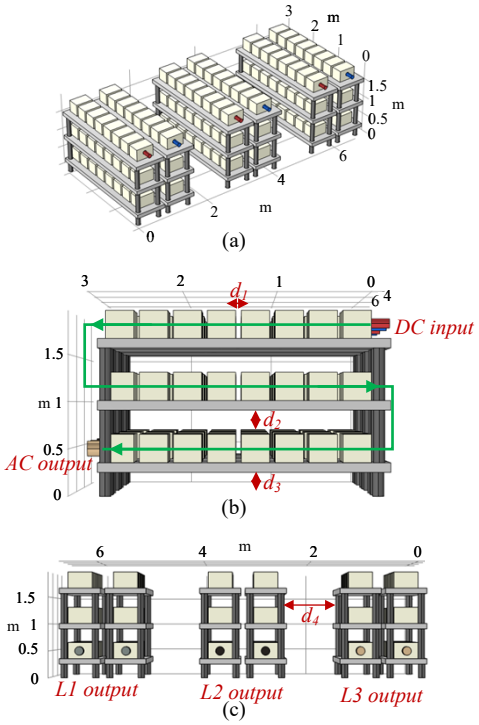


Figure 2.7: MMC converter 3D modelling (a) overall structure, (b) side view 1, (c) side view 2. In total there are six converter towers, corresponding to 6 arms. Each converter tower has three rows, and each row has eight modules. L1, L2, and L3 represents MMC three phase AC outputs.

As a result, the total size shown in Fig. 2.7 is $6.86\,\text{m} \times 3.22\,\text{m} \times 1.95\,\text{m} = 43\,\text{m}^3$.

A summary of MMC-SST converter size and component weights is shown in Table 2.2, where "other module weight" represents an estimation of other components, e.g., gate

drivers and protection systems. The weight of the mechanical construction and enclosure is not included, as the focus is on the major power-electronic components.

Table 2.2: MMC-SST converter detailed size and weight. The MMC size represents the total size of the converter tower in Fig. 2.7. The weight estimation focuses on the capacitor and switches weight.

MMC size (m^3)	Capacitor weight (ton)	Switches weight (ton)	Other module weight (ton)
43	4.752	0.3456	2.1

2.2.4 Design of the Medium-Frequency Transformer for MMC-SST

In order to reduce the MMC harmonics according to IEEE 519, one transformer is configured as Yd, and the other is configured as Dd. The values of the voltages (primary and secondary) and currents are first calculated manually and then verified according to Simulink model. The corresponding primary currents are 580 A for the Yd type and 338 A for the Dd type.

Yd Transformer Design

First, the voltage transfer ratio of the transformers is calculated. The MFT primary side line-to-line RMS voltage and the secondary side line-to-line RMS voltage are calculated according to:

$$U_{pri-LL-RMS} = \frac{U_{dc}}{2} \times m \times \sqrt{\frac{3}{2}} \tag{2.5}$$

$$U_{\text{sec-LL-RMS}} = U_{\text{electrolyzer}} \times \frac{\pi}{3} \times \frac{1}{\sqrt{2}} \tag{2.6}$$

where m is the MMC modulation index and $U_{\text{electrolyzer}}$ is the electrolyzer input voltage. The theoretical voltage transfer ratio of the MFT is calculated as 50. However, due to the commutation phenomenon, the selected voltage transfer ratio of the MFT is decreased to 44.5 to meet the required electrolyzer voltage. The number of turns on the secondary side must be selected as low as possible. This is due to efficiency considerations, taking into account the high current on the secondary side. Practically, it is not feasible to select $N_s = 1$, as continuously transposed conductors (CTCs) require a minimum length to ensure all strands are appropriately positioned. Therefore,

$$N_s = 2 \rightarrow N_p = 52 \tag{2.7}$$

where N_s is the number of secondary turns, and N_p is the number of primary turns. The primary line-to-line voltage is $U_{\text{pri–LL–RMS}} = 25429\,\text{V}$, and the RMS value of the primary phase voltage is $U_{\text{pri–ph–RMS}} = 14615\,\text{V}$.

The following is a brief explanation of core material selection and design. The cross-section of the core can be calculated as follows:

$$A_c = \frac{U_{\text{pri-ph-RMS}}}{k_c \times k_w \times B_m \times f \times N_p} \tag{2.8}$$

where k_c is the core stacking factor, k_w is the form factor, B_m is the maximum flux density in the core, and f is the frequency.

Different core materials are feasible. For high-power applications, grain-oriented electrical steel and amorphous are more common choices [44]. The characteristics of electrical steel and amorphous are compared in Table 2.3.

Table 2.3: Comparison of the characteristics of electrical steel and amorphous alloys

Material	Layer thickness (μm)	Loss @400 Hz (W/kg)	B_{sat} (T)	Permeability	Density (kg/m^3)
Grain-oriented electrical steel	100	16	2	2000	7800
Amorphous	25	1.3	1.63	6500	7300

According to Table 2.3, electrical steel is a good choice for 50/60 Hz applications. However, the higher the frequency, the higher the core loss. Therefore, alternative materials such as amorphous are more beneficial. Another difference between a transformer made of electrical steel and the one made of amorphous is that electrical steel transformers are made of several plates for the limbs and yokes. However, amorphous transformers are made by a number of thin strips which are placed next to each other to form the entire core. From a manufacturing point of view, to insert the coils into an electrical steel core, the manufacturer removes the upper yoke, inserts the coils, and puts the upper yoke again [75, 76]. For an amorphous core, the manufacturer unlaces the strips, inserts the coils, and re-laces the strips again [54]. Although the manufacturing procedure is more complex for the amorphous-based transformers, amorphous is selected as the magnetic material of the core since the frequency in the present application is relatively high. The selected alloy is Metglas 2605HB1M, which is available in strips with various widths, such as 142.2 mm, 170.2 mm, and 213.4 mm [77]. The nominal thickness of the strips is 25 μm, which results in a good lamination.

Assuming $B_{\mathrm{m}} = 1.2\,\mathrm{T}$, $k_{\mathrm{c}} = 0.79$, $k_{\mathrm{w}} = 4.44$, and $f = 400\,\mathrm{Hz}$ in (2.8) results in $A_{\mathrm{c}} = 0.167\,\mathrm{m}^2$. For the MMC-SST topology, amorphous strips with a width of 213.4 mm are selected. Therefore, the width of the core is calculated as 392 mm, as shown in Fig. 2.8(a). The core is made of two cores stacked on top of each other. The core dimensions are shown in Fig. 2.8(b).

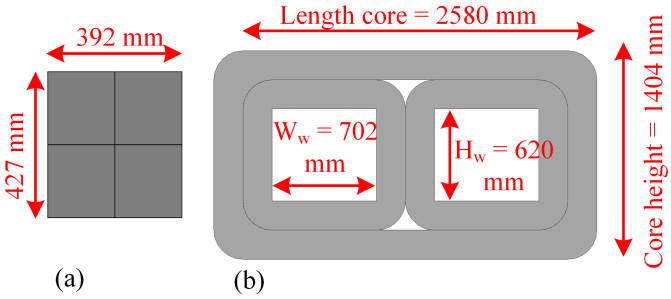


Figure 2.8: Details of the core design for the MMC-SST transformer: a) the cross-section of the core, b) the 3D view of the magnetic core

The core loss of the transformer is calculated as follows [78]:

$$P_c = \text{Volume}_c \times \varrho_c \times P_{c0} \times \left(\frac{f}{f_0}\right)^{\alpha} \times \left(\frac{B_m}{B_{m0}}\right)^{\beta} \times \left(\frac{k_w}{k_{w0}}\right)^{2(\alpha-1)} \tag{2.9}$$

where Volume_c is the volume of the core, ϱ_c is the density of the core, P_{c0} is the core loss per kilogram as listed in Table 2.3, f_0 is the reference frequency (400 Hz), B_{m0} is the reference maximum flux density (1.0 T), k_{w0} is the reference form factor (4.44), $\alpha = 1.47$ is the frequency dependency factor, and $\beta = 1.52$ is the flux density dependency factor.

Besides core losses, transformers are affected by *stray losses*, which stem from eddy currents induced in the transformer's conductive components, such as clamps, flitch, plates, tanks, and shunts [79]. The calculation of stray losses is a complex task, requiring the utilization of Finite Element Method (FEM) simulations or experimental estimation techniques to obtain accurate measurements [80, 81]. In this Chapter, stray loss is estimated based on the method described in [82].

After the core design is accomplished, the CTCs are selected for the conductors of the transformer. CTCs have two advantages. Firstly, CTCs can mitigate the skin effect due to the presence of several strands. Secondly, with the transposition of the strands, they all have similar lengths and experience similar background magnetic fields to avoid circulating current in the windings [83]. The primary CTC size CTC_{pri} and secondary CTC size CTC_{sec} can be designed as follows:

$$A_p = \frac{I_{\text{pri-ph-RMS}}}{J_p} = \frac{580}{2.5} = 232\,\text{mm}^2 \quad \Rightarrow \quad \text{CTC}_{\text{pri}} : 15 \times 8 \times 2\,\text{mm}^2\ (n \times w \times t) \tag{2.10}$$

$$A_s = \frac{I_{\text{sec-ph-RMS}}}{J_s} = \frac{15200}{2} = 7600\,\text{mm}^2 \quad \Rightarrow \quad \text{CTC}_{\text{sec}} : 13 \times 15 \times 19 \times 2\,\text{mm}^2\ (N \times n \times w \times t) \tag{2.11}$$

where A_p and A_s are required primary and secondary conductor size, respectively, $I_{\text{pri-ph-RMS}}$ and $I_{\text{sec-ph-RMS}}$ are phase current RMS values of the primary and secondary, respectively, J_p and J_s are the current density of the primary and secondary, respectively, N is the number of parallel paths on the secondary side to handle huge amounts of current, n is the number of strands (which is an odd number), w is the width of each strand, and t is the thickness of each strand.

The primary and secondary conductors are shown in Fig. 2.9(a) and (b), respectively. The transformer window is designed as shown in Fig. 2.9(c). Note that because of high-current busbars, the secondary is built over the primary. The primary is made of 26 disks, and each has two turns. The secondary is made of 13 parallel disks to handle the high-current. While the distance between disks in the primary is for the oil ducts, the secondary has more space between disks to provide access to the busbar connection. A FEM simulation using a 3D ANSYS Maxwell model was performed to determine the leakage and magnetizing inductances, crucial for voltage impedance calculations and the resonant topology designs discussed in Section 2.3 and Section 2.4. Additionally, a 2D COMSOL model was used to compute the AC load losses, a key factor in assessing transformer efficiency and informing cooling system design. The results of the FEM simulations for MMC-SST MFT are summarized in Table 2.4. The meshing performance of the FEM

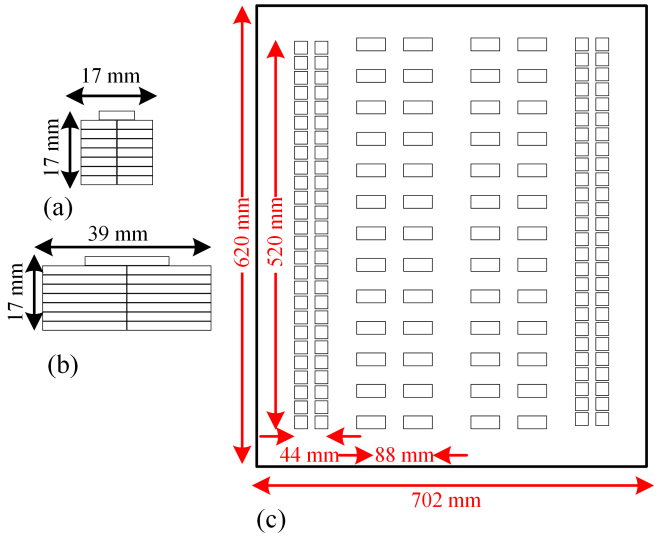


Figure 2.9: The details of the winding design of the MMC-SST transformer: a) Yd CTC of primary, b) Yd CTC of secondary, c) Yd window.

simulation is shown in Fig. 2.10. The 3D view of the MMC-SST MFT in ANSYS Maxwell is shown in Fig. 2.11.

Table 2.4: FEM results for MMC-SST

Configuration	Parameter	Value
Yd	L_{lk}	1.399 mH
	r_p	816.1 $\mu\Omega$/m
	r_s	50.4 $\mu\Omega$/m
Dd	L_{lk}	4.001 mH
	r_p	1549.8 $\mu\Omega$/m
	r_s	51.4 $\mu\Omega$/m

To estimate the copper loss of the transformer, first the Mean Length per Turn (MLT) is calculated as follows:

$$MLT_p = \pi \times (D_p + W_p) \tag{2.12}$$

where D_p is the diameter and W_p is the width of the primary winding. Then, the length of the primary can be calculated as follows:

$$l_p = MLT_p \times N_p \tag{2.13}$$

According to the FEM simulation result in Table 2.4, the average AC resistance r_p is 816.1 $\mu\Omega$/m. The load loss based on the AC resistance can be calculated as follows:

$$R_p = l_p \times r_p \tag{2.14}$$

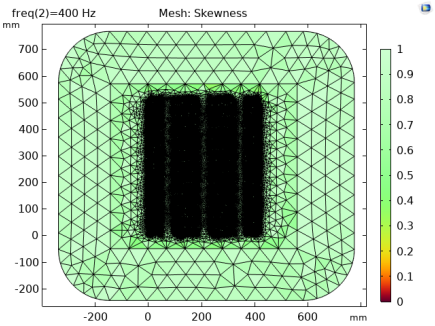


Figure 2.10: Meshing performance of the COMSOL 2D simulation for Yd MMC-SST MFT. The color map represents the element skewness, which is used as an indicator of mesh quality (values close to 1 correspond to well-shaped elements).

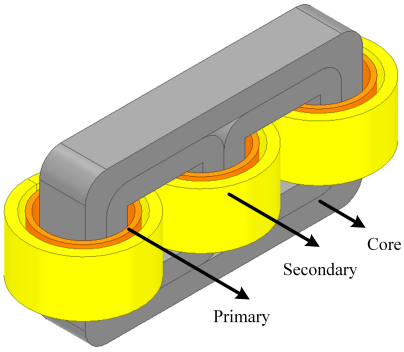


Figure 2.11: 3D view of the MMC-SST MFT

$$Loss_p = 3 \times R_p \times I^2_{\text{pri-ph-RMS}} \tag{2.15}$$

The weight of the primary winding can be calculated as follows:

$$Weight_p = 3 \times l_p \times CTC_{\text{pri}} \times \varrho_{\text{cu}} \tag{2.16}$$

where ϱ_{cu} is the density of copper. The loss and weight of the secondary winding can be calculated using a similar method. Tables 2.7 and 2.8 in Section 2.2.4 summarize the loss and weight for the MFTs.

Dd Transformer Design

The design of the transformer for the Dd configuration is similar to the design of the Yd transformer. The difference is in the primary voltage, and in this case, it is $U_{\text{pri-LL-RMS}} = U_{\text{pri-ph-RMS}} = 25429\,\text{V}$. To maintain the same voltage on the secondary side, the number of turns on the primary side is higher (90 turns compared to 52 turns). Accordingly, the primary current RMS value is 338 A. Therefore, the primary CTC can be designed as $\text{CTC}_{\text{pri}} = n \times w \times t = 13 \times 5 \times 2 = 130\,\text{mm}^2$. The primary consists of 30 disks, which have 3 turns each. The secondary structure is the same as Yd transformer. The AC resistances per

unit length for Dd transformer are $r_p = 1549.8\,\mu\Omega/\text{m}$ and $r_s = 51.5\,\mu\Omega/\text{m}$, as summarized in Table 2.4.

Insulation Considerations, Thermal Management, and Tank Design

Because of the power rating and the amount of loss of the transformers, the MFT in the present study is oil-type, which is filled with mineral oil. The temperature rise limits according to IEC 60076-2 [84] are summarized in Table 2.5. Therefore, the oil temperature for the loss calculations in the COMSOL 2D simulation is considered as $T_{\text{oil}} = 78 + T_{\text{amb}}$, where T_{amb} is the ambient temperature. The MFT for MMC-SST topology consists of two active parts, a Yd and a Dd transformers, in one tank. The cooling system is oil-forced and water-forced (OFWF), as shown in Fig. 2.12.

Table 2.5: Temperature rise limits according to IEC 60076-2 [84]

Components	Temperature rise limit (K)
Top insulation liquid	60
ON (Oil-Natural) and OF (Oil-Forced) cooling systems – average winding	65
Hot-spot winding	78

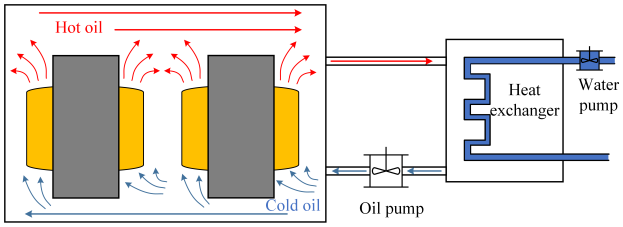


Figure 2.12: Schematic of an oil-forced, water-forced (OFWF) cooling system.

To avoid complexity, it is assumed that the oil flow inside the tank has no eddy patterns. The oil flow between disks is assumed to be laminar. The thermal design follows the methods described in [85–87]. The active parts inside the tank are shown in Fig. 2.13. As shown in Fig. 2.13, there are distances between MFTs and the side wall of the tank (d_1), two MFTs (d_2), MFTs and upper lid of the tank (d_3), and MFTs and bottom of the tank (d_4). More information about the insulation design are provided below.

To satisfy the insulation distances d_1 to d_4 in Fig. 2.13, these distances between the active parts (MFTs) and the walls of the transformer tank are determined by considering three main factors:

- Electrical Clearance: ensuring adequate clearance to prevent dielectric breakdown in the transformer oil, following the standards set by IEC 60156 [88].
- Thermal Management: Adequate spacing is critical for effective heat dissipation, which is vital given the thermal characteristics of the transformer oil compared to air.

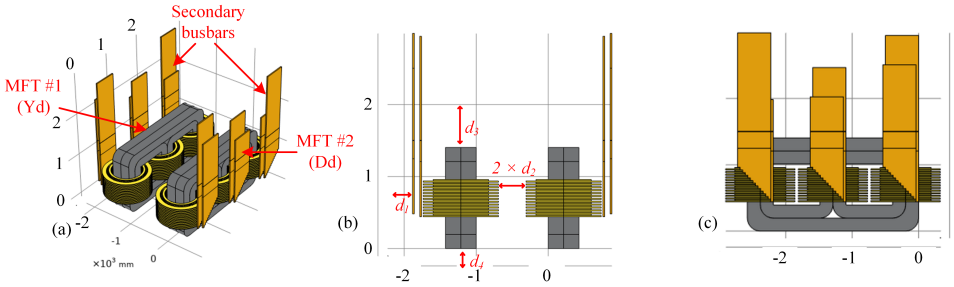


Figure 2.13: 3D view of the active parts inside the tank a) overall view, b) side view 1, and c) side view 2. The high-current busbars on the secondary side are designed to facilitate the parallel connection of the secondary disks and provide sufficient space for the horizontal busbars outside the tank.

- Mechanical Stability and Safety: accounting for sufficient space to accommodate thermal expansion of the oil and other components like the core and windings.

Among these factors, thermal management is predominant. The permissible fields within the oil-type transformer at critical locations are carefully considered to ensure a reliable operation , as summarized in Table 2.6.

Table 2.6: Permissible field strength at the critical points of an oil-type transformer [89]

No	Critical point	Electric field (kV/mm)
1	Oil, between barriers	10
2	Oil, along interfaces	< 5
3	Oil-impregnated paper, perpendicular to layers	30 – 60
4	Oil-impregnated paper, parallel to layers	6 – 10

Given the inherent uncertainties in these figures, a safety margin is crucial. Considering the maximum allowable electric field within the transformer oil to be 5 kV/mm and implementing a safety margin, the maximum electric field is 2.5 kV/mm. This conservative approach is further reinforced by the calculation for the minimum required gap between the windings and the tank, based on the peak of the maximum applied test voltage ($\sqrt{2}\times 70$ kV $\approx$ 100 kV), resulting in:

$$G_{\text{min}} = \frac{V_{\text{test_max}}}{E_{\text{oil_max}}} = \frac{100}{2.5} = 40 \text{ mm} \tag{2.17}$$

where G_{min} is the minimum required gap, $V_{\text{test_max}}$ is the peak of maximum applied test voltage, and $E_{\text{oil_max}}$ is the maximum of permissible electric field inside the oil. Then d_1 – d_4 must be greater than G_{min}.

However, to ensure sufficient spacing for the effective laminar flow of oil, which is critical for both cooling and electrical insulation purposes, in this design d_1, d_2, and d_4 are selected as 100 mm—significantly exceeding the minimum requirement. Also, d_3 is selected as 300 mm to guarantee enough spacing on top of the transformer for convection

heat dissipation. This extra spacing helps mitigate any potential risk associated with the alignment and positioning of the internal components during operation and maintenance, thereby enhancing the overall system reliability and robustness.

The FEM simulation of the electric filed is shown in Fig. 2.14., which indicates the electric filed between the primary winding and core, and between disks of the primary winding, and between turns of a disk regarding the values of Table 2.6.

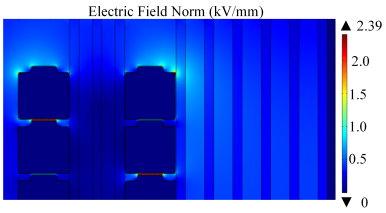


Figure 2.14: The FEM simulation of electric filed.

The CTC strands are enameled, and the CTC itself is insulated by oil-immersed paper. A pressboard makes the disk structure support the winding structure during normal operation and fault forces. The windings are made of disks, which are more compact and provide better voltage distribution, as shown in Fig. 2.15.

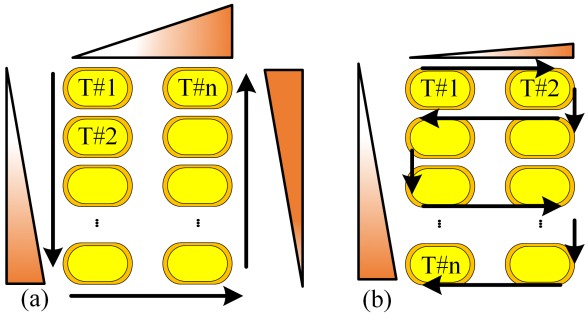


Figure 2.15: Comparison of voltage distribution of (a) a layer winding and (b) a disk winding. T#1, T#2, and T#n represent the first, second, and *n*th turn, respectively.

The rated voltage of the transformer is calculated using (2.5), which is 25.429 kV_{rms}. For insulation design, the input voltage is considered as $U_{\text{pri-LL-RMS}} = 25.5\,\text{kV}$. Based on IEC 60076-3, the test voltage levels for transformers with the highest voltage for equipment winding between 24 kV and 36 kV are as follows: Full Wave Lightning Impulse (LI) = 170 kV, Chopped Wave Lightning Impulse (LIC) = 187 kV, and Line Terminal AC Withstand (LTAC) = 70 kV [90].

However, in the present study, dedicated lightning protection coordination at the system level is outside the scope of this work. Therefore, only the Line Terminal AC Withstand (LTAC) requirement is considered for the insulation design. Accordingly, the MFT is designed to withstand an LTAC test voltage of 70 kV_{rms}.

The cores and the tank are earthed, thus they have zero potential. Due to the presence of high-current busbars of the low-voltage winding, the primary winding, which is connected

to the medium voltage side, is placed near the core, while the secondary winding is placed over the primary. This configuration results in the highest electric field occurring between the primary and the core, particularly near the edges of the core.

Overall Metrics of the MMC-SST MFT

The transformers dimensions are $3232 \times 1044 \times 1404$ mm ($x \times y \times z$). Thus, the volume of active parts is 9.48 m^3. The thickness of the tank plates is selected as $t_{tank} = 5$ mm. Thus, the tank size is calculated as:

$$X_{tank} = x_{trans} + (2 \times d_1) + (2 \times t_{tank}) \tag{2.18}$$

$$Y_{tank} = (2 \times d_1) + (2 \times d_2) + (2 \times y_{trans}) + (2 \times t_{tank}) \tag{2.19}$$

$$Z_{tank} = d_3 + d_4 + z_{trans} + (2 \times t_{tank}) \tag{2.20}$$

where X_{trans}, Y_{trans}, and Z_{trans} represent transformer dimensions and clearances ($d_1 - d_4$) are as shown in Fig. 2.13. Therefore, the volume of the tank is calculated as follows:

$$V_{tank} = X_{tank} \times Y_{tank} \times Z_{tank} = 3.442 \times 2.498 \times 1.814 = 15.6 \text{ m}^3 \tag{2.21}$$

The weight of the tank and the transformer oil are 1521 kg and 5447 kg, respectively.

As a result, the detailed loss, total size, and weight breakdown of MFTs are shown in Table 2.7 and Table 2.8.

Table 2.7: MMC MFT detailed losses at the rated power of 45.4 MW. The copper loss is calculated based on (2.15), and the core loss is calculated based on (2.9).

Copper loss (kW)	Core loss (kW)	Stray loss (kW)	Total losses (kW)
630.1	26.2	39.3	695.6

Table 2.8: MMC MFT size and weight breakdown

Transformer size (m^3)	Copper weight (ton)	Core weight (ton)	Tank weight (ton)	Oil weight (ton)
15.6	3.85	16.79	1.52	5.45

The total size, weight, and loss of the transformers are summarized in Table 2.9. In addition, the loss, size, and weight of power converter parts are also shown. Besides the size and weight information of power converter and MFTs, the chiller's information is also presented.

To cool down the cooling liquid used in the heatsink and the medium frequency transformer, a chiller is needed. The chiller size and weight are considerable and need to be added. According to the product data from DeltaTemp [91], it is possible to derive

Table 2.9: Total loss, size, and weight of SST. All values are shown for three topologies: MMC-SST (400 Hz), MMR (1000 Hz), and ISOP (1000 Hz).

Category	MMC-SST (400 Hz)	MMR (1000 Hz)	ISOP (1000 Hz)
Power converter loss (kW)	888.5	751.5	481.5
Transformer loss (kW)	695.6	817	806.3
Converter size (m^3)	43	39.9	8.94
Transformer size (m^3)	15.6	10.44	13.78
Chiller size (m^3)	78	77.45	64.24
Converter weight (ton)	7.2	5.76	2.4
Transformer weight (ton)	27.6	16.35	28.8
Chiller weight (ton)	14.6	14.5	11.98

curve-fitting models that correlate size and weight with cooling capacity. Curve-fitting expressions can be formulated as follows:

$$\textit{chiller size}\,(\mathrm{m}^3) = 4.7\times10^{-5}\times P(\mathrm{W}) + 6.015 \tag{2.22}$$

$$\textit{chiller weight}\,(\mathrm{kg}) = 8.974\times10^{-3}\times P(\mathrm{W}) + 870.4 \tag{2.23}$$

The total power loss P requiring liquid cooling amounts to 1534.6 kW, comprising 839 kW from converter loss (MMC and secondary DRU) and 695.6 kW from MFT loss. Thus, the required chiller cooling capacity is 1534.6 kW, and its corresponding size and weight are estimated to be 78 m^3 and 14.6 tons, respectively.

2.2.5 Performance Metrics at Different Frequencies

Following a similar design process as shown above, the losses, sizes, and weights at different frequencies of the MMC-SST topologies are shown in Fig. 2.16(a). In the comparative analysis of frequency response, note that for the transformer, only active parts (core and windings) are considered since this simplification is used to ensure manageable computations. For a similar reason, though the converter tower will be different for each analyzed frequency, most of the size changes come from the capacitor size differences between frequencies. Thus, only the capacitors are included to represent the dimensions of the converter parts.

As depicted in Fig. 2.16(a), the optimal frequency for the MMC-SST varies with respect to loss, weight, and size. The primary objective of using SST is to reduce the size and weight compared to traditional line frequency transformer-based converter topologies. This reduction is particularly advantageous in high-power applications, as it minimizes the physical footprint of installations where land and space usage can be costly. Therefore, in our optimal design considerations, size and weight are prioritized over losses. Consequently, the most suitable operating frequency for the MMC-SST has been identified as approximately 400 Hz. At this frequency, the design achieves the smallest size and very low weight while maintaining relatively low losses.

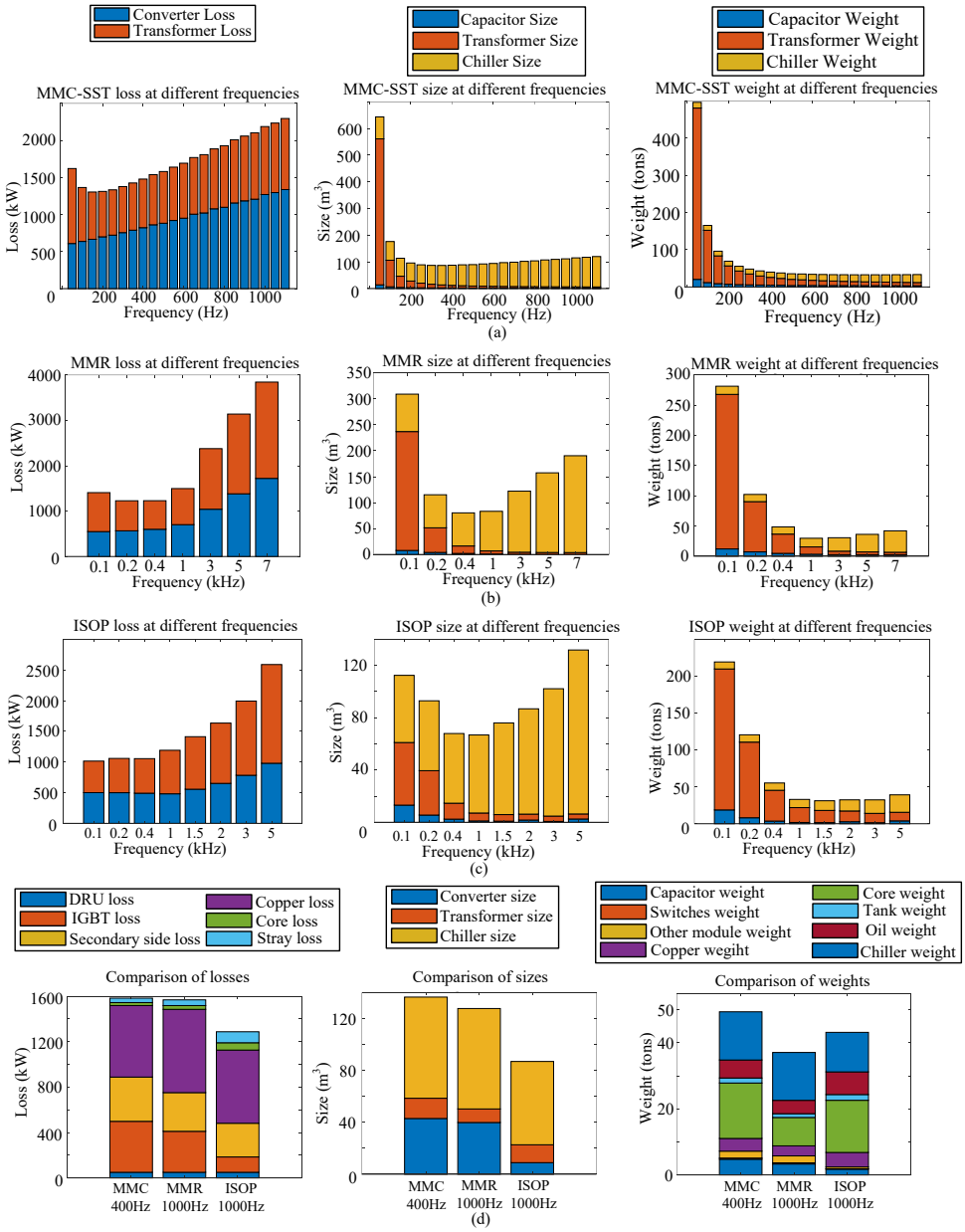


Figure 2.16: (a) MMC-SST (b) MMR (c) ISOP loss, size, and weight at different frequencies. In these figures, for transformer loss, size, and weight estimations, only the active parts are considered for simplicity. For the converter section, the focus is on the changes in size and weight of the capacitor, which are influenced by variations in frequency. Changes in other components are considered minimal and thus not accounted for in this analysis. (d) Topologies comparison results. The optimal operating frequencies for the MMC-SST, MMR, and ISOP are 400 Hz, 1000 Hz, and 1000 Hz, according to (a), (b), and (c).

2.3 Performance Metrics for Modular Multi-Level Resonant-Based Solid-State Transformer

This Section applies the same performance evaluation framework to the MMR-SST. The loss, size, and weight of the power converters and the medium-frequency transformer are analyzed and compared across different operating frequencies to identify the optimal design point.

2.3.1 Loss, Size, and Weight Estimation of the Power Converters

As mentioned in the introduction, the differences between MMR and MMC are inserted resonant capacitors and modulation methods. The Quasi Square Wave modulation method for the MMR is depicted in Fig. 2.17. The complete MMR model, constructed in Simulink, showcases key waveforms in Fig. 2.18, with Fig. 2.18(a) specifically illustrating the resulting arm voltages.

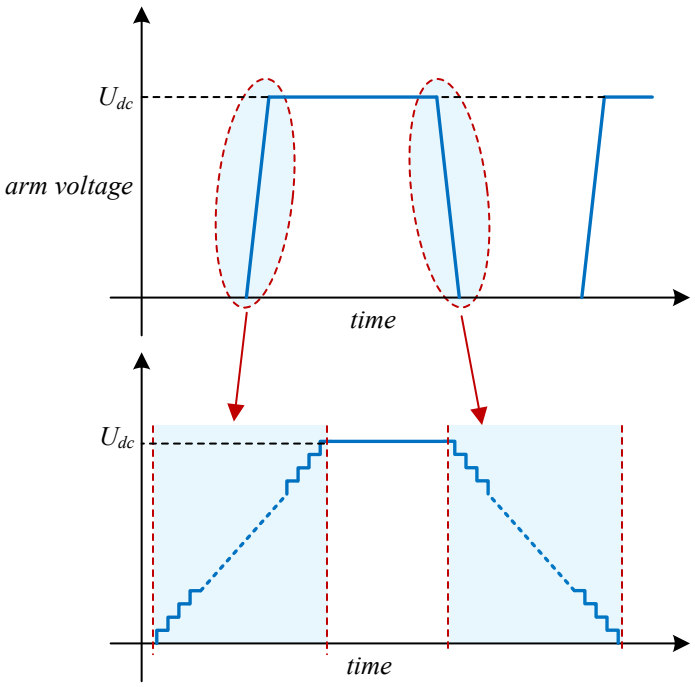


Figure 2.17: Quasi Square Wave modulation method. U_{dc} represents the input DC voltage. The generated staircase waveforms are designed to emulate those from two-level soft-switching converters, ensuring that the operating principles of the MMR align with those of the two-level, soft-switching LLC converters.

In theory, for MMR, primary side switches can achieve ZVS, and secondary side diodes can achieve ZCS, but because of the MMC arm current DC bias, the switching losses will exist, as witnessed in the following loss analysis.

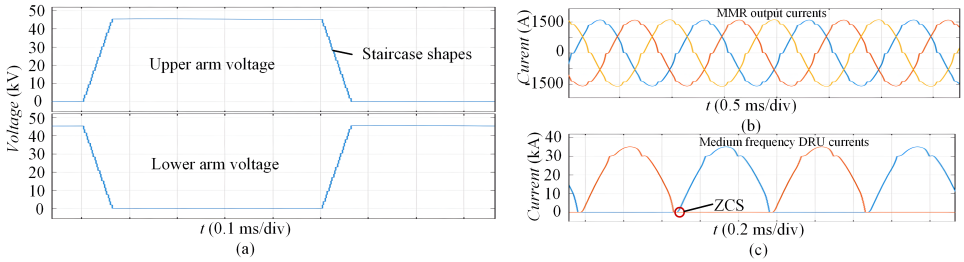


Figure 2.18: Key waveforms of the MMR: (a) phase A upper and lower arm voltages displaying staircase edges, according to the modulation method in Fig. 2.17, (b) MMC output currents with low THD, and (c) medium frequency DRU current exhibiting zero current switching. Additionally, the submodule voltages are balanced similarly to Fig. 2.5(a), and the electrolyzer input currents are maintained within a 3% current ripple band, as shown in Fig. 2.5(c).

The overall configuration of the MMR with the secondary side DRUs is shown in Fig. 2.2. In contrast to the MMC-SST, which employs a YdDd medium frequency transformer configuration to mitigate MMC output current harmonics and associated module losses, the MMR adopts a DdDd configuration. This shift is primarily due to the theoretical expectation that resonant and total MMC output currents in the MMR are sinusoidal, eliminating the necessity for a twelve-pulse configuration. Moreover, manufacturing simplicity is achieved as both medium-frequency transformers share the same configuration. Ideally, a YdYd transformer configuration would be preferable for high input voltage to low output voltage applications. However, according to [92], the resonant current in a three-phase Yd resonant converter is not sinusoidal and contains significant harmonics, adversely affecting MMC loss reduction.

According to simulations, the DdDd configuration ensures minimal THD in resonant currents, thus making it the preferred choice for reducing MMC losses.

The resonant passive components design methods are referred to two-level LLC converters [93]. The transformer designs will be different from the MMC-SST transformers. Dd transformer turn ratio $U_{\text{electrolyzer}}$ is calculated as [94]:

$$n_1 = \frac{U_{dc}}{U_{electrolyzer}} \tag{2.24}$$

where $U_{\text{electrolyzer}}$ represents electrolyzer rated input voltage. The turn ratio is tuned slightly considering output voltage safety room, and the resulting turn ratio of Dd transformer is 52. The parameters of the MMR modules remain the same as those of MMC-SST, e.g., submodule capacitance, number of submodules, etc.

For the power converter loss estimation, the front side twelve pulse DRU losses remain the same as MMC-SST. However, for MMC in MMR, the switching losses will be different because of the soft switching mechanism, and the conduction losses are also different because of different current waveforms. The following theoretically calculate the losses of MMR. For Dd transformer, secondary side current and voltage peak values can be calculated as:

$$U_{\text{sec-ph-peak}} = U_{\text{sec-LL-peak}} = \frac{\pi}{3} \times U_{\text{electrolyzer}} \tag{2.25}$$

$$I_{\text{sec-line-peak}} = \sqrt{3} \times I_{\text{sec-ph-peak}} = \frac{\sqrt{3} \times P_{\text{total}} \times 2}{U_{\text{sec-ph-peak}} \times 3} \tag{2.26}$$

The primary side voltage and current are calculated as:

$$U_{\text{pri-ph-peak}} = U_{\text{sec-ph-peak}} \times n_1 \tag{2.27}$$

$$I_{\text{pri-line-peak}} = \sqrt{3} \times I_{\text{pri-ph-peak}} = \frac{\sqrt{3} \times P_{\text{total}} \times 2}{U_{\text{pri-ph-peak}} \times 3} \tag{2.28}$$

As a result, the primary side line current peak value is calculated as 702 A. The total output current of MMC is:

$$I_{\text{total}} = 1404 \cos(\omega t + \varphi_1) \tag{2.29}$$

At the resonant frequency, the LLC resonant circuit is inductive, thus, the MMC output current phase angle should be slightly behind the output square voltage. With a suitable design, the delay angles will not be far from 0°, as seen from the literature [61]. For the convenience of theoretical loss analysis, MMC phase current is assumed to be:

$$I_{\text{total}} = 1404 \cos(\omega t) \tag{2.30}$$

Thus, the current is in phase with the MMC output square waves. The upper and lower arm currents of phase A are:

$$\begin{aligned} i_p &= \frac{I_{dc}}{3} + \frac{I_{total}}{2} = 328 + 702 \cos(\omega t) \\ i_n &= \frac{I_{dc}}{3} - \frac{I_{total}}{2} = 328 - 702 \cos(\omega t) \end{aligned} \tag{2.31}$$

The key waveforms and the corresponding primary-side notations of the circuits are shown in Figs. 2.19 and 2.20. For simplicity, only one phase is shown.

As seen from Fig. 2.20, the currents are symmetrical for the upper and lower arms, so only the upper arm losses are calculated, and the losses are multiplied by the number of arms. Since the current expressions for the upper and lower arms have been derived above, the conduction losses can be calculated using the same method as MMC-SST.

As for switching losses, for i_{1a} and i_{1b}, six circles have been marked on the waveforms for the switching instances. Because of the DC current bias, switching losses will occur compared with a normal two-level resonant converter. The following analyses these 6 switching instances. For i_{1b}, the current completely goes through the IGBT of S_{1b}. At instance 1, the IGBT turns on with non-ZVS, and at instance 2, the IGBT turns off with non-ZCS. For i_{1a}, at instance 3, the diode of S_{1a} turns on, however, the turn-on losses of the diodes are usually omitted. At instance 4, the diode of S_{1a} turns off, and the IGBT of S_{1a} turns on with ZVS. At instance 5, the IGBT of S_{1a} turns off with ZCS, and the diode of S_{1a} turns on. At instance 6, the diode of S_{1a} turns off with reverse recovery losses. The current values can be calculated at each instance, and the turn-on, turn-off, and reverse recovery energies can be referred to in the datasheet. The switching losses are computed by those energy losses multiplied by the switching frequency.

As for the secondary side DRU, because of the working principle of the resonant converter, there is no reverse recovery of the diodes, thus, only the conduction losses of

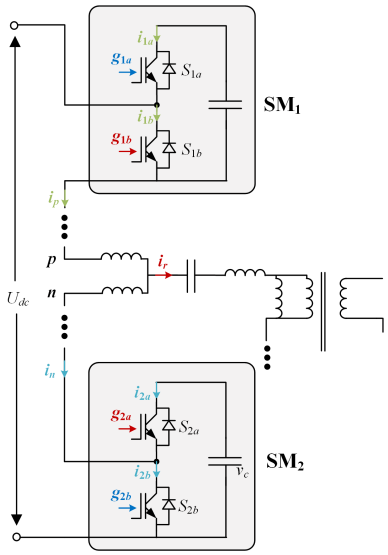


Figure 2.19: MMR primary side notations. For simplicity, only one submodule in each arm for one phase is shown. S_{1a} and S_{1b} denote the upper and lower IGBT modules of SM1, respectively, while g_{1a} and g_{1b} correspond to their gate signals. S_{2a}, S_{2b}, g_{2a}, and g_{2b} are similarly defined for SM_2. i_p, i_n, and i_r refer to the upper arm, lower arm, and resonant currents, respectively.

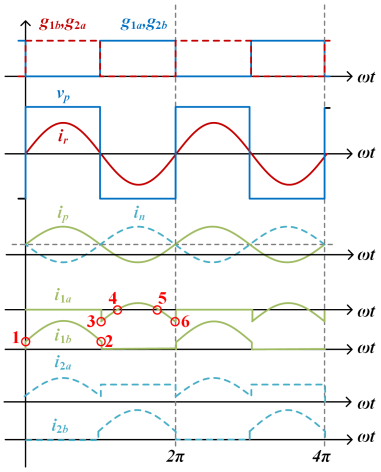


Figure 2.20: Key waveforms of the primary side converter corresponding to Fig. 2.19. Six switching instances are marked consecutively for upper arm submodule for theoretical loss analysis and calculation.

the diodes are considered. Because the primary side resonant current is pure sinusoidal at the resonant frequency, and the magnetizing inductance is much higher than the leakage inductance of the MFT, the secondary side current is also assumed to be sinusoidal. The conduction losses calculation method of the secondary side DRU is the same as that of MMC-SST. As a result, the conduction losses, switching losses of MMC, and the conduction losses of secondary side DRU are 191 kW, 68 kW, and 341 kW, respectively, for 400 Hz. For 1000 Hz, only the switching losses of the MMC will change to 170 kW, and others will remain unchanged

As a result, a summary of the losses of different components at 1000 Hz is shown in Table 2.10.

Table 2.10: MMR converter detailed losses at the rated power of 45.4 MW

DRU loss (kW)	MMC loss (kW)	Secondary side DRU loss (kW)	Total loss (kW)
49.5	361	341	751.5

Fig. 2.18(b) displays the simulated MMR output currents, which deviate slightly from a perfect sinusoidal shape due to the delay angle introduced by the Quasi Square Wave modulation. Fig. 2.18(c) presents the medium frequency DRU current, clearly exhibiting ZCS characteristics. The model's behavior aligns closely with theoretical analysis.

The following size and weight estimations are based on 1000 Hz operating frequency, as the next Section shows that the best frequency for MMR is 1000 Hz. Submodule capacitance installed in the 1000 Hz MMC is estimated as $1.45\,\text{mF} \times 400/1000 = 0.58\,\text{mF}$, where 1.45 mF is the capacitance value used in the 400 Hz MMC-SST. The capacitor size and weight for 0.58 mF MMC are estimated as $6 \times 10^{-3}\,\text{m}^3$ and 23 kg, based on (2.3) and (2.4). The switches' size and weight remain unchanged, at $1.56 \times 10^{-3}\,\text{m}^3$ and 2.4 kg. Assuming the weight and volume of other module components remain the same as the 400 Hz MMC submodule, the submodule size is $0.031\,\text{m}^3$, and the submodule weight is 40 kg. The total submodule weight of the MMC converter is 5.76 ton. The submodule block dimensions are assumed to be 0.35 m (length) × 0.3 m (width) × 0.3 m (height). The insulation design is similar to the MMC-SST, and the 3D modelling will not be repeated here for simplicity. The insulation distances d_1, d_2, d_3, and d_4 defined in Subsection 2.2.3 are the same as MMC-SST. However, due to the smaller submodules, the total size is different from MMC-SST, and the total size of the MMR converter is $6.29\,\text{m} \times 3.22\,\text{m} \times 1.97\,\text{m} = 39.9\,\text{m}^3$. Table 2.11 summarizes the MMR converter's size and component weights.

Table 2.11: MMR converter detailed size and weight

MMC size (m^3)	Capacitor weight (ton)	Switches weight (ton)	Other Module Weight (ton)
39.9	3.312	0.3456	2.1

2.3.2 Design of the Medium-Frequency Transformer for MMR

The MMR topology has two Dd MFTs. The voltage and current of the transformers are measured in the Simulink model.

For the Dd transformer of the MMR topology, (2.8) can be written as

$$A_c = \frac{\int u_{\text{pri-ph}}(t)\,\mathrm{d}t}{2N_p k_c B_m}, \tag{2.32}$$

where the integral of $u_{\text{pri-ph}}(t)$ is taken over the positive half-cycle of the primary phase voltage.

For the present design, the applied volt-second is $\int u_{\text{pri-ph}}(t)\,dt = 9.28\,\text{V}\cdot\text{s}$, with $N_p = 104$ and $N_s = 2$. The remaining core sizing and winding design procedures follow the same methodology as that used for the MFTs in the MMC-SST and are therefore not repeated here.

The physical structure of MMR MFT is similar to MMC-SST MFT, where there are also two active parts inside one tank, and rating power and voltages are similar.

The FEM simulation results of MMR MFT are summarized in Table 2.12.

Table 2.12: FEM results for MMR MFTs

Frequency	Configuration	Parameter	Value
1000	Dd	L_{lk}	3.762 mH
		r_{p}	2970.4 μΩ/m
		r_{s}	71.761 μΩ/m

The MFT detailed loss is summarized in Table 2.13, and the size and weight breakdown information is summarized in Table 2.14.

Table 2.13: MMR MFT detailed losses at the rated power of 45.4 MW

Copper loss (kW)	Core loss (kW)	Stray loss (kW)	Total losses (kW)
733.5	33.5	50.25	817

Table 2.14: MMR MFT detailed size and weight

Transformer size (m^3)	Copper weight (ton)	Core weight (ton)	Tank weight (ton)	Oil weight (ton)
10.44	3.04	8.6	1.15	4.04

The loss, size, and weight information for power converter, MFTs, and chiller for MMR at 1000 Hz are summarized in Table 2.9.

2.3.3 Performance Metrics at Different Frequencies

Following a similar analysis process, the losses, sizes, and weights at different frequencies of the MMR topologies are shown in Fig. 2.16(b). As shown in Fig. 2.16(b), the optimal fundamental frequency for the MMR topology is identified as approximately 1000 Hz, prioritizing size and weight reduction as key design targets. The frequency sweep range for MMR is different from MMC-SST as shown in Fig. 2.16(a), because the analysis aims to identify the optimal frequency corresponding to the turning point. Due to the soft switching characteristics of MMR, it is necessary to consider a broader frequency range. This approach ensures that the optimal frequency is accurately determined. A similar rationale applies to the frequency sweep range analysis for the ISOP topology.

2.4 Performance Metrics for Input-Series Output-Parallel Solid-State Transformer

This Section extends the performance evaluation framework established in previous Sections to the ISOP-SST. Following the same methodology, the converter and medium-frequency transformer are designed and assessed in terms of loss, size, and weight, providing a consistent basis for comparison with the MMC- and MMR-based solutions.

2.4.1 Loss, Size, and Weight Estimation of the Power Converters

As discussed in the introduction, LLC is more suitable than DAB for this unidirectional application scenario. At the initial stage of the design, the single-phase LLC was chosen as the sub-module for the ISOP. Although this topology offers better scalability, it has notable disadvantages. Firstly, three single-phase transformers are heavier and larger compared to a three-phase transformer with the same voltage level and capacity. Secondly, compared with multi-phase implementations, the single-phase LLC inherently exhibits a pronounced second-order ripple current at the rectifier output, which necessitates a significantly larger output filter capacitance.

An alternative topology is shown in Fig. 2.21. Full bridge inverters are used because of the high-power requirement of modules. The voltage rating of the switches remains the same as the MMC-SST, i.e., 3.3 kV IGBT with a derated safety voltage of 2 kV. The number of cascaded full bridges is $N = \text{ceil}(U_{\text{dc}}/U_{\text{IGBT_derated}}) = 24$.

Instead of using the variable frequency modulation method to change the output voltage, the phase shift modulation (PSM) method is adopted in this study. The delay angle between the leading bridge and the following bridge is controlled to modify the output voltage [95]. In this way, the transformer design is less challenging than variable frequency modulation, because the transformer needs over-design for the latter to cover the whole operating frequency range.

Since the full bridges are grouped in sets of three, there are eight three-phase LLC converters whose inputs are connected in series. Four of these three-phase LLC converters are output parallel connected to one electrolyzer, and the remaining four are connected to another.

The following part analyses the three-phase LLC with 1000 Hz operating frequency since the next Section shows that the topology's best operating frequency is around 1000 Hz.

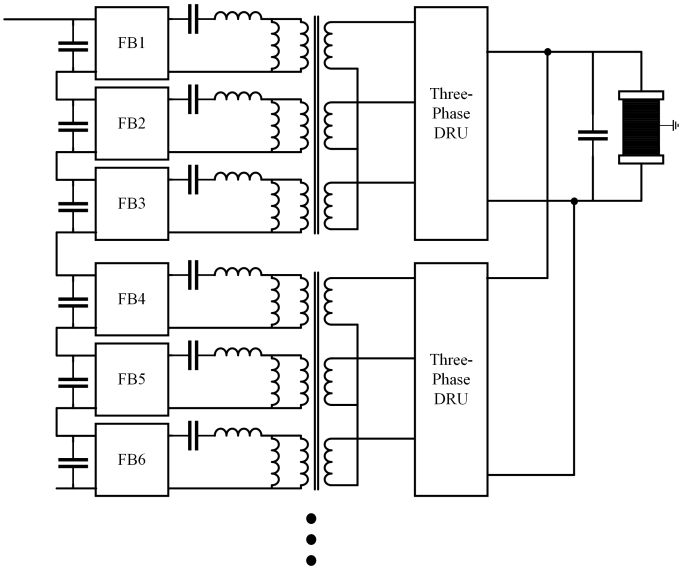


Figure 2.21: Three-phase ISOP system. Three-phase LLC submodules are connected together to form an ISOP configuration. The primary side of these three submodules is shifted with a 120° phase delay. FB represents full bridge modules.

Only one three-phase LLC submodule is built in Simulink, because in steady-state operation, all three-phase LLC submodules should work in the same condition. The designed resonant inductance is 0.11 mH, the magnetizing inductance is 0.038 H, and the resonant capacitance is 0.22 mF to have a 1000 Hz resonant frequency. The resonant inductance and magnetizing inductance come from the medium frequency transformer. Based on the same design methodology of switches as MMC-SST topology, the primary side inverter switches are chosen as 5SNA 1800E330400 with a voltage rating of 3.3 kV and current rating of 1.8 kA, according to the measured current flowing through the switches. The secondary side diode is chosen as 5SDF28L4521, with three of them in parallel to handle high currents. The input DC capacitance for each full bridge inverter is set as 2.4 mF to limit the voltage ripple, and the output capacitance is set as 32 mF to meet the electrolyzer's 3 % current variation requirement. To validate these design choices and demonstrate the system's operational efficacy, the corresponding simulation waveforms are presented in Fig. 2.22. Specifically, Fig. 2.22(a) illustrates the sinusoidal resonant current waveforms, while Fig. 2.22(b) showcases the medium frequency DRU current, which clearly exhibits ZCS characteristics.

Thermal modeling is done for three-phase modules. The resulting losses are multiplied by the number of three-phase modules, i.e., $n_{3\text{ph}} = 8$. The input 50 Hz DRU losses are directly taken from MMC-SST since both ISOP and MMC-SST have the same input 12-pulse DRU design. As a result, a summary of the losses of different components is shown in Table 2.15.

The resonant capacitor size and weight estimation are based on the manufacturer datasheet [96]. The size and weight of it are 0.02 m^3 and 28 kg, respectively. The switches'

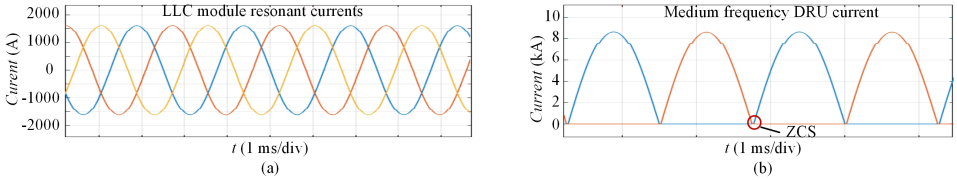


Figure 2.22: Key waveforms of the ISOP for one LLC submodule: (a) three-phase resonant currents displaying a highly sinusoidal shape, and (b) medium frequency DRU current demonstrating zero current switching. Additionally, the electrolyzer input currents are consistently maintained within a 3 % current ripple band, similar to that depicted in Fig. 2.5(c).

Table 2.15: ISOP converter detailed losses at the rated power of 45.4 MW

DRU loss (kW)	IGBT loss (kW)	Secondary side DRU loss (kW)	Total loss (kW)
49.5	135	297	481.5

size and weight are 0.003 m^3 and 4.8 kg, respectively. And the input capacitor of 2.4 mF size and weight are estimated as 0.0225 m^3 and 44 kg, based on Equations (2.3) and (2.4). Adding the size of IGBT and capacitors and leaving margins for other components, the submodule size and weight are estimated as 0.08 m^3 and 100 kg, respectively. The weight value is multiplied by 24 full bridge modules, and the total weight of the submodules is estimated to be 2.4 tons.

An insulation design is accomplished for ISOP, as shown in Fig. 2.23. The red and blue cylinders represent $+DC$ and $-DC$ inputs, respectively. The submodule block dimensions are assumed to be 0.5 m (length) × 0.4 m (width) × 0.4 m (height). Three insulation distances, d_1, d_2, and d_3, have been considered, and the method is the same as MMC-SST, which will not be repeated here. As a result, the total size for the valve tower of ISOP is 0.94 m × 3.15 m × 3.02 m = 8.94 m^3. Table 2.16 shows a summary of the ISOP converter's size and component weight.

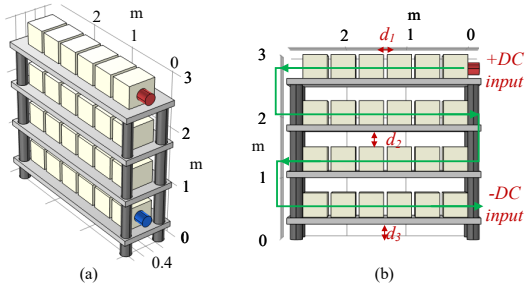


Figure 2.23: ISOP converter 3D modelling (a) overall structure, (b) side view. There is one converter tower with four rows, each with eight modules.

Table 2.16: ISOP converter detailed size and weight

ISOP converter size (m^3)	Capacitor weight (ton)	Switches weight (ton)	Other Module Weight (ton)
8.94	1.73	0.115	0.557

2.4.2 Design of the ISOP MFT

The transformer design for this case uses a method similar to the MMR and MMC-SST. However, the number of transformers here is eight. The converter has a square-shaped voltage waveform; thus, the peak voltage must be considered ($U_{\text{pri-ph-peak}} = 3260\,\text{V}$). The number of turns in primary and secondary are 10 and 2, respectively. The ISOP is a resonant LLC topology, and it is beneficial to use the leakage inductance of the MFT as the resonant inductor; therefore, the primary and secondary windings are located on top of each other to maintain the desired high leakage inductance, as shown in Fig. 2.24(a). Another difference is that the ISOP MFT is a shell-type transformer because building the windings as similar as possible is essential, mainly regarding the leakage and magnetizing inductances. Using a shell-type transformer guarantees that the leakage inductances remain similar. The shell-type ISOP MFT is shown in Fig. 2.24(b).

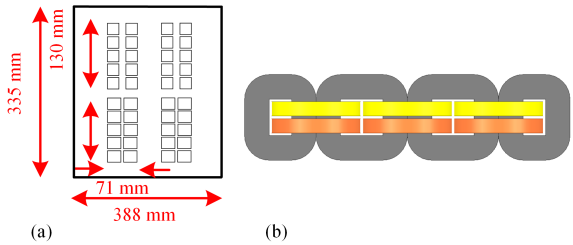


Figure 2.24: Details of the ISOP transformer design: (a) ISOP MFT window, (b) ISOP shell-type transformer with windings on top of each other

The cross-section of the core for the MFT at 1000 Hz is:

$$A_c = \frac{U_{pri\text{-}ph\text{-}peak}}{k_c \times k_w \times B_m \times f \times N_p} = \frac{3260}{0.79 \times 4 \times 1.26 \times 1000 \times 10} = 0.082\,\text{m}^2 \tag{2.33}$$

Therefore, the core is selected as $2 \times 170.2 \times 240$ mm. The primary and secondary currents are $I_p = 1334\,\text{A}$ and $I_s = 6465\,\text{A}$, respectively. Therefore, $\text{CTC}_{pri} = 21 \times 13 \times 2 = 546\,\text{mm}^2$, and $\text{CTC}_{sec} = 5 \times 21 \times 16 \times 2 = 3360\,\text{mm}^2$ (there are five parallel paths on the secondary side). A 3D view of the ISOP MFT is shown in Fig. 2.25(a).

Insulation and Thermal Considerations

The insulation and thermal considerations for ISOP MFT are similar to those for MMC-SST and MMR. To decrease the insulation stress, the cores are clamped to the middle point of the input DC bus and insulated from the tank accordingly. There are eight active parts inside one tank, as shown in Fig. 2.25(b) and Fig. 2.25(c).

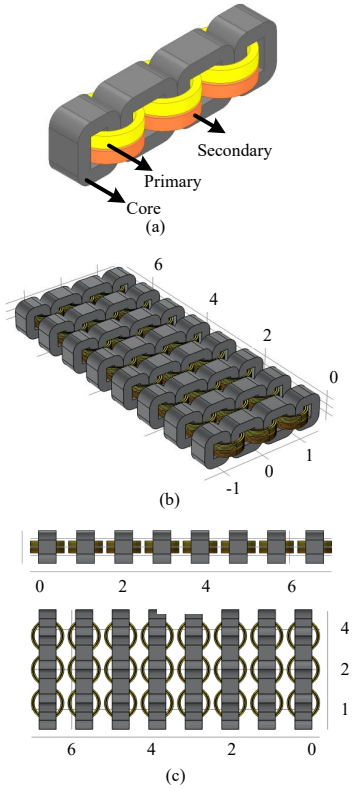


Figure 2.25: The ISOP MFT: a) the 3D view of one MFT, b) the 3D view of the eight MFTs inside the tank, and c) the side views

Overall Metrics of the ISOP MFT

The transformers' detailed loss, total size, and weight breakdown are shown in Table 2.17 and Table 2.18. The FEM simulation results for ISOP MFT are summarized in Table 2.19.

Table 2.17: ISOP MFT detailed losses at the rated power of 45.4 MW

Copper loss (kW)	Core loss (kW)	Stray loss (kW)	Total losses (kW)
644.8	64.6	96.9	806.3

The loss, size, and weight information for the power converter, MFTs, and chiller for ISOP at 1000 Hz are summarized in Table 2.9.

2.4.3 Performance Metrics at Different Frequencies

Following a similar analysis process, the losses, sizes, and Weights of the ISOP topologies at different frequencies are shown in Fig. 2.16(c). Due to the ZVS turn-on characteristics, turn-

Table 2.18: ISOP MFT detailed size and weight

Transformer size (m^3)	Copper weight (ton)	Core weight (ton)	Tank weight (ton)	Oil weight (ton)
13.78	4.4	15.8	1.74	6.86

Table 2.19: FEM results for ISOP MFTs

Frequency	Parameter	Value
1000 Hz	L_{lk}	110.4 μH
	r_p	475.5 $\mu\Omega$/m
	r_s	88.9 $\mu\Omega$/m

on losses are effectively eliminated. However, turn-off losses are still present and contribute to the overall power loss observed in the converter. As a result, the converter power loss fluctuates between different frequencies, as observed in Fig. 2.16(c). As indicated in Fig. 2.16(c), the optimal fundamental frequency for the ISOP topology is set at approximately 1000 Hz, with a primary focus on reducing size and weight.

2.5 Topologies Comparison Results

Section 2.2–2.4 have thoroughly detailed the design processes for the MMC-SST, MMR-SST, and ISOP-SST, respectively, with summarized results presented in Fig. 2.16. To determine the most suitable topology for electrolyzer applications, this Section begins with a frequency sweep analysis for each topology. Subsequently, a comparison of the three topologies at their optimal operating frequencies is performed.

2.5.1 Frequency Sweep Analysis

Fig. 2.16(a)–(c) illustrates the frequency sweep analyses for MMC-SST, MMR, and ISOP topologies, focusing on their loss, size, and weight characteristics. In all three topologies, converter and transformer losses each account for approximately half of the total losses. Specifically, due to the hard switching operation of the MMC-SST, converter losses increase linearly with the operating frequency as the switching losses are directly proportional to frequency. In contrast, for MMR and ISOP, which feature soft-switching characteristics, converter losses are significantly reduced. However, switching losses are not completely eliminated. For MMR, due to the DC bias of the MMC arm current, switching losses persist, as detailed in the loss analysis in Subsection 2.3.1. For ISOP, while Zero-Voltage Switching (ZVS) turn-on characteristics eliminate turn-on losses, turn-off losses remain. Consequently, within a certain frequency range, here identified as 1000 Hz, converter losses are maintained at a relatively low level. Beyond this frequency, however, converter losses increase sharply, pushing switch junction temperatures beyond safe operational limits.

In terms of transformer losses, the trend differs: losses initially decrease and then increase with rising frequencies. This is due to the reduction in core size with higher fre-

quencies, which lowers core losses and reduces the Mean Length per Turn, thus decreasing copper losses. However, increased frequencies also intensify losses in the windings due to the proximity effect and skin effect, causing transformer losses to vary with frequency.

In terms of size and weight trends, there is a discernible pattern where both transformer size and weight are inversely proportional to the operating frequency. For MMC-SST, beyond approximately 400 Hz, and for MMR and ISOP, beyond around 1000 Hz, the transformer size becomes negligible compared to that of the chiller. In these three topologies, transformer weight is typically the dominant factor; however, at higher frequencies, the weight of the chiller becomes increasingly significant. Regarding the converter section, attention is given to how changes in frequency affect the size and weight of capacitors. In this frequency sweep analysis, the impact of capacitor size and weight is minimal and does not significantly influence the determination of the optimal operating frequency.

2.5.2 Analysis of Topologies at Optimal Frequencies

As detailed in Subsections 2.2.5, 2.3.3, and 2.4.3, when prioritizing size and weight reduction, the optimal operating frequencies for the MMC, MMR, and ISOP topologies have been identified as 400 Hz, 1000 Hz, and 1000 Hz, respectively. Fig. 2.16(d) presents a comparison of these topologies' performance metrics at their respective optimal frequencies.

Among the designs evaluated, the MMC-SST is the bulkiest and heaviest, and it also exhibits the highest energy losses. In contrast, the ISOP-SST and MMR-SST excel in different aspects: the ISOP-SST achieves the lowest losses and is the most compact, while the MMR-SST is distinguished by having the lowest weight.

In terms of loss comparison, transformer copper loss constitutes a significant portion of the total losses. The MMR and ISOP experience higher copper losses than the MMC-SST due to their higher operating frequencies, which intensify the proximity effect. Regarding IGBT losses, the ISOP-SST benefits from reduced switching losses owing to its soft-switching capabilities. In contrast, the MMR-SST does not achieve full soft switching, attributed to the DC bias in its arm current. Concerning conduction losses, the different current ratings of the IGBTs used lead to variations: ISOP employs 1800 A IGBTs due to higher current requirements, whereas MMR uses 1200 A IGBTs. Consequently, the total losses for MMC-SST and MMR are comparable, while the total loss for ISOP is slightly lower.

In all three topologies, the chiller size is a dominant factor. The ISOP-SST stands out for its compactness, largely due to its reduced module count, resulting in smaller converter towers. Specifically, the MMR topology requires 144 submodules distributed across multiple racks, necessitating ample space between racks for maintenance. In contrast, the ISOP system comprises only 24 modules, which can be accommodated within a single rack. This configuration significantly reduces the required insulation and maintenance space, as illustrated in Fig. 2.23, thereby minimizing the overall size of the converter compared to the other two scenarios.

Regarding weight, the chiller and core weights are significant factors across all three topologies. The MMR topology features a notably lighter core, achieved by using only two 1000 Hz transformers, as opposed to the eight utilized in ISOP-SST. This design choice reflects the principle that a single, larger transformer tends to be more weight-efficient than multiple smaller units, offering substantial weight savings.

2.6 Conclusion

This Chapter comprehensively designs and compares the MMC-based, MMR-based, and ISOP SST for electrolyzer applications from the efficiency, size, and weight points of view. The sizes of the converter towers and transformers are calculated by explicitly accounting for insulation distance requirements.

Based on the detailed analysis provided, five key findings emerge:

1. The analysis emphasizes the critical role of chiller size and weight in evaluating each topology, underscoring the importance of considering these factors in size and weight comparisons.
2. The adoption of a soft-switching topology is recommended to achieve lower converter losses, which in turn reduces the size and weight of the chiller due to decreased cooling requirements.
3. A lower number of submodules typically necessitates reduced insulation and maintenance space, consequently diminishing the overall size of the converters.
4. Topologies utilizing a central transformer generally exhibit lower transformer size and weight compared to those employing multiple smaller transformers.
5. Within the specific application context and ratings investigated, the ISOP-SST emerges as the optimal choice for applications where space conservation is crucial, whereas the MMR-SST is found to be more suitable for scenarios where minimizing weight is a critical consideration.

While the design procedures and evaluation work in this study were conducted under specific parameters, the analytical framework employed for calculating and comparing losses, size, and weight across different topologies, especially through the frequency sweep method, demonstrates high adaptability. This versatility enables the framework to be effectively applied to various system parameters, offering a robust guideline for adapting to diverse operational conditions and application scenarios.

3

Control Strategy for Enhanced Performance of MMR-SST

This Chapter introduces a novel control strategy for Modular Multilevel Resonant converters (MMR) in Solid-State Transformer (SST) applications, with a focus on medium-voltage conversion for hydrogen electrolyzers. The Chapter first reviews voltage control methods in MMR, analyzing their operational principles, regulation capabilities, and impact on MMR efficiency. A continuous modulation index control method with double-step staircase waveform modulation is then proposed, simplifying the control scheme to a single control variable while maintaining robust controllability. By fixing the operating frequency at the resonant frequency, the transformer can be designed with a high magnetizing inductance, thereby reducing the magnetizing current. Additionally, using a small phase shift angle between Modular Multilevel Converters (MMC) submodules helps to lower the harmonic distortion of the resonant current. The proposed control strategy is validated through Simulink simulations and experimental results, demonstrating its simplified control structure and reduced total harmonic distortion.

This chapter is based on:

-**Z. Li**, R. Mirzadarani, J. van der Weg, W. Heyns, R. van der Sande, M. Ghaffarian Niasar, A. Shekhar, P. Bauer, and Z. Qin, "A control approach for performance improvement of MMR-based SST in H_2 electrolyzer applications," IEEE Journal of Emerging and Selected Topics in Power Electronics, under review.

3.1 Introduction

Green hydrogen is widely recognized as a key solution for advancing renewable energy integration and alleviating grid congestion [43, 44]. It is produced by electrolyzers supplied by renewable energy sources and can be utilized across multiple sectors, including transportation, industry, and power generation, while also serving as an environmentally friendly energy storage medium.

In large-scale electrolyzer applications, power conversion typically involves stepping down medium voltage to low-voltage DC using a transformer–rectifier system. Conventional solutions based on line-frequency transformers and diode or thyristor rectifiers [45] are cost-effective but result in bulky systems, making them unsuitable for applications with stringent size constraints.

Solid-state transformers (SSTs) provide a compact alternative for such size- and weight-sensitive applications, including traction systems [46], wind turbine nacelles [47, 48], and future naval vessels [49]. By converting line-frequency power to medium or high frequency using power electronic converters, SSTs enable voltage conversion and galvanic isolation with significantly reduced transformer size.

Among various SST topologies, cascaded structures are widely adopted due to their modularity and ease of control [51, 52], offering flexibility for different voltage and current requirements [97, 98]. However, the need for multiple low-power transformers with full DC voltage isolation substantially increases system volume, cost, and insulation complexity, limiting their suitability for high-voltage, high-power applications.

A viable approach to addressing these issues is the use of the modular multilevel converter (MMC) topology combined with a centralized transformer. In recent years, numerous studies have introduced MMC-based SST designs for medium voltage conversion, including configurations such as the dual-active-bridge (DAB) and resonant structures [99–101]. The centralized high-power transformer simplifies insulation and isolation, enhances power density, and eases production. Topologies' soft-switching capability enables higher operating frequencies, reducing transformer size and the volume of passive components.

The MMC-SST with a DAB structure functions similarly to a standard DAB, where output power is regulated by adjusting the phase shift between primary- and secondary-side AC voltages. This configuration is often referred to as a modular multilevel DAB (M2DAB) [58, 102–104]. However, M2DAB is not ideal for electrolyzer applications due to its excessive bidirectional capability and the higher costs associated with active switches on the secondary side.

The MMC with a resonant structure, known as the Modular Multilevel Resonant converter (MMR), is better suited for the electrolyzer application, as illustrated in Fig. 3.1. The MMR benefits from the wide soft-switching range of the LLC configuration and gains additional voltage control capabilities through the modular multilevel structure.

Various control methods have been proposed in the literature for regulating the MMR. For instance, [61, 105] combined the regulation of inserted submodules (SMs) with frequency variation control to achieve broad voltage regulation capabilities. However, this frequency regulation approach relied on a small transformer magnetizing inductance, resulting in high magnetizing currents, which can cause losses in both the transformer and MMC submodules. To mitigate this, [101] introduced the phase shift angle among MMC SMs as an additional control dimension for regulating voltage gain, alongside controlling the number of inserted

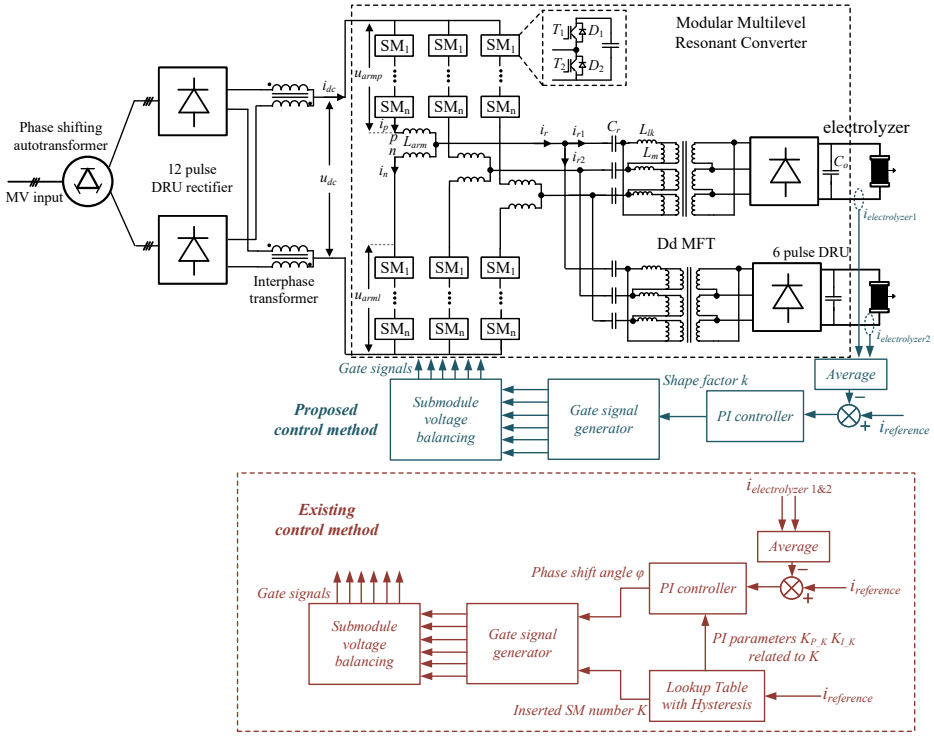


Figure 3.1: Modular Multilevel Resonant converter based Solid State Transformer. An autotransformer is used instead of an isolated transformer to generate a 30° phase shift angle for two DRUs, reducing both space and weight. Two resonant circuits are connected in parallel to supply power to two electrolyzer units. L_{arm}, L_{lk}, L_{m}, and C_{r} represent MMC arm inductance, MFT leakage inductance, MFT magnetizing inductance, and resonant capacitance, respectively. u_{dc}, i_{dc}, i_{p}, i_{n}, i_{r1}, i_{r2}, and i_{r} represent MMR input dc voltage, input dc current, MMR phase A upper arm current, lower arm current, the first MFT resonant current, the second MFT resonant current, and the total resonant current, respectively. The proposed control method regulates the output current using a single control variable k, whereas the existing control method employs two control variables, namely the phase-shift angle ϕ and the inserted submodule number K, to achieve the same objective. The existing control strategy and the proposed control strategy are detailed in Section 3.2.2 and Section 3.3, respectively.

SMs. This method fixes the operating frequency at the resonant frequency and allows for a transformer with a larger magnetizing inductance. Despite these improvements, the existing control methods involve multiple control loops, complicating the design of controller parameters.

To address this issue, this Chapter introduces a novel continuous modulation index control method utilizing a double-step staircase modulation waveform. This approach simplifies the control by using only a single control variable while maintaining equivalent controllability. By fixing the system's operating frequency to the resonant frequency, the transformer can be designed with a significantly higher magnetizing inductance, thereby reducing magnetizing current. Additionally, the phase shift angle between MMC submodules is set to a small, fixed value, resulting in lower resonant current distortion compared to existing phase shift control. This optimization leads to a potential reduction in total power losses at rated operating power, reducing the costs associated with the heatsink and chiller.

The remainder of this Chapter is organized as follows: Section 3.2 covers the basic operation and existing control principles of the MMR-SST. In Section 3.3, the proposed continuous modulation index control method and control loops are introduced. Section 3.4 validates the effectiveness of the proposed method through detailed simulations, comparing the efficiency, power losses, and THDi with those of existing approaches. Section 3.5 further demonstrates that the proposed simplified control strategy can be effectively implemented on the experimental platform, confirming the validity of the theoretical analysis. Finally, Section 5 concludes with the main findings and contributions of this work.

3.2 Basic Operation and Existing Control Method for MMR-SST

Section 3.2 introduces the fundamental operating principle of the modular multilevel resonant solid-state transformer and reviews existing control methods reported in the literature. The limitations of these conventional approaches, particularly in terms of control complexity and resonant current distortion, are highlighted to motivate the proposed strategy in the following Section.

3.2.1 Fundamental Operation Principle

Fig. 3.1 illustrates the Modular Multilevel Resonant Converter-based Solid-State Transformer (MMR-SST), which comprises two main components: the 12-pulse DRU rectifier and the MMR. The MMR consists of a three-phase MMC, three-phase medium frequency transformers, and secondary-side DRU rectifiers. A three-phase configuration is utilized due to its advantageous performance in terms of semiconductor and capacitor ratings, as well as the medium frequency transformer, as evidenced by a comparative study between three-phase and single-phase MMC-SST configurations [44, 106].

In the subsequent analysis, the parameters of the two MFTs are assumed to be identical, disregarding component tolerances.

The operating principle of the MMR resembles that of a two-level LLC converter. As depicted in Fig. 2.17, a quasi-square waveform modulation is employed to improve DC voltage utilization while simultaneously minimizing dv/dt. The resonant current i_r in

Fig. 3.1 is nearly sinusoidal, due to the LLC resonant unit. The arm currents, voltages, and resonant currents are described by the equations below [61]:

$$\begin{cases} u_p = u_{\text{arml}} - \frac{u_{\text{dc}}}{2} = \frac{u_{\text{dc}}}{2} - u_{\text{armp}} \\ i_p = \frac{i_r}{2} + \frac{i_{\text{dc}}}{3} \\ i_n = -\frac{i_r}{2} + \frac{i_{\text{dc}}}{3} \\ i_r = i_{r1} + i_{r2} \end{cases} \tag{3.1}$$

where u_p denotes the voltage applied to the resonant tank. A DC component is present in the MMC arm current. The MMR output resonant current i_r is evenly distributed between the upper and lower arms, and is also equally divided between the two MFTs, assuming that the resonant circuits' passive components are identical.

The equivalent First Harmonic Analysis (FHA) circuit model is depicted in Fig. 3.2.

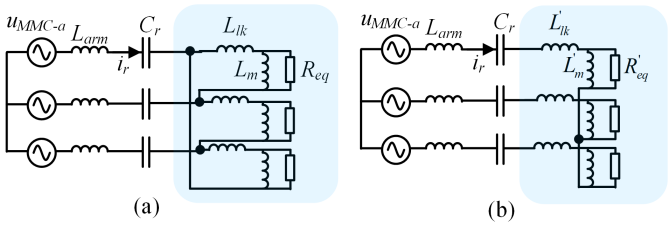


Figure 3.2: FHA circuit model of each Dd transformer: (a) the original D connection, (b) the equivalent Y connection

The primary side delta (Δ) connection shown in Fig. 3.2(a) is transformed into a Y connection as shown in Fig. 3.2(b). The parameters in Fig. 3.2(b) can be calculated as

$$\begin{cases} L'_{\text{lk}} = \dfrac{L_{\text{lk}}}{3} \\ L'_m = \dfrac{L_m}{3} \\ R'_{\text{eq}} = \dfrac{R_{\text{eq}}}{3} \end{cases} \tag{3.2}$$

where R_{eq} is the phase resistance, which can be calculated as [107]:

$$R_{\text{eq}} = \frac{18}{\pi^2} \left(\frac{N_p}{N_s} \right)^2 R_L \tag{3.3}$$

R_L denotes the electrolyzer load resistance during operation.

Therefore, for each resonant circuit, the LLC resonant inductance comprises the MMC arm inductance and MFT leakage inductance:

$$L_r = L_{\text{arm}} + L'_{\text{lk}} \tag{3.4}$$

The quality factor of the resonant circuit is defined as [93]:

$$Q_e = \frac{\sqrt{L_r / C_r}}{R'_{\text{eq}}} \tag{3.5}$$

where L_r represents the resonant inductance calculated by (3.4), C_r represents the resonant capacitance, and R'_{eq} represents the equivalent load resistance calculated by (3.3). The quality factor is a measure of the resonance selectivity of the circuit. A high quality factor results in a narrow resonant bandwidth and strong frequency selectivity, thereby enhancing the circuit's ability to reject current harmonics. This will be shown in Section 3.5.

According to (3.1), the primary operation waveform of the MMR is illustrated in Fig. 3.3, where the arm voltage is a trapezoidal wave and the arm current comprises a DC bias current and a sinusoidal resonant current, both proportional to the output power. Unlike traditional two-level LLC converters, the presence of DC bias current in the MMR inhibits full soft switching. The soft switching characteristics of the switches are detailed in Table 3.1 [101], where T_1, T_2, D_1, D_2 represent upper and lower transistors and diodes for one submodule as shown in Fig. 3.1, and D_{S1}–D_{S6} represent secondary side diodes.

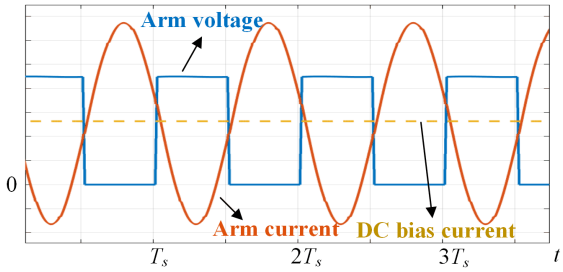


Figure 3.3: Phase-A total arm current (orange) and upper-arm voltage (blue) waveforms of the MMR-SST. The dashed yellow line indicates the DC circulating current component embedded in the arm current.

Table 3.1: MMR-SST soft-switching status

Device	T_1	T_2	D_1	D_2	D_{S1}–D_{S6}
Soft switching status	ZVS ON ZCS OFF	hard ON hard OFF	hard OFF	No current	ZCS OFF

3.2.2 Existing Control Method

Frequency variation control, similar to traditional two-level LLC converters, can be applied in MMRs but offers a limited voltage regulation range. Alternatively, adjusting the resonant tank voltage through arm voltages, as shown in Fig. 3.4, allows for a wide range of discontinuous modulation index control by varying the number of inserted submodules per arm. These two approaches have been effectively integrated to fulfill the control objectives of the MMR [61, 105]. In the discontinuous modulation index control described in [61, 105], a total of $N_{\text{sub}} + K$ submodules are inserted in each leg at any given time. This approach is advantageous when the input DC voltage is variable, as it helps maintain the submodule voltages within a safe range. However, in the hydrogen application considered here, the input voltage remains relatively stable. Therefore, the method is slightly modified

to maintain exactly N_{sub} submodules inserted per leg at all times. This modified approach will be used for comparison with the proposed method in Subsection 3.4.2.

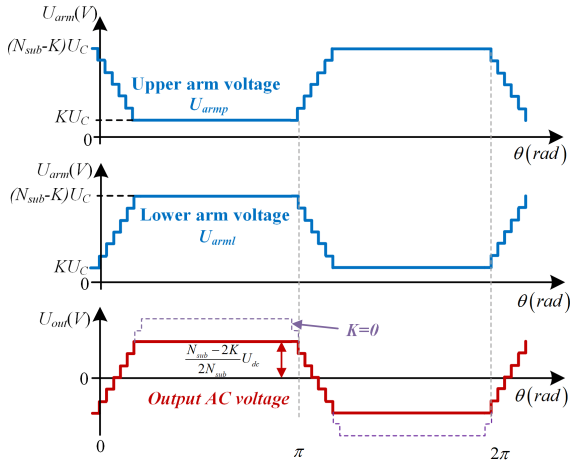


Figure 3.4: Discontinuous modulation index control. K represents the number of constantly inserted submodules for each arm. N_{sub} represents the number of submodules per arm in the MMC

While effective, frequency variation control relies on a small transformer magnetizing inductance, resulting in high magnetizing currents and increased losses in the MFT and MMC. Key limitations and features of this control strategy are summarized in Table 3.2 as Control Method 1.

Table 3.2: Comparison of the existing control methods with the proposed control method

Control Method	1.DMC & FC* [61, 105]	2.DMC & PSC [101]	3.Proposed CMC
Number of Control variables	2	2	1
Control Complexity	High	High	Low
Magnetizing current	High	Low	Low
Resonant current THD	Medium	Medium	Medium/Low**
Power losses	High	Medium	Medium/Low**

* DMC: discontinuous modulation index control; FC: frequency variation control; PSC: phase shift angle control; CMC: continuous modulation index control.
** The reduction in MMC THDi is attributed to the fixed and low modulation waveform edge angle α, and is also influenced by the quality factor of the resonant tank (see Experimental Verification). If the THDi is significantly lower than that of DMC&PSC, further power-loss reduction and efficiency improvement can be achieved.

Ref. [101] introduces phase shift control as an alternative to frequency variation control, as illustrated in Fig. 3.5. This approach involves increasing the phase shift angles at both the rising and falling edges of the modulation waveforms, thereby reducing the fundamental component magnitude and subsequently lowering the corresponding output voltage. Because of a fixed operating frequency, the magnetizing inductance can be designed to be significantly larger, thereby mitigating power losses associated with high magnetizing currents. Combined with discontinuous modulation index control, it achieves greater

efficiency than previous methods [61, 105]. A summary of this improved approach is provided in Table 3.2 as Control Method 2.

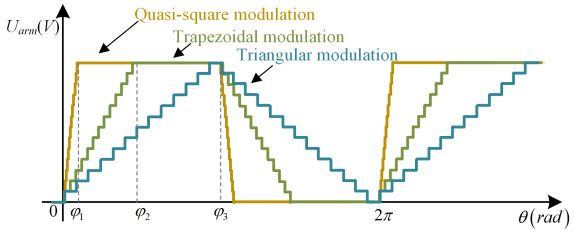


Figure 3.5: Phase shift control with different phase shift angles φ_1, φ_2, and φ_3.

However, the analysis in Subsection 3.4.3 will demonstrate that a fixed, small phase shift angle is preferable for reducing the THD_i of the output resonant current and, consequently, minimizing power loss.

A further question for the phase shift control combined with discontinuous modulation index control is whether it can adequately compensate for the discrete steps in the modulation index. These steps are introduced by the discontinuous control method itself in systems with a low number of submodules per arm, such as five, where the step size becomes significant. This aspect requires further analysis. To clarify the relationship between the discrete modulation index variations and the number of submodules per arm, as shown in Fig. 3.4, the parameter K denotes the number of submodules that are either constantly inserted or bypassed in each arm, while N_{sub} represents the total number of submodules per arm in the MMC.

Accordingly, the MMC AC output voltage magnitude U_{ac} can be expressed as

$$U_{ac} = \frac{N_{\mathrm{sub}} - 2K}{2N_{\mathrm{sub}}} U_{dc} \tag{3.6}$$

The corresponding voltage modulation index of the MMC is given by

$$M(N_{\mathrm{sub}}, k) = \frac{U_{ac}}{\frac{1}{2}U_{dc}} = \frac{N_{\mathrm{sub}} - 2K}{N_{\mathrm{sub}}} \tag{3.7}$$

Based on Equation (3.7), the modulation index for various values of N_{sub} is plotted in Fig. 3.6. As shown, when the number of submodules per arm is small—for example, four—the modulation index steps between adjacent values of K are large (up to 0.5). Such large gaps in modulation index introduce difficulties for the phase shift angle control, which must compensate for these discontinuities to achieve fine-grained control of the output voltage.

Regarding the modulation index under phase shift angle control, according to [101], assuming the peak value of the trapezoidal waveform is normalized to 1, the magnitude of its fundamental component can be calculated as follows:

$$U_{ac} = \frac{\pi}{4} \cdot \frac{\sin(\alpha/2)}{\alpha/2}, \quad \alpha \in [0, \pi] \tag{3.8}$$

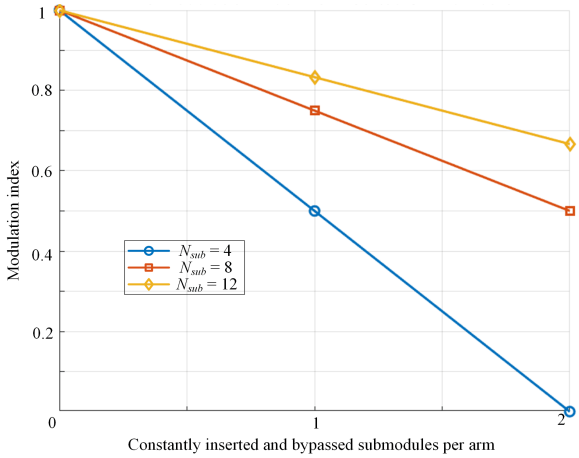


Figure 3.6: Modulation index of MMC versus control parameter K, with different number of submodules per arm

The resulting per-unit values of the fundamental component as a function of the phase shift angle are plotted in Fig. 3.7. The results indicate that the fundamental component decreases with increasing phase shift angle, ranging from 1 p.u. to a minimum of approximately 0.64 p.u. Here, the per-unit value is defined with respect to the fundamental component magnitude at zero phase shift angle, which serves as the reference (1 p.u.).

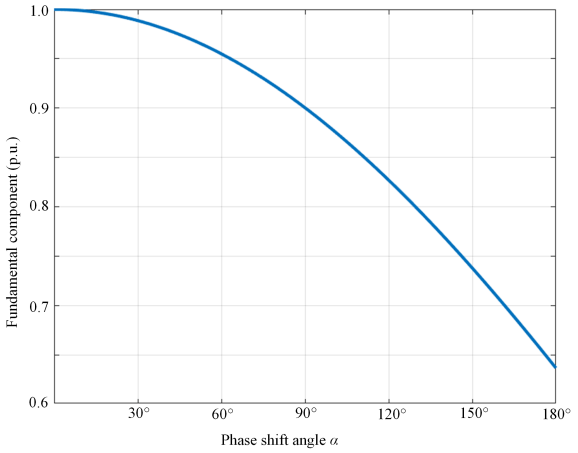


Figure 3.7: Fundamental component per-unit value as a function of the phase shift angle under phase shift control

At first glance, it may appear that phase shift angle control alone cannot adequately compensate for the modulation index gaps introduced by discontinuous modulation index control, particularly when the number of submodules per arm is small—for instance, four, as shown in Fig. 3.6.

However, after further analysis of configurations with a low number of submodules per arm, we found that the combination of phase shift angle control and discontinuous modu-

lation index control can still effectively span the full output voltage range. To demonstrate this, the fundamental component per-unit values were calculated using Fourier transform and are shown in Fig. 3.8 for systems with four and six submodules per arm. Additionally, Fig. 3.9 presents a simulation-based parameter sweep examining the achievable voltage gain under the combined control strategy.

Notably, Fig. 3.9 shows a close match with the results in Fig. 3.8. Both figures confirm that phase shift angle control can effectively bridge the modulation index gaps caused by discrete K-steps. Moreover, the effective modulation index range for the phase shift angle control achieved with four submodules per arm extends from 1 p.u. to approximately 0.48 p.u.—broader than the theoretical range of 1 to 0.64 derived from the ideal trapezoidal waveform in Fig. 3.7. This discrepancy arises because, at low submodule counts, the actual modulation waveform deviates significantly from the ideal trapezoidal shape; the rising and falling edges become discrete steps rather than continuous slopes.

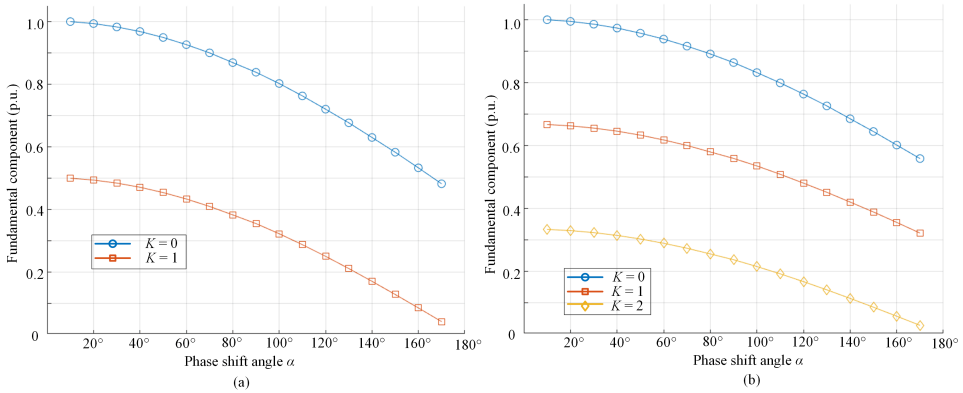


Figure 3.8: Fundamental component per-unit value versus phase shift angle: (a) $N_{\mathrm{SM}} = 4$ submodules per arm, (b) $N_{\mathrm{SM}} = 6$ submodules per arm

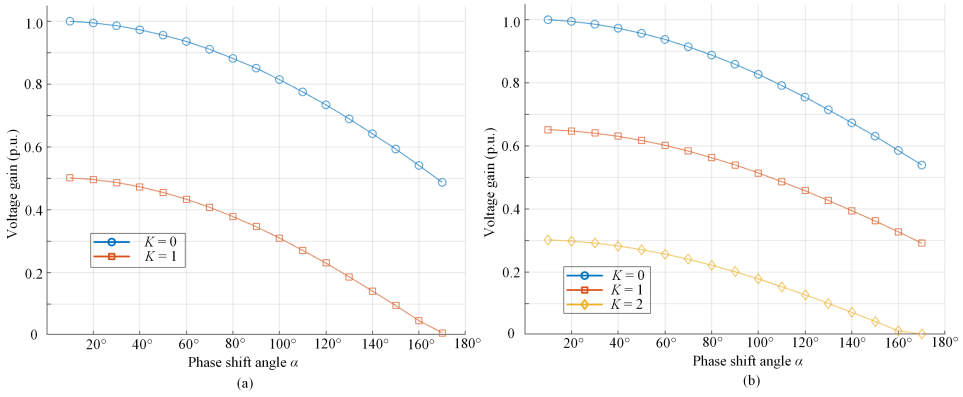


Figure 3.9: Simulated voltage gain versus phase shift angle: (a) $N_{\mathrm{SM}} = 4$ submodules per arm, (b) $N_{\mathrm{SM}} = 6$ submodules per arm

Based on the analysis and supporting simulations, it can be reasonably concluded that for systems with a low number of submodules per arm, such as five, although the discrete steps in the modulation index are significant, the resulting gaps can still be adequately compensated by phase shift control.

The complete control structure of the phase shift angle control and discontinuous modulation index control is shown in Fig. 3.1. This existing control method employs two control variables, namely the phase shift angle and the constantly inserted submodule number K. These two variables jointly determine the modulation waveform and are used to regulate the output current. The control strategy is derived from the output current characteristics of the MMR with respect to the phase shift angle and K.

As an illustrative example, Fig. 3.10 shows the simulated output DC current as a function of K and phase shift angle under the same system parameters as the experimental setup, except that the number of submodules per arm is increased to six for clarity.

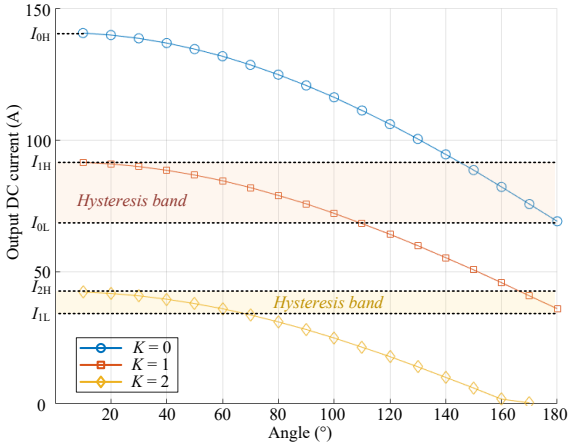


Figure 3.10: Simulated output current as a function of phase-shift angle using parameters consistent with the experimental platform, with the number of submodules per arm changed to six for clarity of presentation.

For $K = 0$, the output current decreases from $I_{0H} = 140\,\text{A}$ at a phase shift angle of 10° to $I_{0L} = 69.2\,\text{A}$ at 180°.

For $K = 1$, the output current varies from $I_{1H} = 91.6\,\text{A}$ at 10° to $I_{1L} = 36\,\text{A}$ at 180°.

For $K = 2$, the output current decreases from $I_{2H} = 42.4\,\text{A}$ at 10° to 0 A at approximately 170°.

The inserted submodule number K is determined by a lookup table based on the current reference. If the boundaries between different K regions are defined strictly at the current limits (e.g., I_{1H} and I_{2H}), small fluctuations of the current reference around these boundary values may lead to frequent switching of K and the corresponding phase shift angle.

For instance, if the current reference repeatedly varies between 92 A (slightly higher than I_{1H}) and 91 A (slightly lower than I_{1H}), the commanded value of K may alternate between $K = 0$ and $K = 1$. As a consequence, the corresponding phase shift angle command would also change abruptly from approximately 140° to 10°, even though the variation

in the current reference is minimal. Such abrupt and repetitive changes in the control commands could potentially deteriorate system stability, according to [61].

Therefore, following the approach in [61], a hysteresis-based lookup table is introduced to prevent frequent switching of the K command and the associated phase shift angle, thereby improving the stability of the overall control system.

With the hysteresis-based lookup table, when the current reference decreases from 100 A (above I_{1H}) to 80 A (between I_{0L} and I_{1L}), the value of K is intentionally kept at $K = 0$, and only the phase shift angle is adjusted by the PI controller. If the current reference further decreases to 60 A (below I_{0L}), the lookup table updates the command to $K = 1$, and the phase shift angle is then regulated within the corresponding operating range. Conversely, when the current reference increases and exceeds I_{1H}, the value of K is switched back to $K = 0$.

In this way, the hysteresis-based lookup table avoids frequent toggling of K and abrupt changes of phase shift angle near the boundary values while ensuring stable and continuous current regulation.

Once K is determined according to the hysteresis-based lookup table, the phase shift angle is regulated by a PI controller to track the current reference. Although the output current versus phase shift angle characteristics exhibit similar shapes for different K values, as shown in Fig. 3.10, both the current variation range and the slope differ. As a result, different PI parameter sets are required for different K values in order to achieve optimal dynamic performance. The complete control structure of the existing method is summarized in Fig. 3.1. The above analysis is also applicable to systems with different power ratings and different numbers of submodules per arm.

3.3 Proposed Control Method for MMR-SST

Existing control methods often combine discontinuous modulation index control with frequency variation or phase shift control, leading to multiple control loops, complicating FPGA implementation. This Section proposes a novel continuous modulation index control method, using a single control variable while maintaining equivalent controllability. A summary of the proposed control method is presented in Table 3.2 as Control Method 3.

3.3.1 Proposed Modulation Method

The modulation index control shown in Fig. 3.4 exhibits discontinuities inherent to the waveform's nature, characterized by a stair-step pattern that appears and disappears in distinct steps. These steps correspond to discrete control parameter K.

Conversely, Fig. 3.11 illustrates the double-step staircase waveform modulation, which facilitates continuous modulation index control. As the staircase waveform decreases its levels, both the uppermost and bottom levels continuously shrink until they eventually vanish. The modulation waveform for both the upper and lower arms exhibits a 180° phase shift. The term "double-step staircase waveform modulation" originates from the waveform's overall stair-step structure, featuring two distinct steps at the upper and lower levels. The presence of the lower step ensures symmetry in the modulation waveform, guaranteeing that at any given time, there are always N_{sub} submodules engaged in each leg, with N_{sub} denoting the number of submodules per arm in the MMC.

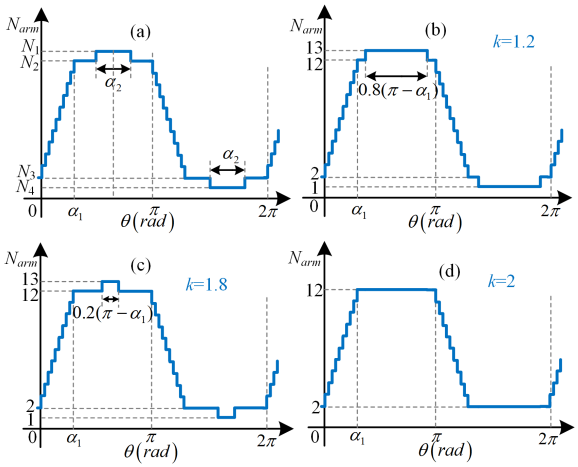


Figure 3.11: Continuous modulation index control with double-step staircase waveform modulation. N_{arm} represents the command value for the number of submodules to be inserted into the arm. The continuous change in parameter k illustrates the modulation index's continuity. (a) displays a general case, while (b), (c), and (d) show specific instances when k equals 1.2, 1.8, and 2, respectively

To quantify this continuous modulation index control, the shape factor k is used. When k is a natural number, it has a similar meaning to K in discontinuous modulation index control in Fig. 3.4. Between integer values, k takes on decimal values, representing the lengths of the uppermost and bottom steps.

Using k, the parameters shown in Fig. 3.11(a) are defined in (3.9), where $\text{rem}(k,1)$ represents the fractional part of the decimal number k. The floor function, denoted as $\text{floor}(k)$, returns the greatest integer less than or equal to k. The ceiling function, denoted as $\text{ceil}(k)$, returns the smallest integer greater than or equal to k. The uppermost level N_1 is centered with the next level N_2, and the bottom level N_4 is centered with the next level N_3.

$$\begin{cases} N_1 = N_{\text{sub}} - \text{floor}(k) \\ N_2 = N_{\text{sub}} - \text{ceil}(k) \\ N_3 = \text{ceil}(k) \\ N_4 = \text{floor}(k) \\ \alpha_2 = [1 - \text{rem}(k,1)] \cdot (\pi - \alpha_1) \end{cases} \tag{3.9}$$

Fig. 3.11(b)–(d) show examples with different k values when $N_{\text{sub}} = 14$. The phase shift angle of the rising edge and falling edge, α_1, is kept at a relatively low value of 10° in the following Sections.

Fig. 3.12 illustrates the modulation waveform transition from $k = 1$ to $k = 2$, highlighting the smooth and continuous nature of the change.

In theory, as k increases, the fundamental component of the modulation waveform decreases, leading to a corresponding reduction in the output voltage of the MMR. A k-value sweep was conducted to evaluate the effectiveness of continuous modulation index control, as depicted in Fig. 3.13. The theoretical modulation index for each k is determined by dividing the fundamental component value of the modulation waveform, calculated

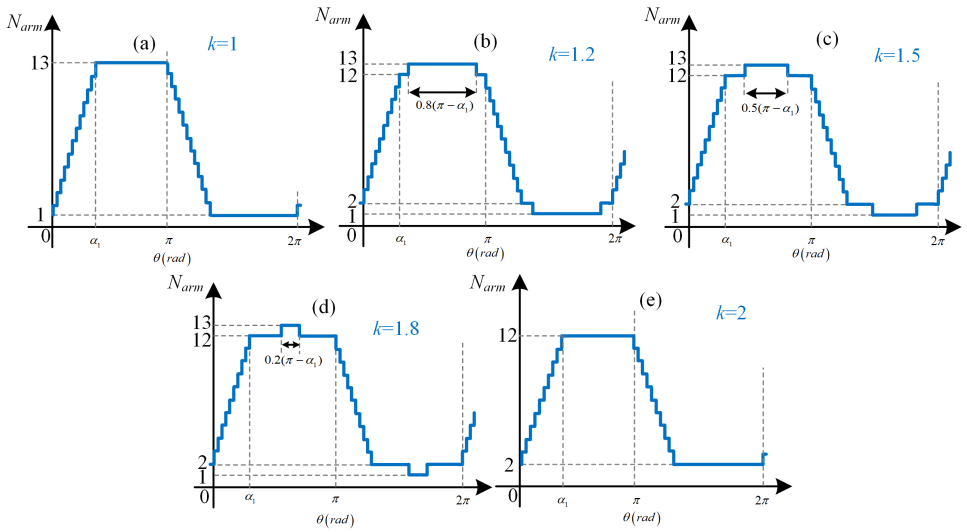


Figure 3.12: Proposed continuous modulation index control using a double-step staircase waveform, with shape factor k changing from 1 to 2

using the Fourier transform, by the fundamental component value when $k = 0$. Fig. 3.13 illustrates that by varying k alone, the output voltage and current of the MMR can be continuously controlled.

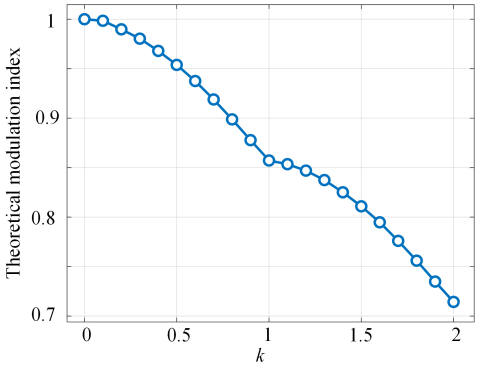


Figure 3.13: Theoretical modulation index with varying k when $N_{\text{sub}} = 14$

In contrast to frequency modulation in LLC converters, the proposed continuous modulation index control uses double-step staircase waveform modulation method to fix the operating frequency at the resonant frequency, allowing flexible resonant unit design and minimizing losses by using a larger magnetizing inductance for the MFT.

3.3.2 Gate Signal Generation and Overall Control Loop

The double-step staircase waveform modulation can be decomposed into different gate signals, each corresponding to a single submodule per arm, as depicted in Fig. 3.14.

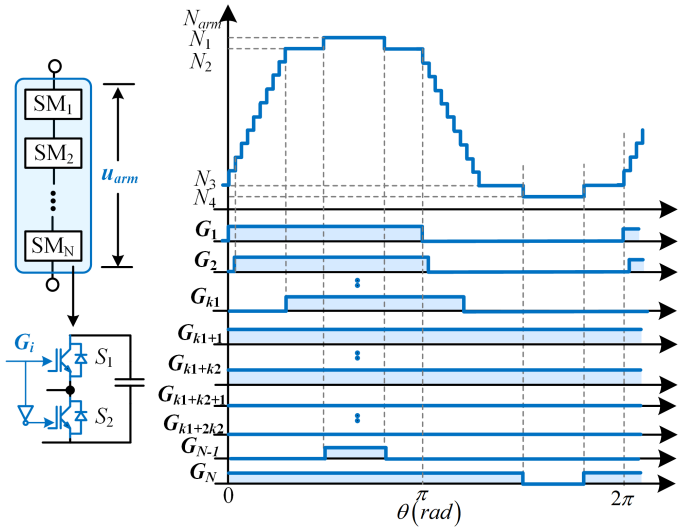


Figure 3.14: Gate signals generation for double-step staircase waveform modulation

There are five different statuses of submodules:

1. **Half-Inserted:** This status, represented by gate signals G_1 to G_{k_1}, indicates that the submodule duty cycle is 50% within one fundamental period. There are $k_1 = N_{\text{sub}} - 2 \cdot \text{ceil}(k)$ half-inserted gate signals. A small phase shift angle is introduced between these gate signals to reduce dv/dt.

2. **Full Inserted and Full Bypassed:** These statuses are represented by gate signals G_{k_1+1} to $G_{k_1+k_2}$ and $G_{k_1+k_2+1}$ to $G_{k_1+2k_2}$, respectively, where the submodule is continuously inserted or bypassed throughout the fundamental period. There are $k_2 = \text{floor}(k)$ gate signals for each of these statuses.

3. **Short-Inserted and Short Bypassed:** The fourth and fifth statuses, involving gate signals G_{N-1} and G_N, form the upper and lower steps of the modulation waveform respectively.

The overall process of continuous modulation index control is illustrated in Fig. 3.1. The shape factor k is adjusted based on the feedback of the output current. In this application, the currents from two electrolyzers are sampled, averaged to obtain the mean output current, and then compared with the target current value. The resulting error is processed by a proportional-integral (PI) controller. With k established, the corresponding gate signals are generated.

Before sending the gate signals into MMC, the submodule voltage balancing algorithm starts to function. This Chapter uses the submodule voltage balancing method in [61, 108], as shown in Fig. 3.15. The balancing algorithm is executed once every fundamental period.

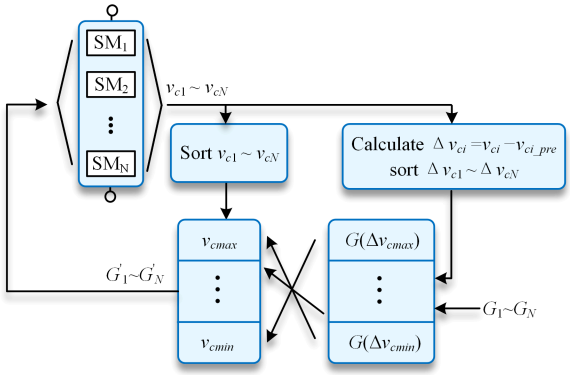


Figure 3.15: Submodule voltage balancing algorithm.

Taking the upper arm of phase A as an example, let $v_{c1} \sim v_{cN}$ denote the capacitor voltages of the N submodules (SMs). Once triggered, the algorithm first sorts the capacitor voltages $v_{c1} \sim v_{cN}$. Simultaneously, the voltage variation of each submodule is calculated as $\Delta v_{ci} = v_{ci} - v_{ci,\text{pre}}$, where $v_{ci,\text{pre}}$ is the voltage of the i-th SM one fundamental period earlier. The set of variations $\Delta v_{c1} \sim \Delta v_{cN}$ is then sorted.

A larger Δv_{ci} indicates a higher charging capability of the corresponding gate signal in the previous period. Therefore, this gate signal with high charging capability is reassigned to a submodule with a lower voltage to help it catch up with the others. Conversely, gate signals with lower charging capability are assigned to submodules with higher voltages, preventing them from overcharging. Through this process, dynamic voltage balancing is achieved.

To determine the PI controller parameters for the feedback current loop, the transfer function of the system must either be derived analytically or obtained through measurement. As reported in previous studies [109–117], the state-space averaging method is not applicable to frequency-controlled resonant converters because their power processing mechanism differs fundamentally from that of PWM converters. In PWM converters, the natural frequency of the output filter is much lower than the switching frequency, and modulation is realized through the low-frequency component of the control signal. Under this condition, the averaging method can approximate the nonlinear state equations with a linear continuous model, which remains accurate up to about half the switching frequency (i.e., the Nyquist frequency when sampled once per switching period). In contrast, in resonant converters the switching frequency is close to the resonant tank frequency, and the state variables are dominated by switching-frequency harmonics rather than low-frequency components. Modulation is achieved through the interaction between the switching and resonant frequencies. Since the averaging method filters out switching-frequency information, it fails to capture the dynamic behavior of resonant converters.

As a result, the extended describing function method has become a widely used framework for systematic small-signal modeling of nonlinear switching converters. Unlike conventional state-space averaging, this approach is able to include arbitrary Fourier components, thereby improving model accuracy. It produces continuous-time small-signal representations that are applicable not only to PWM converters but also to a wide range of

soft-switching resonant topologies. The main limitation of the extended describing function method is that constructing the model requires identifying every possible operating mode of the circuit. In the case of the LLC resonant converter, numerous operating modes exist, as discussed in [109]. For the MMR topology, the number of operating modes becomes even larger because of the complex and variable modulation waveforms used in the MMC.

Instead of the extended describing-function method, this dissertation adopts a simulation-based method, which emulates the function of an impedance analyzer to obtain the small-signal response directly from time-domain simulations. This technique requires no additional modeling effort, can naturally include parasitics, and is particularly effective for complex converter topologies that are challenging for conventional modelling methods. The overall approach is detailed analysed in [109].

To measure the frequency response of the plant, the current feedback loop is temporarily opened and the shape factor k is fixed at specified values. In this work, the plant refers to the transfer function from the shape factor k at the input of the gate-signal generator to the converter output current $i_{\text{electrolyzer}}$, including the effects of gate signal generator, submodule voltage balancing, the MMR power stage, and the electrolyzer load. The procedure is summarized as follows:

1. **Baseline simulation:**
   The converter is simulated at specific operating points, defined by fixed shape factor, load condition, and input voltage. The output current is recorded, and an FFT analysis is performed to extract the frequency components of interest. These results are stored for later use in Step 3. In this study, steady-state values of k, denoted as k_s, are chosen as 0.5, 1.5, 2.5, and 3.5. Other system parameters are provided in Table 3.3 for 120 kW case, and the simulations are repeated for each of the four k values.

2. **Perturbation injection:**
   A small-signal perturbation is superimposed on the steady-state shape factor k_s. Specifically, a sinusoidal signal is introduced as $x_m(t) = k_p \cos(2\pi f_p t)$, leading to the perturbed shape factor expressed as

$$k(t) = k_s + k_p \cos(2\pi f_p t) \tag{3.10}$$

   where k_p is the perturbation magnitude (set to 5% of k_s in this study to ensure linearity), and f_p is the perturbation frequency. The MMR output current responds to this excitation with both a DC component and a sinusoidal component at f_p. An FFT is applied to the recorded current waveform to extract the frequency component at f_p, which is then saved for the next step. In this part, the perturbation frequencies are selected as

$$\begin{aligned} f_p \in \{&10, 20, 30, 40, 50, 60, 70, 80, 90, 100, \\ &200, 300, 400, 500, 600, 700, 800, 900, 1000, \\ &2000, 3000, 4000, 5000\}\,\text{Hz} \end{aligned}$$

   For each steady-state value of k_s (0.5, 1.5, 2.5, and 3.5), the system is simulated across all perturbation frequencies, resulting in a total of $4 \times 23 = 92$ simulations.

3. **Frequency response extraction:**
The small-signal frequency response of the plant is obtained by comparing the perturbed and baseline currents. Specifically, the transfer function is calculated as

$$G(j\omega_p) = \frac{I_{\text{pert}}(j\omega_p) - I_{\text{base}}(j\omega_p)}{K_{\text{pert}}(j\omega_p)} \tag{3.11}$$

where $I_{\text{pert}}(j\omega_p)$ denotes the Fourier component of the output current under perturbed $k(t)$, $I_{\text{base}}(j\omega_p)$ is the Fourier component of the output current under baseline k_s, and $K_{\text{pert}}(j\omega_p)$ represents the Fourier component of the perturbation signal $k_p \cos(2\pi f_p t)$.

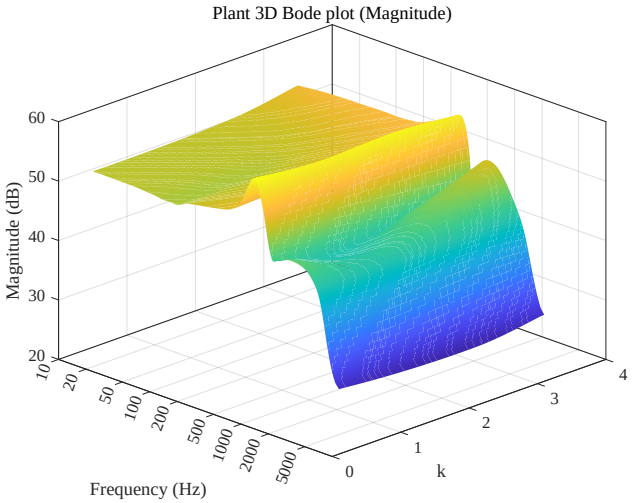


Figure 3.16: Plant Bode plot showing the magnitude response.

As a result, the plant transfer-function Bode plots obtained through perturbation simulations are shown in Fig.3.16 and Fig.3.17.

To better analyze the plant transfer function characteristics, Fig.3.16 and Fig.3.17 are redrawn in 2D views, as shown in Fig.3.18. At different k values corresponding to different system operating points, the magnitude and phase responses exhibit similar trends. Specifically, at low frequencies within several hundred Hz, the magnitude remains around 50 dB , while the phases stay close to -180°. Based on these observations, the subsequent Section examines the transfer function characteristics of the required PI controller to determine appropriate parameter settings.

With the proposed control method, a higher k value results in a reduced output current, since the controlled variable increases and inversely influences the plant output. Consequently, the proportional and integral gains of the PI controller must be set to negative values to ensure proper feedback regulation. An example Bode plot of the PI controller with negative parameters is shown in Fig. 3.19. This controller has a turning frequency of approximately 2000 Hz, with its magnitude decreasing at a slope of -20 dB/dec and the

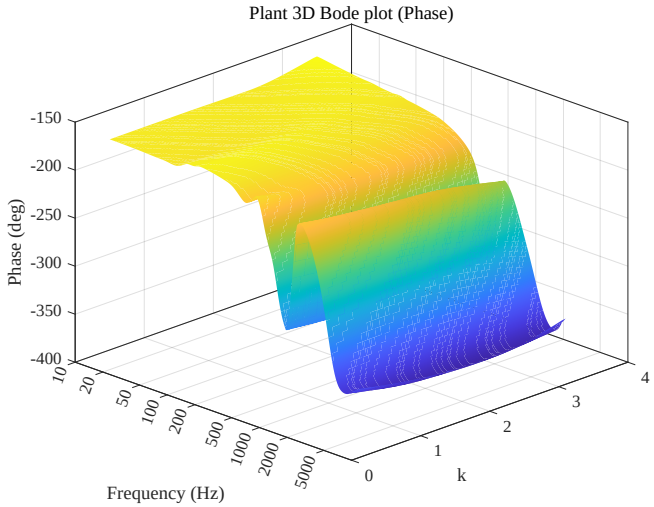


Figure 3.17: Plant Bode plot showing the phase response.

phase maintained at 90° within the low-frequency range of several hundred hertz. Under these characteristics, if the open-loop crossover frequency of the system is placed around 100 Hz, the corresponding open-loop phase will be approximately $-180^\circ + 90^\circ$, thereby yielding a phase margin of about 90°. In addition, the turning frequency should be chosen, as illustrated in Fig.3.19, to be higher than 1000 Hz, ensuring that the magnitude peak of the plant around 600 Hz in Fig.3.18 can be effectively damped. Here, the turning frequency refers to the frequency of the PI controller at which the control action transitions from integrator-dominated behavior at low frequencies to proportional-dominated behavior at higher frequencies, corresponding to a change in magnitude slope from −20 dB/dec to a constant gain.

According to the previous analysis, the PI controller is designed to satisfy the following requirements:

1. The turning frequency should be higher than 1000 Hz; in this study, it is selected as 2000 Hz.

2. The gain magnitude at 100 Hz should be approximately −52 dB, such that the system open-loop transfer function crossover frequency is located around 100 Hz.

Based on these design specifications, the parameters can be uniquely determined (with negative values to ensure the correct feedback direction). The design conditions are given as follows:

- Target frequency: $f_0 = 100\,\text{Hz} \Rightarrow \omega_0 = 2\pi \cdot 100\,\text{rad/s}$.
- Target gain: $-52\,\text{dB} \Rightarrow |G_c(j\omega_0)| = 10^{-52/20}$,
- Turning frequency: $f_z = 2000\,\text{Hz} \Rightarrow \omega_z = 2\pi \cdot 2000\,\text{rad/s} = \dfrac{K_i}{K_p}$.

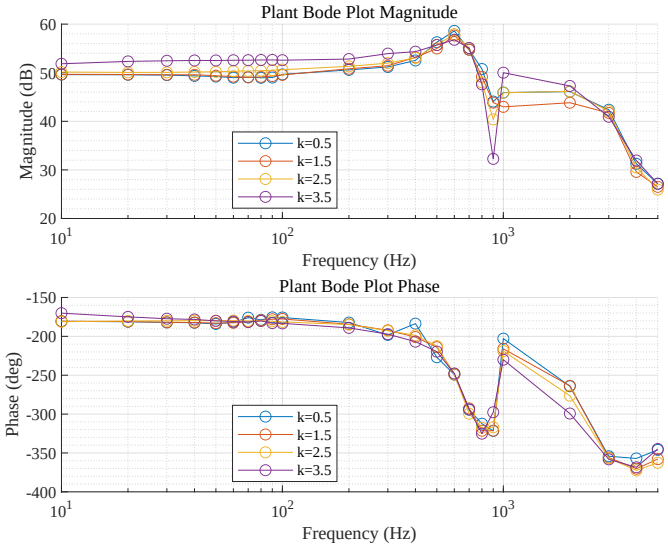


Figure 3.18: Plant Bode plot showing the magnitude and phase response.

Accordingly, the magnitude of the PI controller at ω_0 is expressed as

$$|G_c(j\omega_0)| = |K_p| \sqrt{1 + \left(\frac{\omega_z}{\omega_0}\right)^2}. \tag{3.12}$$

Thus, the proportional and integral gains are obtained as

$$|K_p| = \frac{10^{-52/20}}{\sqrt{1 + \left(\frac{\omega_z}{\omega_0}\right)^2}}, \qquad K_i = K_p \omega_z. \tag{3.13}$$

By substituting numerical values (and assigning negative signs to match the required feedback direction), the PI controller parameters are determined as

$$K_p \approx -1.2544 \times 10^{-4}, \qquad K_i \approx -1.5763. \tag{3.14}$$

Using the derived PI parameters, the system open-loop transfer function Bode plot is obtained, as shown in Fig. 3.20. It can be observed that the system exhibits a crossover frequency of approximately 100 Hz, a phase margin of about 90°, and that the original plant magnitude peak around 600 Hz is effectively damped. These characteristics indicate that the system is expected to operate with both stability and fast dynamic response. The simulation results using these controller parameters are presented in the following Section, specifically Fig. 3.22 and Fig. 3.23. For comparison, PI controllers designed for crossover frequencies of 50 Hz and 150 Hz were also tested; however, the configuration with a 100 Hz crossover frequency provided the best overall performance in terms of stability and transient speed.

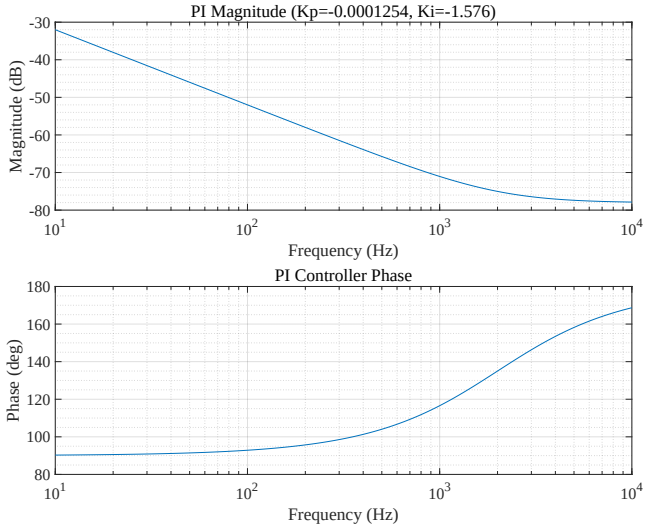


Figure 3.19: Bode plot of the PI controller

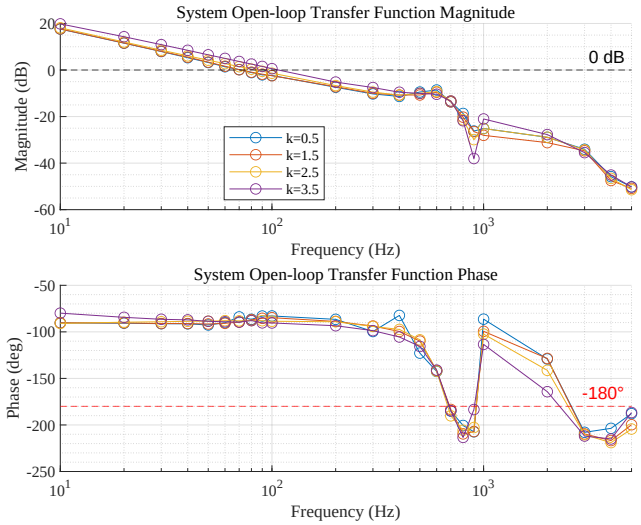


Figure 3.20: Bode plot of the system open loop transfer function

3.4 Simulation Results and Comparison with Previous Method

This Section evaluates the effectiveness of the proposed control strategy through time-domain simulations and provides a systematic comparison with the existing method. Key performance metrics, including efficiency and resonant current quality, are analyzed to enable a quantitative comparison between the two control approaches.

3.4.1 Simulation Results

To demonstrate the effectiveness of the proposed modulation and control strategy, an MMR-based SST incorporating a power loss model has been implemented within the Matlab/Simulink environment. The system design methodology and power loss modeling approach are based on [118], with the system parameters presented in the second column of Table 3.3. The input AC voltage V_{in} is 6.6 kV. The switching devices utilized in the input 50 Hz DRU, MMC, and MF DRU are ASENERGI D141-100, SKM50GB12T4, and ASENERGI D171-500, respectively. The input voltage is maintained at 6.6 kV, while the output current ranges from 0 A to the rated 750 A. The system is also designed with a 1.3 p.u. overcurrent capability, enabling it to handle currents up to 1000 A. The total rated output power is 240 kW, calculated as 120 kW per electrolyzer, with two electrolyzers in total. The electrolyzer load characteristics are defined by: $U_{\text{out}} = I_{\text{out}} \cdot 0.0875\,\Omega + 90\,\text{V}$.

To demonstrate the effectiveness of the proposed modulation and control strategy, an MMR-based SST incorporating a power loss model has been implemented within the Matlab/Simulink environment. The system design methodology and power loss modeling approach are based on [118], with the system parameters presented in the second column of Table 3.3.

Table 3.3: Key parameters of analysed systems

Parameter	Simulink Model	Experiment Setup
Electrolyzer rated current I_{out}	750 A	100 A
Electrolyzer rated power P_{out}	120 kW	3 kW
MMC arm SM number N_{sub}	14	4
SM capacitance C_{sm}	450 μF	5 mF
Arm inductance L_{arm}	2 mH	2.2 mH
Resonant capacitance C_r	6.7 μF	6.7 μF
MFT leakage inductance L_{lk}	5.3 mH	2.86 mH
MFT magnetizing inductance L_{m}	1 H	50 mH
MFT turn ratio n	50	8.5
Output capacitance C_o	8 mF	1.36 mF
Resonant frequency f_x	1000 Hz	1000 Hz

The input AC voltage V_{in} is 6.6 kV. The switching devices utilized in the input 50 Hz DRU, MMC, and MF DRU are ASENERGI D141-100, SKM50GB12T4, and ASENERGI D171-

500, respectively. The input voltage is maintained at 6.6 kV, while the output current ranges from 0 A to the rated 750 A. The system is also designed with a 1.3 p.u. overcurrent capability, enabling it to handle currents up to 1000 A. The total rated output power is 240 kW, calculated as 120 kW per electrolyzer, with two electrolyzers in total. The electrolyzer load characteristics are defined by: $U_{\text{out}} = I_{\text{out}} \cdot 0.0875\,\Omega + 90\,\text{V}$.

Fig. 3.21 illustrates the steady-state operation waveforms of the MMR-SST using the proposed control method.

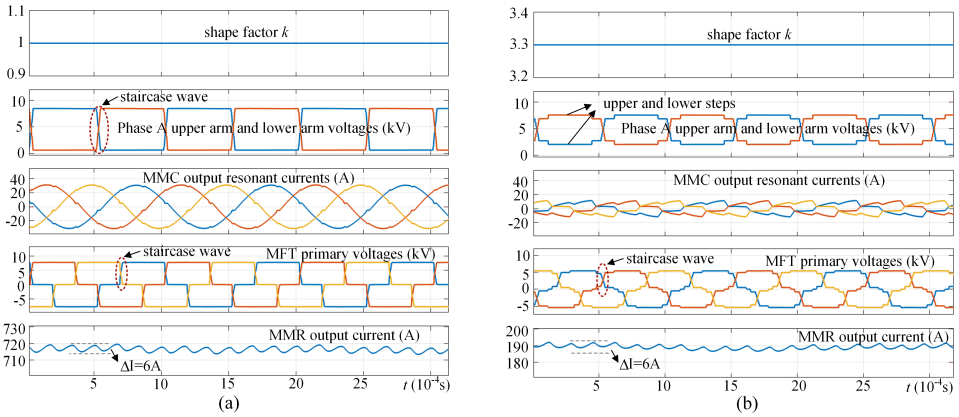


Figure 3.21: Steady-state waveform of MMR-SST with proposed continuous modulation index control: (a) shape factor $k = 1$ and $I_{\text{out}} = 718$ A, (b) shape factor $k = 3.3$ and $I_{\text{out}} = 190$ A

In Fig. 3.21(a), the arm voltages exhibit trapezoidal waveforms, and the MMC output currents are nearly sinusoidal with low THD_i, aligning with the operating principle of the resonant converter. The MMR output current shows minimal variation, meeting the requirements of the electrolyzer. In Fig. 3.21(b), when the output current setpoint decreases to 190 A, the shape factor k adjusts to 3.3. The arm voltages now include upper and lower steps, corresponding to the working principle presented in Fig. 3.21. Under this condition, the MMC resonant current is non-sinusoidal with high THD_i due to the discontinuous operation of the secondary-side DRU at low operating points, where discontinuities occupy a significant portion of the cycle.

Fig. 3.22 demonstrates the dynamic characteristics of the proposed control method. In Fig. 3.22(a), the output current decreases continuously from 980 A to 0 A as the shape factor k increases from 0.5 to 4.5 over time. The relationship between the MMR output current and k aligns with the theoretical analysis presented in Fig. 3.13. As the MMR output current decreases, the MMC input DC voltage increases, causing the submodule voltages to rise accordingly to accommodate the higher input DC voltage. A similar effect causes the average value of the MMC arm voltages to gradually rise.

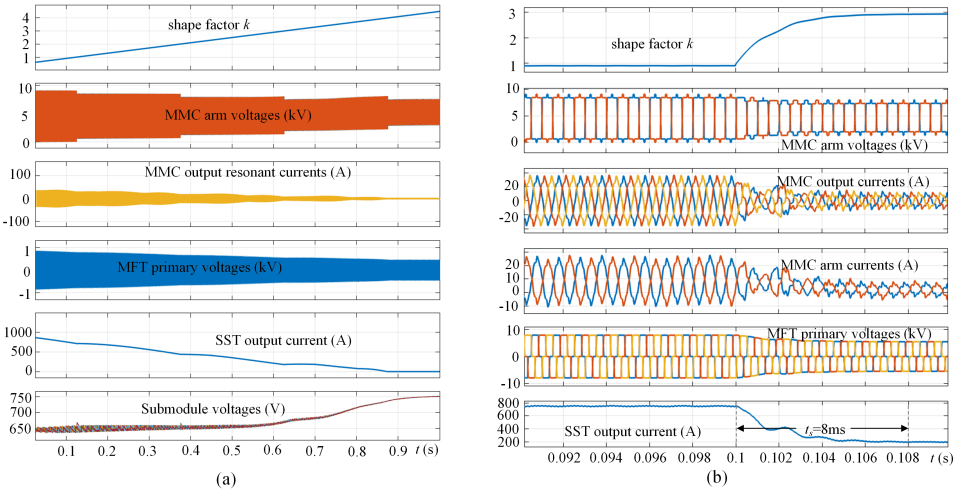


Figure 3.22: Dynamic waveform of MMR-SST with proposed continuous modulation index control: (a) gradual change in output current from 980 A to 0 A by continuously varying the shape factor k, (b) output current step response from 750 A to 200 A, demonstrating stable dynamic performance with no overshoot and a settling time of approximately 8 ms (±5% band)

Fig. 3.22(b) illustrates the dynamic response of the current controller when the output current setpoint is adjusted from 750 A to 200 A. The arm currents exhibit slight oscillations with minor amplitude fluctuations, attributed to the 12-pulse characteristics of the 50 Hz input DRU. After a settling time of 8 ms, the output current stabilizes within the ±5% tolerance band without any overshoot, confirming the controller's fast and stable behavior under step changes in load conditions.

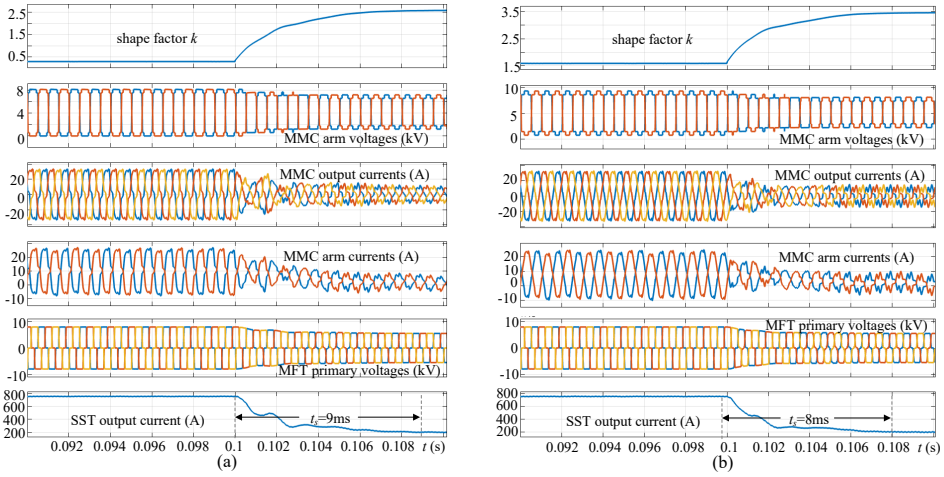


Figure 3.23: Current control waveforms showing step response with output DC current command changing from 750 A to 200 A: (a) input AC voltage of 0.9 p.u., (b) input AC voltage of 1.1 p.u.

In order to analyze how the adjustment of the shape factor k impacts system perfor-

mance under extreme operating conditions—and whether such adjustment could potentially lead to instability—±10% variations in the input AC grid voltage have been considered, as shown in Fig. 3.23. The current controller's response is evaluated by applying a step change in the output current command from 750 A to 200 A. In all three cases, the controller maintains stable operation with settling times within 10 ms. Furthermore, extensive simulations and experimental validation have shown no signs of instability, provided that the controller parameters are properly tuned. These results confirm that the adjustment of the shape factor k does not compromise system stability under both typical and extreme conditions.

3.4.2 Comparison with Phase-Shift Control Plus Discontinuous Modulation Index Control

To verify the advantages of the proposed continuous modulation index control, this Section compares it with the existing phase shift control combined with the discontinuous modulation index control, as discussed in Section 3.2.2. The discontinuous modulation index control has been slightly adjusted for the fixed input voltage, with K now representing the number of submodules that are either constantly inserted or bypassed in each arm, ensuring a total of N_{sub} submodules are inserted in each leg at any time.

A parameter sweep was conducted for both methods. For the continuous modulation index control, the shape factor k varied from 0 to 4, with intervals of 0.1. For the existing method, the control parameter K was varied from 0 to 3, with intervals of 1, and for each interval, the phase shift angle was adjusted from 10° to 120° in 10° increments. The sweep results for system efficiency, total power loss, and resonant current THD_i are presented in Fig. 3.24. The calculation of system efficiency primarily considers the power losses from the MMC, medium-frequency DRU, and MFTs, as these constitute the majority of the total losses. Losses from other components were deemed negligible and thus not included.

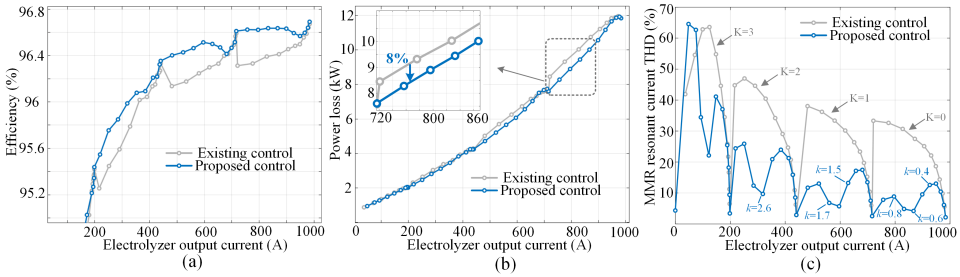


Figure 3.24: Comparison of two control methods: (a) efficiency comparison. The proposed control represents the continuous modulation index control, and the existing control represents the phase shift control combined with the discontinuous modulation index control; (b) power losses comparison, including the losses in the 50 Hz DRU, MMC, medium-frequency DRU, and MFTs; (c) MMR resonant current THD comparison

As shown in Fig. 3.24(a), the efficiency of both control methods exceeds 95% across most of the operating range, with the proposed control method consistently achieving higher or equal overall efficiency compared to the existing method. When the shape factor k is equal to or only slightly greater than the control parameter K (e.g., $k = 2.1$ and $K = 2$), and the phase shift control angle is small, the efficiencies of the two methods are comparable.

However, as the difference between k and K increases, the efficiency gap widens until k reaches the next integer value of K. This trend is influenced by the difference in resonant current THD_i, as illustrated in Fig. 3.24(c). As the THD_i difference increases, the associated power losses—specifically the MMC conduction loss, medium-frequency DRU conduction loss, and MFT winding loss—also increase, contributing to the growing efficiency difference.

As illustrated in Fig. 3.24(b), there is a noticeable difference in power losses between the two methods, particularly around the system's rated current of 750 A. The zoomed-in view highlights that near this rating point, the proposed control method reduces total power loss by 8%. As previously discussed, this reduction in power loss is primarily due to the difference in resonant current THD_i.

Fig. 3.24(c) compares the resonant current THD_i of the proposed and existing control methods across a wide output current range. At higher current levels, the existing method—based on phase-shift and discontinuous modulation index control—shows increasing THD_i within each fixed index segment (e.g., $K = 0, 1, 2$) as the phase shift angle α rises. Once the output current reaches the threshold of the next segment, the phase shift angle resets (i.e., to 10°), causing a sharp drop in THD_i. For instance, the THD_i can reach 35% at $K = 0$ and $\alpha = 110^\circ$, but drops to around 5% when transitioning to $K = 1$ and $\alpha = 10^\circ$.

In contrast, the proposed method maintains low THD_i across the full current range by fixing the phase shift angle at 10°. The proposed method at $k = 0$ is equivalent to the existing method at $K = 0$ with a phase shift angle of 10°, resulting in the same THD_i. However, as k increases while the angle remains fixed, the proposed method maintains lower THD_i compared to the existing method, until k and K both reach the next integer value (e.g., 1). This pattern repeats across successive intervals. For example, at $k = 0.6$, the THD_i remains significantly lower than that of the existing method at the same output current.

At lower currents (below 200 A), the difference in THD_i becomes negligible, due to the dominant effect of the secondary-side DRU's discontinuous operation. Further analysis of phase shift angle influence will be provided in Section 3.4.3.

Fig. 3.25 presents a breakdown of power losses at the rated current. Noticeable differences are observed in MMC conduction losses, medium-frequency DRU losses, and MFT winding losses, primarily due to the difference in current THD_i, which leads to higher RMS currents through the switches and transformer windings. The detailed loss calculation method can be found in [118]. The total losses for the phase shift control combined with discontinuous modulation index control amount to 8907 W, while the proposed control method results in total losses of 8177 W. This represents an 8.2% reduction in power loss with the proposed method, which could lead to substantial benefits in reducing the size and cost of the heatsink and chiller [118]. The efficiency of the proposed method reaches 96.62%, compared to 96.32% for the existing method.

A comparison of submodule capacitor voltage ripple is carried out at the rated output current condition to complement the evaluation of the proposed control method. One possible drawback of the proposed method is a slightly higher submodule capacitor voltage ripple. To illustrate this, Fig. 3.26 to Fig. 3.28 have been added, presenting the submodule capacitor voltage ripple under various operating conditions for both the proposed and existing control methods in the simulation cases.

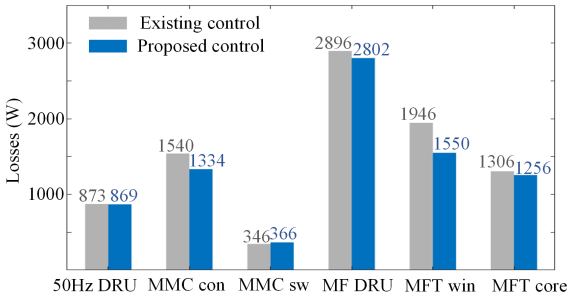


Figure 3.25: Loss calculation of MMC-SST at the rated current with two different control methods. 50 Hz DRU, MMC_con, MMC_sw, MF DRU, MFT_win, and MFT_core represent the input 50 Hz DRU losses, MMC conduction losses, MMC switching losses, medium-frequency DRU losses, MFT winding losses, and MFT core losses, respectively

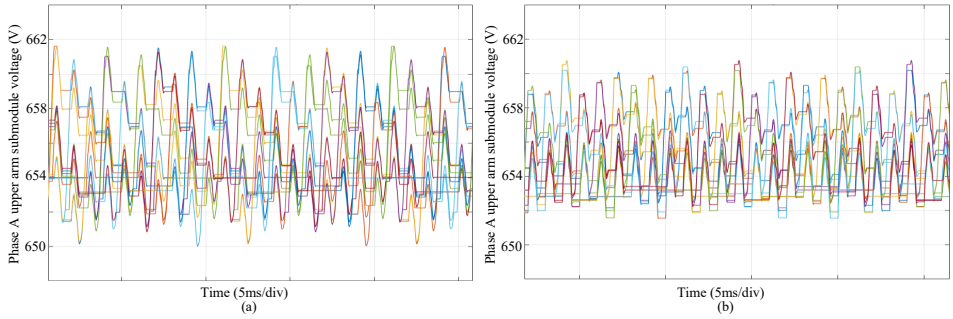


Figure 3.26: Submodule capacitor voltage comparison at an output DC current of 346 A. (a) Proposed continuous modulation index control, with shape factor $k = 2.5$ and phase shift angle $\alpha = 10^{\circ}$; the submodule voltage variation is 12 V. (b) Existing phase-shift control combined with discontinuous modulation index control, with control parameter $K = 2$ and phase shift angle $\alpha = 83^{\circ}$; the submodule voltage variation is 9 V.

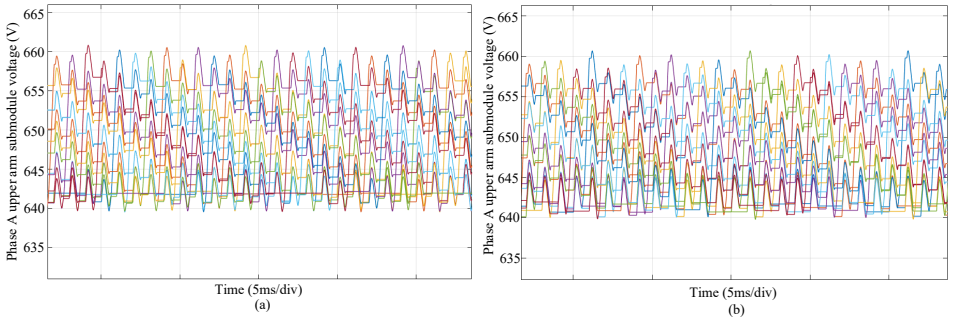


Figure 3.27: Submodule capacitor voltage comparison at an output DC current of 690 A. (a) Proposed continuous modulation index control, with shape factor $k = 1.2$ and phase shift angle $\alpha = 10^{\circ}$; the submodule voltage variation is 21 V. (b) Existing phase-shift control combined with discontinuous modulation index control, with control parameter $K = 1$ and phase shift angle $\alpha = 40^{\circ}$; the submodule voltage variation is 21 V.

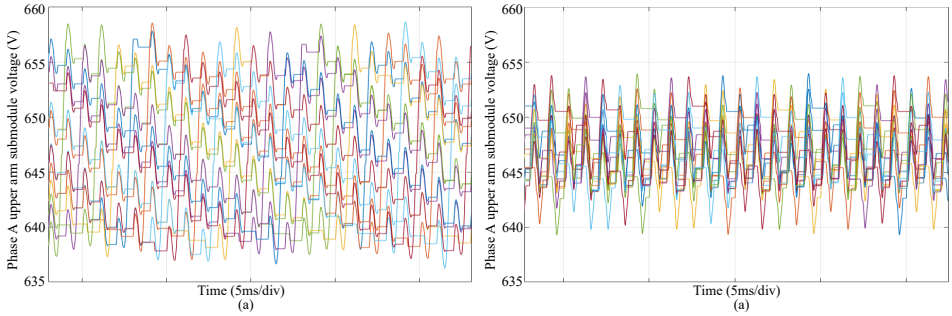


Figure 3.28: Submodule capacitor voltage comparison at the rated output DC current of 750 A. (a) Proposed continuous modulation index control, with shape factor $k = 0.9$ and phase shift angle $\alpha = 10^{\circ}$; the submodule voltage variation is 22 V. (b) Existing phase-shift control combined with discontinuous modulation index control, with control parameter $K = 0$ and phase shift angle $\alpha = 103^{\circ}$; the submodule voltage variation is 15 V.

As shown in the figures, the proposed control method exhibits slightly higher voltage ripple compared to the existing phase-shift method. Specifically:

- At 346 A output current (Fig. 3.26), the voltage variation is 12 V for the proposed method and 9 V for the existing method.
- At 690 A (Fig. 3.27), the variations are 21 V (proposed) and 21 V (existing).
- At the rated 750 A (Fig. 3.28), the variations are 22 V and 15 V, respectively.

This increase in ripple is primarily caused by differences in gate signal generation between the two control strategies. In the proposed method, several gate signals have duty ratios deviating from 50%, resulting in submodules being charged for durations shorter or longer than half a switching period. This asymmetry in charging time leads to slightly higher capacitor voltage ripple.

Nevertheless, in all tested cases, the peak-to-peak voltage ripple remains less than 5% of the average submodule voltage, which is well within typical design limits. In practical MMC applications, a ripple ratio of 10–20% is generally acceptable. Therefore, the proposed method meets the reliability and design requirements from an engineering perspective.

Regarding system power quality, a quantitative comparison of the input current THD between the two methods is provided in Fig. 3.29 and Fig. 3.30. As observed, the input current THD (THDi) for the proposed and existing methods are 13.28% and 13.18%, respectively. The difference is minimal, which aligns with the theoretical expectation. This is because the dominant factor influencing the input current THD is the diode rectifier configuration. In the proposed topology, a 12-pulse rectifier is employed, resulting in an expected THDi of approximately 15%.

3.4.3 MMR Resonant Current THD Analysis of Two Control Methods

To analyze the difference in THD_i of the MMR resonant current between the proposed control method and the existing control method as depicted in Fig. 3.24(c), a test case is presented in Fig. 3.31. This test case presents the steady-state waveforms of both control

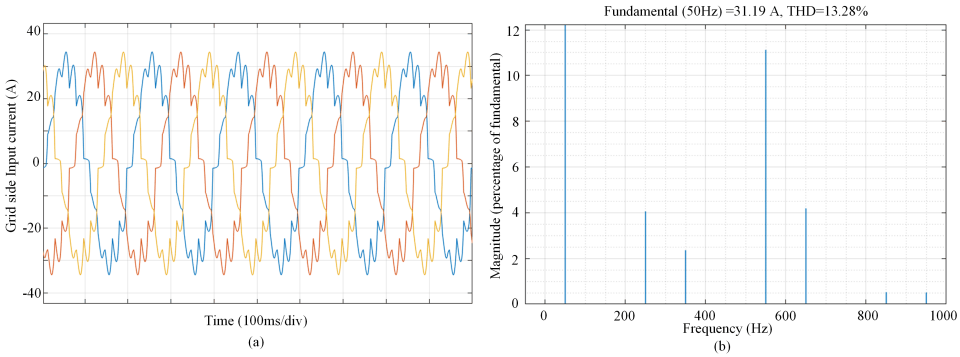


Figure 3.29: Grid-side input current at rated power using the proposed continuous modulation index control ($k = 0.9$, $\alpha = 10^{\circ}$): (a) input current waveform, (b) corresponding FFT spectrum

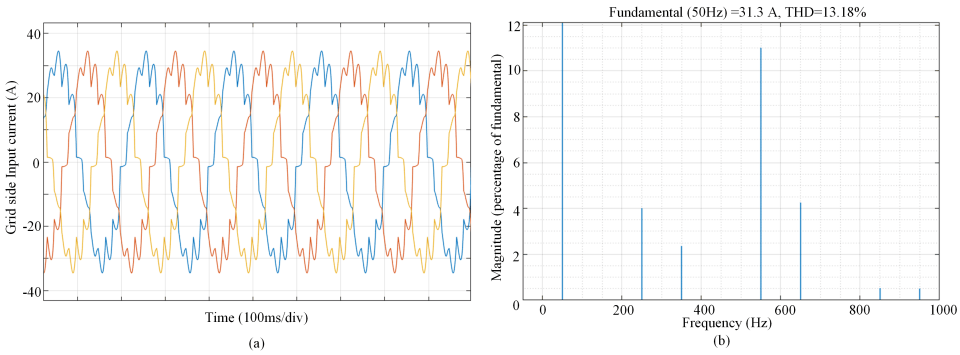


Figure 3.30: Grid-side input current at rated power using the existing phase-shift control combined with discontinuous modulation index control ($K = 0$, $\alpha = 103^{\circ}$): (a) input current waveform, (b) corresponding FFT spectrum

methods under the same output current condition of 865 A, as shown in Fig. 3.31(a) and Fig. 3.31(b). For the proposed control method with shape factor $k = 0.6$ and a 10° phase shift angle (Fig. 3.31(b)), the resonant current THD_i is 4.3%, compared to 27.9% for the existing method with control parameter $K = 0$ and an 80° phase shift angle (Fig. 3.31(a)).

To further isolate the influence of the phase shift angle on THD_i, Fig. 3.31(c) presents an additional case where the proposed control method is applied with the same shape factor ($k = 0.6$) as in Fig. 3.31(b), but with the phase shift angle increased to 80°, matching that of the existing control method in Fig. 3.31(a). In this case, the output current is 700 A, and the measured THD_i rises to 25.29%. This clearly indicates that the increase in THD_i is primarily caused by the larger phase shift angle. A detailed explanation of how the phase shift angle affects the switching behavior and harmonic distortion of the topology is provided below.

Given that the magnetizing inductance of the MFTs is significantly larger than the leakage inductance, the current through the magnetizing inductance is negligible. Additionally, since both the primary and secondary windings of the MFT are configured in a delta connection, the primary input current of the MFT (which is half of the MMR

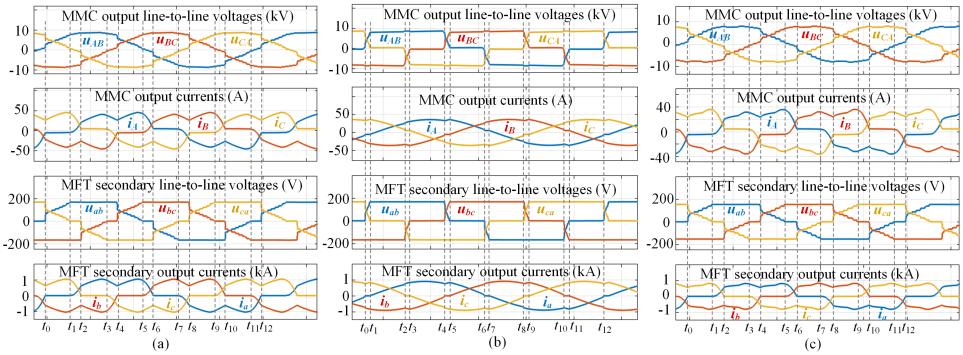


Figure 3.31: Steady-state waveform of MMR-SST with two control methods: (a) existing phase shift control combined with discontinuous modulation index control, with control parameter $K = 0$ and phase shift angle $\alpha = 80°$; (b) proposed continuous modulation index control, with shape factor $k = 0.6$ and phase shift angle $\alpha = 10°$; (c) proposed continuous modulation index control, with shape factor $k = 0.6$ and phase shift angle $\alpha = 80°$

resonant current) closely resembles the shape of the secondary output current, as shown in Fig. 3.31. Consequently, the MMC output resonant current and the MFT secondary output current exhibit identical THD_i values. To simplify the analysis, the focus will be on the MFT secondary voltages and output currents.

In Fig. 3.31, the interval from t_0 to t_{12} represents a complete period of the voltage and current waveforms, which can be divided into 12 distinct sections. The conduction states for the first 6 sections are illustrated in Fig. 3.32. Since the second half of the cycle is horizontally symmetric to the first half and follows the same pattern, it is not repeated in the analysis.

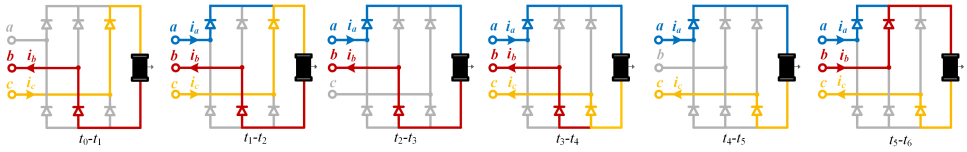


Figure 3.32: Switching states and current flow directions at different time intervals of the secondary-side DRU

From t_0 to t_1, the magnitude of u_{cb} is higher than that of u_{ab} and u_{ca}, resulting in current flow from port c to port b. Between t_1 and t_2, u_{ab} and u_{cb} have equal magnitudes, causing current to flow from both ports a and c to port b. From t_2 to t_3, u_{ab} reaches the highest magnitude, leading to current flow from port a to port b. During the interval from t_3 to t_4, u_{ab} and u_{ac} have equal magnitudes, causing current to flow from port a to both ports b and c. From t_4 to t_5, with u_{ac} having the highest magnitude, current flows from port a to port c. Finally, from t_5 to t_6, u_{bc} and u_{ac} have equal magnitudes, resulting in current flow from both ports a and b to port c.

The intervals t_0 to t_1, t_2 to t_3, and t_4 to t_5 correspond to the rising and falling edges of the MFT secondary line-to-line voltages. During these intervals, one of the secondary output currents of the MFT remains at zero, which distorts the overall sinusoidal shape of the current. The duration of these zero currents is directly related to the phase shift

angles used in both the proposed and existing methods. A larger phase shift angle results in longer durations of these zero currents.

In the existing phase shift control method, when the control delay angle is large—as seen in the case presented in Fig. 3.31(a)—typical dual-peak current waveforms occur, similar to those observed in three-phase DRU systems with sinusoidal input voltages. In contrast, the proposed control method employs a small delay angle shown in Fig. 3.31(b), minimizing the duration of discontinuous currents. This results in more sinusoidal current waveforms and lower current THD_i.

It should be noted that the effectiveness of THD_i reduction also depends on the resonant circuit design, particularly the quality factor Q_e as defined in (3.5). In the presented simulation, $Q_e = 0.078$. If a higher Q_e is used, the resonant tank will exhibit a narrower bandwidth, which inherently suppresses current harmonics. In such cases, the improvement in THD_i achieved by the proposed method becomes less pronounced. Experimental results and comparisons for different Q_e values will be provided in the next Section.

3.5 Experimental Verification

To validate the proposed control methods, a laboratory prototype of a modular multilevel resonant converter-based solid-state transformer was developed, with a 300 V input and a 100 A/3 kW output, as shown in Fig. 3.33.

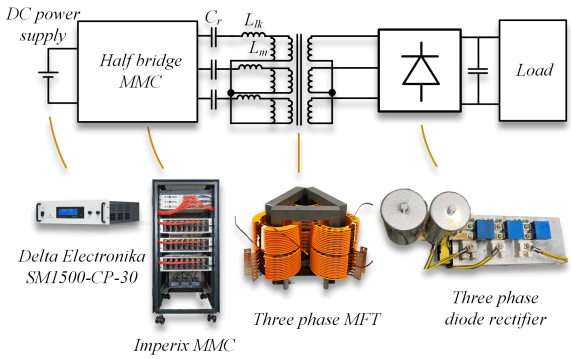


Figure 3.33: Experimental setup

The key parameters are listed in the third column of Table 3.3. The experimental setup, illustrated in Fig. 3.33, is a simplified version of the simulation configuration. The 12-pulse DRU rectifier has been replaced by a Delta Elektronika SM1500-CP-30 DC power supply, as the primary focus of this research is the control optimization of the modular multilevel resonant converter. The half-bridge MMC used in the experiment is based on the Imperix MMC platform, configured with four submodules per arm. A symmetrical three-phase transformer has been built [119], which provides closely matched leakage and magnetizing inductances among the three phases, in contrast to a conventional five-limb shell-type transformer with inherent asymmetry. The current feedback control, gate signal generation, and submodule voltage balancing are implemented on the Imperix B-Box controller, operating at an interrupt frequency of 100 kHz. The interrupt frequency refers

to the execution rate of the control loop on the Imperix B-Box controller, at which the control algorithms are executed and the gate signals are updated once per interrupt.

The PI controller parameters for the current control are designed following the same procedure as in the simulation case presented in Subsection 3.3.2. Based on this approach, the measured plant responses are obtained, as shown in Fig.3.34 and Fig.3.35. These Bode plots are not presented to perform a direct one-to-one comparison between the full-scale simulation model and the scaled-down experimental setup.

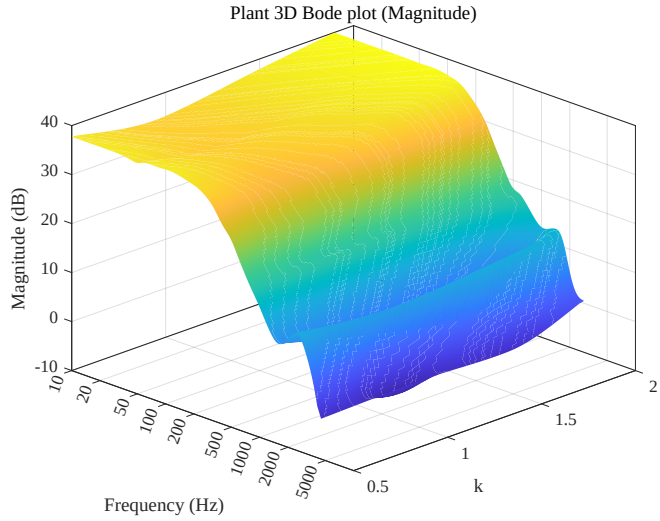


Figure 3.34: Plant magnitude response for the downscaled experimental setup.

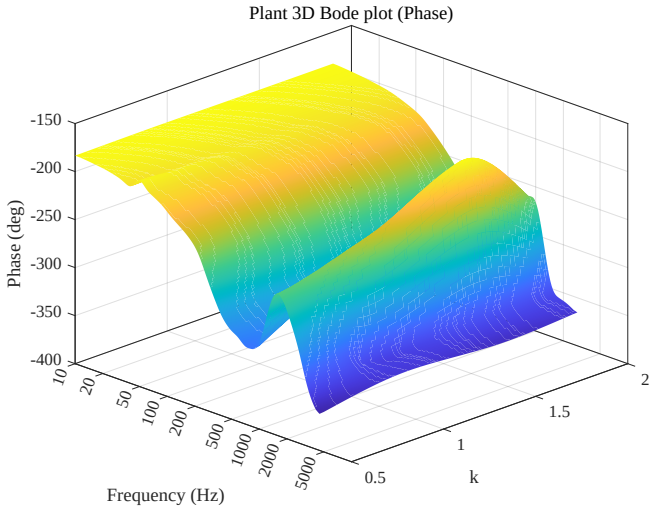


Figure 3.35: Plant phase response for the downscaled experimental setup.

Their purpose is to illustrate the frequency-domain characteristics of each plant individually, in order to support PI controller design. To achieve a crossover frequency of approximately 100 Hz, the calculated PI parameters are $K_p = -5.0 \times 10^{-4}$ and $K_i = -6.28$. The resulting system open-loop transfer function Bode plot is shown in Fig.3.36, indicating a phase margin of about 80°.

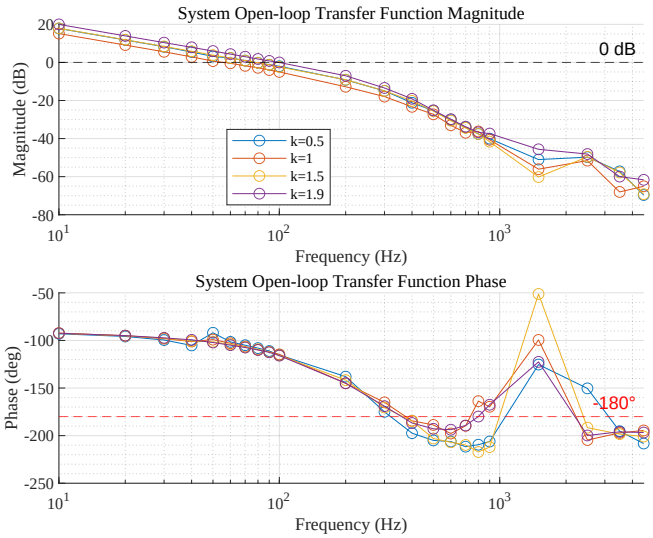


Figure 3.36: System open loop Bode plot for the downscaled experimental setup.

One key challenge in the practical implementation was improving the computational efficiency of the control algorithm on the Imperix B-Box controller, in order to achieve a higher CPU interrupt frequency within the available processing resources. This allowed the control algorithm to execute more frequently, enabling more precise and responsive system behavior. A detailed explanation is provided below.

As shown in Fig. 3.37, the modulation waveform can be decomposed into the corresponding gate signals 1–4. The CPU interrupt frequency of the Imperix controller affects the timing accuracy of the generated gate signals—specifically, whether the transitions between 0 and 1 occur at the intended moments. Taking gate signal 3 as an example, the blue line represents the ideal gate signal.

With a lower interrupt frequency (e.g., 10 kHz, shown in orange), the actual transition from 0 to 1 may be delayed. In contrast, a higher interrupt frequency (e.g., 50 kHz, shown in purple) enables the gate signal to more closely match the ideal switching timing.

Since the controller's CPU resources are limited, achieving a higher interrupt frequency required optimization of the control algorithm. The control program deployed on the CPU is currently generated from Simulink using Simulink Coder. Several methods were applied to reduce the computational load:

1. The data types used throughout the control algorithm were changed from double to single precision, significantly reducing memory usage and arithmetic complexity.

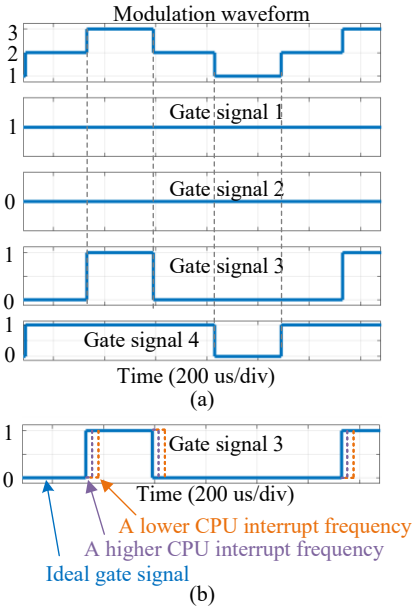


Figure 3.37: Illustration of the modulation waveform and gate signals for the experimental setup with four submodules per arm and shape factor $k = 1.5$: (a) modulation waveform and corresponding gate signals 1–4, (b) gate signal 3 showing the effect of different CPU interrupt frequencies

2. Originally, gate signal generation and submodule voltage balancing were implemented using MATLAB Function blocks. These were later replaced by S-Function blocks written in C++, which reduced code overhead and improved execution efficiency, resulting in faster real-time performance.

Through these optimizations, the interrupt frequency was successfully increased from 20 kHz to 100 kHz. The following experimental results will demonstrate stable and accurate system performance under this setting.

Additionally, for applications requiring even higher interrupt frequencies, part of the control algorithm can be offloaded to the controller's FPGA using Vitis HLS and Vivado. This significantly reduces the computational burden on the CPU. As a proof of concept, the submodule voltage balancing algorithm for the upper arm of phase A has been implemented on the FPGA. In future work, full FPGA-based control implementation will be considered, which could enable interrupt frequencies in the range of 200–300 kHz.

Figure 3.38 shows the Vivado block design used for this proof-of-concept implementation. The modules "average_0" and "sort_list_0" were custom-designed using Vitis HLS in a C++-based environment. The former performs the averaging of the submodule voltages, while the latter ranks the voltages to determine the insertion sequence for balancing. In contrast, the modules "axis_broadcaster_0" and "axis_dwidth_converter_0" are IP cores provided by Imperix, used for AXI4-Stream data broadcasting and format conversion, respectively, to interface with other logic blocks. This design demonstrates the feasibility of mapping voltage balancing logic onto FPGA fabric.

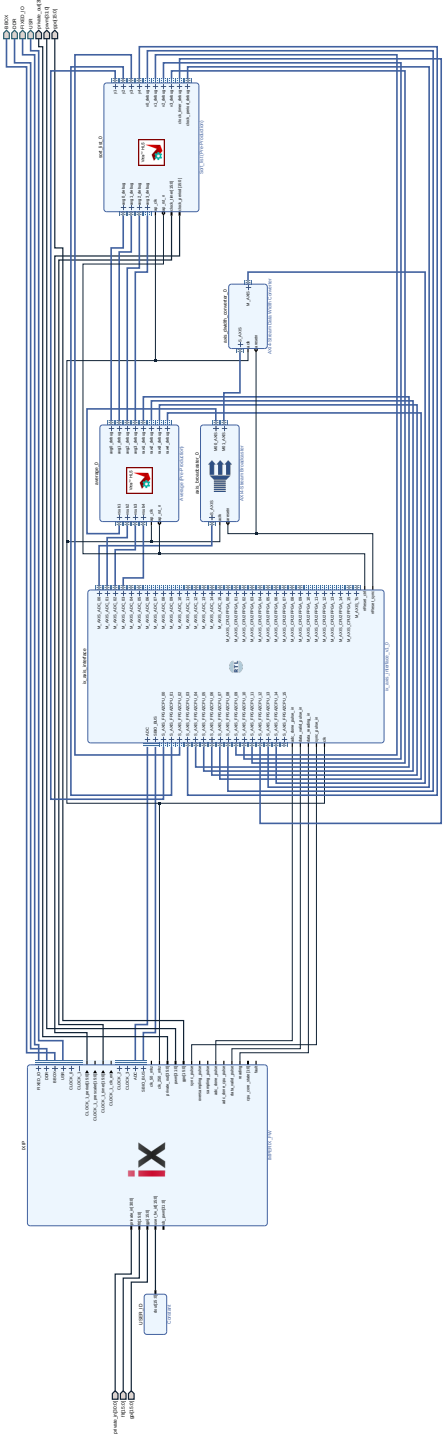


Figure 3.38: Vivado block design for implementing the submodule voltage balancing algorithm in FPGA.

Two operating scenarios—225 W and 2.5 kW output power—have been tested to demonstrate the effectiveness of the proposed control method and its improved THD_i performance compared to the existing approach.

Case 1: 225 W operation

For the 225 W case, the input DC voltage is 150 V and the load resistance is 1 Ω, resulting in rated output values of 15 A and 15 V for current and voltage, respectively. The corresponding experimental results are shown in Fig. 3.39, Fig. 3.40, and Fig. 3.41.

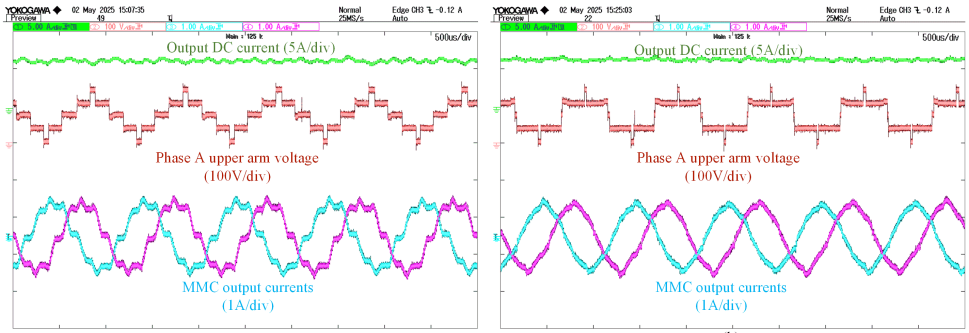


Figure 3.39: Case of 225 W rated power: comparison of MMR-SST with existing control method and proposed control method at an output current of 6.4 A. For clarity, the waveform types and scaling factors are labeled in the figure. (a) Existing phase shift control combined with discontinuous modulation index control, with control parameter $K = 0$ and phase shift angle $\alpha = 160^\circ$. The MMC output current THD = 15.5%. (b) Proposed continuous modulation index control, with shape factor $k = 0.95$ and phase shift angle $\alpha = 10^\circ$. The MMC output current THD = 8.5%.

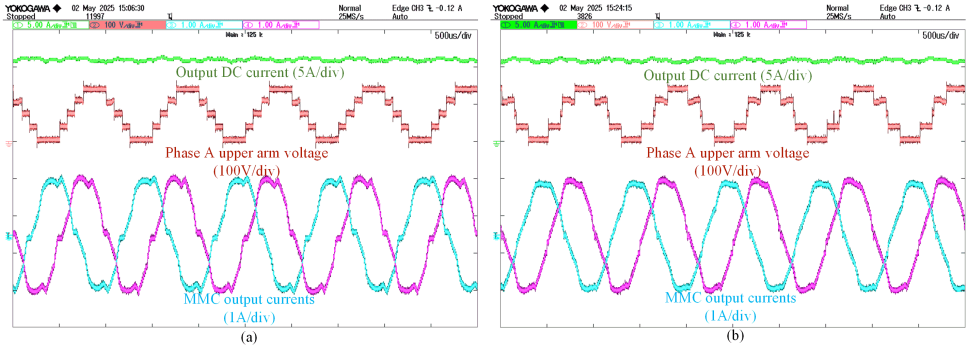


Figure 3.40: Case of 225 W rated power: comparison of MMR-SST with existing control method and proposed control method at an output current of 11 A. (a) Existing phase shift control combined with discontinuous modulation index control, with control parameter $K = 0$ and phase shift angle $\alpha = 90^\circ$. The MMC output current THD = 11%. (b) Proposed continuous modulation index control, with shape factor $k = 0.53$ and phase shift angle $\alpha = 10^\circ$. The MMC output current THD = 6.8%.

For the 225 W case, Fig. 3.39 illustrates the steady-state waveforms of the MMR-SST under both the existing control method (a) and the proposed control method (b), with an identical output current of 6.4 A. A significant difference in MMC output current THD_i

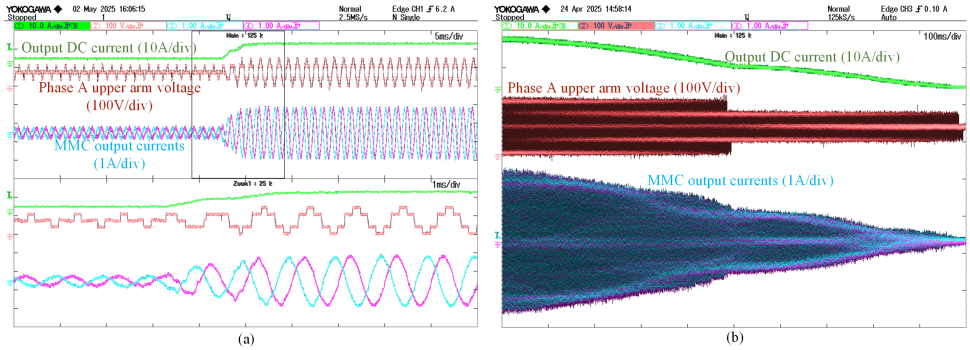


Figure 3.41: Case of 225 W rated power: dynamic waveform of MMR-SST with proposed continuous modulation index control. (a) Output current step response from 2 A to 10 A, demonstrating stable dynamic performance with no overshoot and a settling time of approximately 4 ms (±10% band). (b) Gradual change in output current from 13 A to 0 A by continuously varying the shape factor k.

is observed, with THD_i values of 15.5% and 8.5% for the existing and proposed methods, respectively. This is consistent with the simulation and theoretical analysis in Section 3.4.

Fig. 3.40 presents a different operating point at 11 A output current, which also demonstrates the THD_i improvement achieved by the proposed control method, with THD_i values of 11% and 6.8% for the existing and proposed approaches, respectively. It is noted that an output DC capacitor of 133 μF was used in the 225 W case, while a larger capacitance of 1.36 mF was adopted in the 2.5 kW case. These values were selected to ensure fast dynamic response of the current controller under different power levels, while maintaining the output current ripple within an acceptable range.

Fig. 3.41 illustrates the dynamic performance of the proposed control method. In Fig. 3.41(a), the output DC current command is varied from 2 A to 10 A. The system reaches steady state within approximately 4 ms (±10% band) without any overshoot, demonstrating a fast and well-damped dynamic response. Fig. 3.41(b) shows the output current response as the shape factor k is continuously increased from 0 to 2, during which the output current gradually decreases from 13 A to 0 A.

Case 2: 2.5 kW operation

For the 2.5 kW case, the input DC voltage is 300 V and the load resistance is 0.25 Ω, corresponding to rated output values of 100 A and 25 V. This high-current, low-voltage configuration is representative of electrolyzer applications. The experimental results are presented in Fig. 3.42, Fig. 3.43, and Fig. 3.44.

For the 2.5 kW case, Fig. 3.42 and Fig. 3.43 present two operating points at output currents of 48 A and 78 A, respectively. In both scenarios, the proposed and existing control methods yield comparable THD_i performance, with values of approximately 8% and 5.3%, respectively. This behavior can be attributed to the difference in output resistance between the 2.5 kW and 225 W operating conditions. In the 2.5 kW case, a much lower output resistance of 0.25 Ω is used, compared to 1 Ω in the 225 W case. According to the Q-factor definition in (3.5), the resulting quality factors Q_e are 0.76 and 0.19 for the 2.5 kW and 225 W cases, respectively. A higher quality factor leads to a narrower bandwidth, enhancing the resonant circuit's ability to reject current harmonics. Consequently, the THD_i difference

between the proposed and existing control methods is less significant, with both producing nearly sinusoidal output current waveforms.

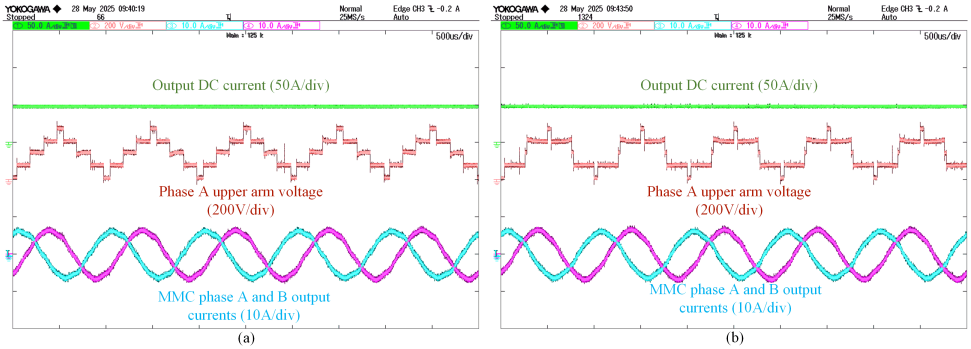


Figure 3.42: Case of 2.5 kW rated power: comparison of MMR-SST with existing control method and proposed control method at an output current of 48 A. (a) Existing phase shift control combined with discontinuous modulation index control, with control parameter $K = 0$ and phase shift angle $\alpha = 155^\circ$. The MMC output current THD = 8.11%. (b) Proposed continuous modulation index control, with shape factor $k = 0.92$ and phase shift angle $\alpha = 10^\circ$. The MMC output current THD = 8.02%.

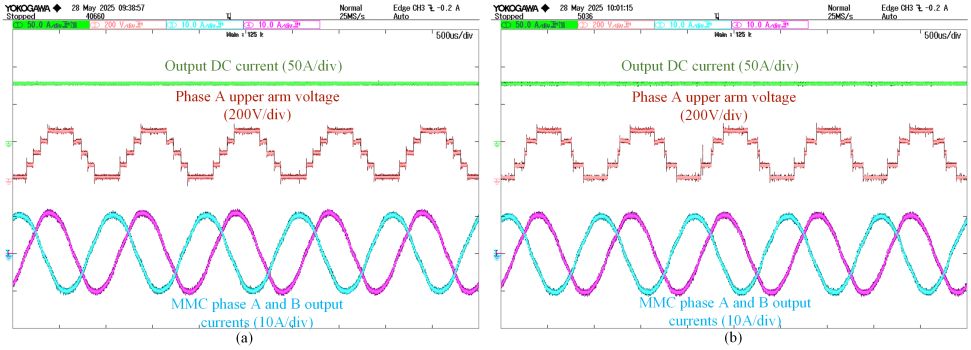


Figure 3.43: Case of 2.5 kW rated power: comparison of MMR-SST with existing control method and proposed control method at an output current of 78 A. (a) Existing phase shift control combined with discontinuous modulation index control, with control parameter $K = 0$ and phase shift angle $\alpha = 80^\circ$. The MMC output current THD = 5.32%. (b) Proposed continuous modulation index control, with shape factor $k = 0.478$ and phase shift angle $\alpha = 10^\circ$. The MMC output current THD = 5.27%.

Fig. 3.44 illustrates the dynamic performance of the proposed control method under the 2.5 kW condition. In Fig. 3.44(a), the output DC current command steps from 85 A to 20 A, and the system settles within approximately 7 ms (±10% band) with no overshoot, confirming fast and stable control behavior. Fig. 3.44(b) presents the output current response as the shape factor k increases continuously from 0 to 2, resulting in a gradual current decrease from 95 A to 0 A.

The experimental results under various operating conditions confirm that the proposed control method ensures stable operation and exhibits fast dynamic response. Under the low-power condition of 225 W, where the resonant circuit exhibits a lower quality factor,

the proposed method achieves significantly lower output current THD_i compared to the existing approach. This reduction in harmonic content could contribute to decreased conduction losses in the MMC, the secondary-side diode rectifier unit, and the transformer windings. In contrast, at higher output power (2.5 kW) with a higher quality factor, both control methods yield comparable THD_i performance due to the improved harmonic rejection capability of the resonant circuit. These results validate the effectiveness of the proposed control strategy across a wide operating range.

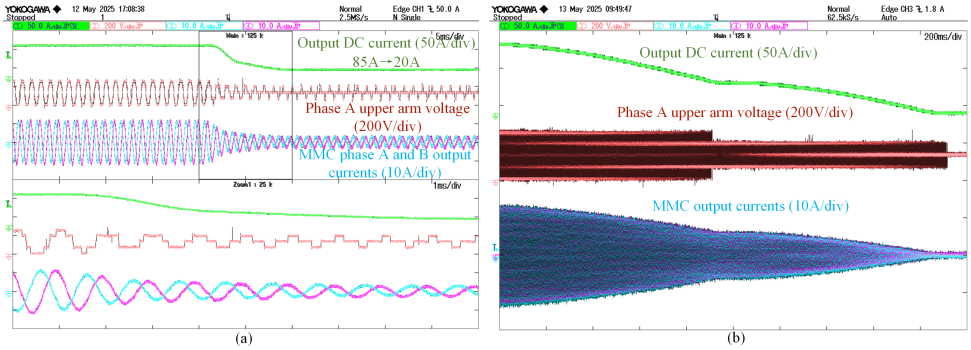


Figure 3.44: Case of 2.5 kW rated power: dynamic waveform of MMR-SST with proposed continuous modulation index control. (a) Output current step response from 85 A to 20 A, demonstrating stable dynamic performance with no overshoot and a settling time of approximately 7 ms (±10% band). (b) Gradual change in output current from 95 A to 0 A by continuously varying the shape factor k.

3.6 Conclusion

This Chapter presents an advanced control strategy for modular multilevel resonant converter based solid-state transformers for hydrogen electrolyzer applications. The proposed continuous modulation index control, with double-step staircase waveform modulation, significantly simplifies the control loop and controller parameter designs while maintaining equivalent controllability.

By setting the operating frequency to the resonant frequency and maintaining a low phase shift angle among submodules, the proposed method reduces magnetizing current, minimizes resonant current THD_i, and total power losses compared to the existing method. This fixed low phase shift angle resolves the issue of high resonant current THD_i in the existing method, which arises from the extended duration of discontinuous resonant current caused by large phase shift angles.

The effectiveness of the proposed strategy is validated through both software simulation and down-scaled experimental validation, demonstrating comparable efficiency and THD performance to the existing control method, as well as rapid dynamic performance. The results indicate the potential applicability of the proposed strategy to medium-voltage hydrogen electrolyzer systems.

4

Data-Driven Modeling of Magnetic Losses for SST Design Optimization

Traditional methods such as Steinmetz's equation (SE) and its improved variant (iGSE) have demonstrated limited precision in estimating power loss for magnetic materials. The introduction of Neural Network technology for assessing magnetic component power loss has significantly enhanced accuracy. Yet, an efficient method to incorporate detailed flux density information—which critically impacts accuracy—remains elusive. Our study introduces an innovative approach that merges Fast Fourier Transform (FFT) with a Feedforward Neural Network (FNN), aiming to overcome this challenge. To optimize the model further and strike a refined balance between complexity and accuracy, Multi-Objective Optimization (MOO) is employed to identify the ideal combination of hyperparameters, such as layer count, neuron number, activation functions, optimizers, and batch size. This optimized Neural Network outperforms traditionally intuitive models in both accuracy and size. Leveraging the optimized base model for known materials, transfer learning is applied to new materials with limited data, effectively addressing data scarcity. The proposed approach substantially enhances model training efficiency, achieves remarkable accuracy, and sets an example for Artificial Intelligence applications in loss and electrical characteristic predictions with challenges of model size, accuracy goals, and limited data. This framework shows strong potential for future extension to medium-frequency transformer loss modeling and system-level optimization in MW-scale solid-state transformer applications.

This chapter is based on:

-**Z. Li** et al., "A Data-Driven Model for Power Loss Estimation of Magnetic Materials Based on Multi-Objective Optimization and Transfer Learning," in IEEE Open Journal of Power Electronics, vol. 5, pp. 605–617, 2024

4.1 Introduction

The empirical Steinmetz Equation (SE), introduced in 1890, has long served as the basis of standard loss modeling techniques in power magnetics and has been extended through various improvements, such as the improved generalized Steinmetz equation (iGSE). Nevertheless, the accuracy of these approaches remains limited. For the N87 ferrite dataset reported in the literature, the iGSE model shows a 95th percentile loss estimation error of approximately 12 %–25 % over a temperature range from 25 °C to 90 °C [120]. The imprecise model leads to a rough magnetic design, and therefore a large design margin is required to achieve acceptable loss performance of magnetic components.

The 2023 MagNet Challenge [121–123], led by Princeton University, focuses on improving the Steinmetz equation by leveraging an extensive dataset encompassing diverse materials, frequencies, waveform shapes, and temperatures. The objective is to develop innovative and refined data-driven methods to deepen the power electronics community's grasp of magnetic core properties, particularly in core loss. Extensive data for ten known materials and limited data for five unknown materials were released consecutively. The final evaluation criteria are based on the accuracy of loss prediction for the five unknown materials and the complexity of the model.

To accurately predict the loss of magnetic material, one possible approach is using neural networks. Neural networks have been utilized in the modeling of magnetic hysteresis loops, as referenced in [124, 125]. However, using hysteresis loops as an indirect predictor of power loss can introduce notable inaccuracies in the estimation of core losses due to minor phase discrepancies, as discussed in [123].

A more effective approach involves employing neural networks to directly predict the power loss and temperature of magnetic components [126–136]. Reference [126] introduced Neural Network-aided Loss Maps (NNALMs) for both inductors and transformers, taking load conditions as inputs to predict both winding and core losses with an average error of less than 10%. Additionally, a Knowledge-Aware Artificial Neural Network (KANN) was developed in [128, 129], incorporating the output of the SE function or iGSE function as one of the inputs to a Feedforward Neural Network (FNN), thereby achieving high accuracy even with limited training datasets. Due to the minimal computational demands of trained FNNs, Reference [131] proposed utilizing two FNNs to predict real-time maximum temperatures and loss distributions in medium frequency transformers. Reference [127] employed a Convolutional Neural Network (CNN) to forecast inductance and core loss. One area for further investigation in these studies is the inclusion of detailed flux density waveform information, which has the potential to significantly enhance the accuracy of power loss predictions.

Based on extensive open-source magnetic materials data provided by MagNet [137], the current state-of-the-art methodologies in this field are those presented in [123], which include various neural network structures such as the Feedforward Neural Network (FNN), Long Short-Term Memory (LSTM), and the Encoder-Decoder structure, as depicted in Fig. 4.1(a), (b), and (c), respectively. The FNN uses a four-layer FNN, taking peak flux density B, duty ratio D, and fundamental frequency f to predict core loss density P_V. The disadvantage of this method is that the B waveform shape information cannot be included by only using the peak flux density value. One possible approach is to train different FNNs for different B waveforms. However, there are an unlimited number of B waveform shapes.

Thus, it is impractical to first categorize and then design separate FNNs for each case.

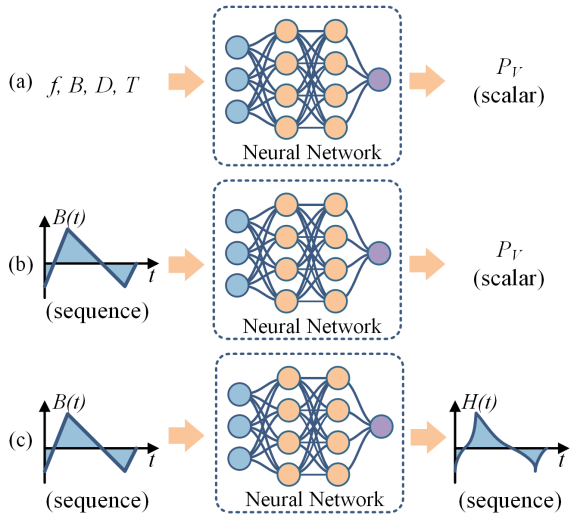


Figure 4.1: Three approaches for modeling magnetic material properties using neural networks: (a) scalar-to-scalar mapping using a feedforward neural network (FNN), (b) time-series-to-scalar mapping using a long short-term memory (LSTM) network, (c) time-series-to-time-series mapping using an encoder–decoder structure.

To effectively capture the waveform shape information of the flux density, other advanced neural networks can be applied, e.g., LSTM and encoder-decoder structures. LSTM and encoder-decoder architectures offer enhanced temporal data processing and sequence-to-sequence prediction capabilities [138, 139], outperforming traditional FNNs in handling long-term dependencies and complex patterns in time-series data. However, these models are more complex and require longer training time, which can be a critical drawback in practical applications where large volumes of data need to be processed with limited computational resources. Section 4.3 will analyze these advanced methods in detail.

To effectively encapsulate the information of the B waveform while reducing model complexity, employing FFT (Fast Fourier Transform) in conjunction with FNN presents a more efficient approach. This paper employs the FFT to convert the waveform data into its harmonic components. These harmonics are subsequently utilized as inputs for the FNN. This approach limits the number of parameters and decreases the complexity; thus, the training time is considerably shorter compared to other more complex methods. To the best of the authors' knowledge, this is the first research to integrate FFT with FNN for estimating magnetic power loss.

In the AI modeling process, a common dilemma is balancing model size with accuracy, where a model with more parameters typically offers higher accuracy but demands greater computational resources and larger dataset. The trade-off among various alternatives for generating the FNN dataset is analyzed in [130]. References [132, 133] are concentrated on optimizing the number of layers and neurons in neural networks. Reference [134] demonstrated that the GELU activation function and Huber loss function outperform the RELU activation function and MSE loss function. Despite these advancements, there

remains an evident gap in the systematic optimization of neural network hyperparameters for magnetic component power loss estimation applications.

A viable solution to this challenge is implementing Multi-Objective Optimization (MOO) [140], where accuracy and the number of parameters are set as objectives. This approach facilitates the identification of optimal model hyperparameters from the generated Pareto Front, effectively resolving the trade-off between complexity and performance. In this study, Optuna is employed for MOO, which is an efficient hyperparameter optimization framework renowned for its simplicity and flexibility in various optimization tasks [141].

Although the methods mentioned above are sufficient for materials with extensive data, in real-world applications, engineers may not be able to measure a large amount of data when dealing with new materials. Yet, there is often a need to predict the performance of new materials quickly and accurately, which is exactly the goal of the Magnet competition. In such situations, transfer learning can play a significant role [142, 143]. Transfer learning allows the application of knowledge acquired from extensive datasets of known materials to predict the characteristics of new materials, even with limited data. This approach is particularly effective in reducing the need for extensive data collection for new materials, thereby accelerating the prediction process while maintaining accuracy.

In summary, the main contributions of this Chapter include the following:

1. An FFT+FNN neural network structure for magnetic loss estimation is proposed, which can effectively capture key information of the B waveforms influencing the core loss. Compared to the advanced LSTM and encoder-decoder structure, the proposed structure has the simplest structure, comparable or better accuracy, and the shortest training time.

2. The necessity of conducting multi-objective optimization (MOO) and selecting hyperparameter combinations from the Pareto front is demonstrated, enabling a balanced trade-off between model complexity and prediction accuracy.

3. It is shown that applying transfer learning to new magnetic materials can mitigate the loss prediction accuracy degradation caused by data scarcity.

This chapter presents a neural network modeling approach that integrates multi-objective optimization and transfer learning to accurately predict magnetic core loss under limited data availability. Accordingly, the chapter is organized as follows. Section 4.2 presents the employed FNN architecture and elaborates on the rationale behind the chosen input layer format and the number of harmonics. Section 4.3 details a comparative analysis with other sophisticated AI methodologies. Section 4.4 details two approaches for predicting power loss in new materials: normal training and transfer learning, each integrating MOO. This Section further compares the developed FNNs, aiming to identify the most effective model regarding parameter count and accuracy. Finally, Section 4.5 concludes the Chapter.

4.2 Provided Dataset and Proposed Neural Network

This Section introduces the dataset used in this study and the proposed neural network. The architecture, input representation, and training procedure are outlined to establish the foundation for subsequent Sections.

4.2.1 MagNet Challenge Provided Dataset

Table 4.1 describes the number of data points provided by the MagNet challenge. Each data point encompasses single-cycle B–H loop data with 1024 time steps per cycle. The original steady-state waveforms contain multiple cycles as shown in Fig. 4.2, which are segmented and interpolated to obtain a normalized single-cycle waveform as shown in Fig. 4.3, in order to reduce data redundancy and improve training efficiency.

Table 4.1: Number of data points for the ten known materials in the MagNet challenge.

Material	Sine	Triangular	Trapezoidal	Total
TDK N27	479	3542	7375	11396
TDK N30	500	2691	5787	8978
TDK N49	334	2839	5429	8602
TDK N87	1426	13190	26000	40616
Ferroxcube 3C90	1601	13123	25989	40713
Ferroxcube 3C94	1776	12627	25665	40068
Ferroxcube 3F4	146	2314	4103	6564
Ferroxcube 3E6	503	2045	4448	6996
Fair-Rite 77	482	3528	7434	11444
Fair-Rite 78	472	3524	7384	11380

For each material, the provided data includes five CSV files, including B Field ($N \times 1024$, in T), H Field ($N \times 1024$, in A/m), Frequency ($N \times 1$, in Hz), Temperature ($N \times 1$, in °C), and Volumetric loss ($N \times 1$, in W/m^3), where N refers to the number of data points. The B field data are presented in various waveforms — sinusoidal, triangular, and trapezoidal — to simulate different excitations in magnetic materials. Temperature values are distributed at 25°C, 50°C, 70°C, and 90°C. The frequency of the B field varies from 50 kHz to 800 kHz. The provided data have been open-sourced in GitHub [144].

For the final test, the competition committee has provided five new materials, as shown in Table 4.2. The identities of the new materials are undisclosed and designated as A, B, C, D, and E. The dataset has the complete information, including B Field, H Field, Frequency, Temperature, and Volumetric loss. As seen in the tables, the data points of the five new materials are much fewer than the ten existing materials. This setup holds practical significance as there are countless types of magnetic materials in reality, and engineers often need to accurately predict the losses of these materials based on limited data obtained in a short period. The data scarcity scenario will be considered in the subsequent analysis.

In machine learning, datasets with complete information, encompassing parameters such as the B Field, H Field, Frequency, Temperature, and Volumetric loss, are typically divided into three sets: training, validation, and test. The training dataset is used to train the model, allowing it to learn and adapt to the data patterns. It usually comprises the largest data portion, often ranging from 50% to 80%. The validation dataset serves as a tool for tuning the model parameters and providing an unbiased evaluation of a model fit

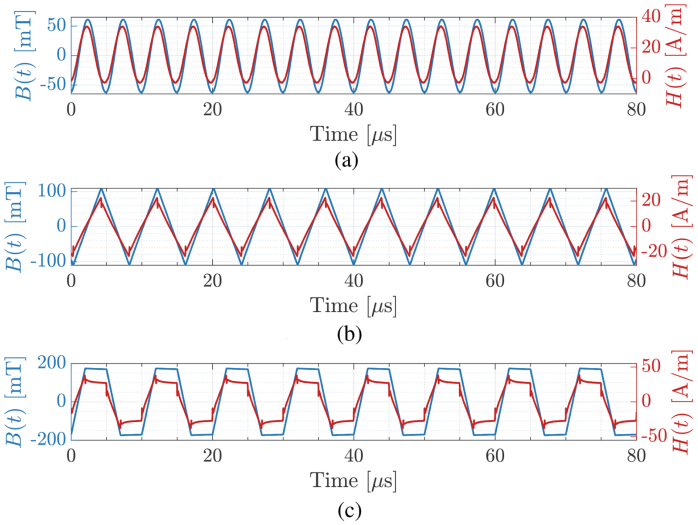


Figure 4.2: Examples of full-length waveforms measured with N87 ferrite material [121]: (a) sinusoidal wave; (b) triangular wave; (c) trapezoidal wave.

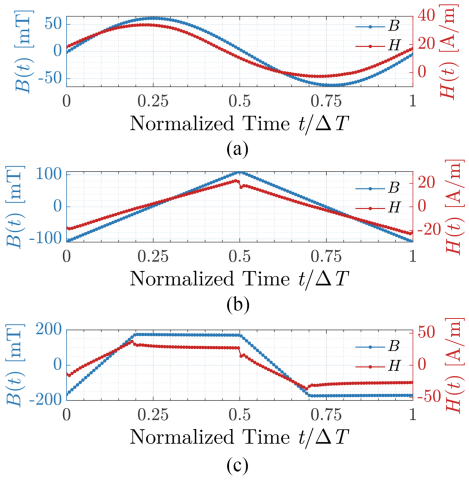


Figure 4.3: Examples of single-cycle waveforms [121], corresponding to the full-length waveforms shown in Fig. 4.2: (a) sinusoidal wave; (b) triangular wave; (c) trapezoidal wave.

Table 4.2: Number of data points of the five new materials of MagNet challenge. The identities of the new materials are undisclosed.

Material	Sine	Triangular	Trapezoidal	Total
Material A	101	694	1637	2432
Material B	364	2253	4783	7400
Material C	215	1679	3463	5357
Material D	145	400	35	580
Material E	57	667	1289	2013

during the training phase. It typically constitutes about 10% to 25% of the data. Finally, the test dataset is used to assess the performance of the model after the training is complete. It provides an unbiased evaluation of the final model fit and is usually about 10% to 25% of the data. The exact proportions can vary based on the size and specifics of the dataset. A typical training process will be demonstrated in Section 4.2.3.

4.2.2 Proposed FFT+FNN Method

The proposed Neural Network structure is shown in Fig. 4.4. Initially, the magnetic flux density $B(t)$ is broken down into its harmonic components, characterized by frequencies f, magnitudes M, and phases ϕ. For training the FNN, we input the harmonic frequencies f and magnitudes M, along with temperature data T. The inputs of FNN are thus formatted as $[f_1, M_1, f_2, M_2, \ldots, f_n, M_n, T]$, as illustrated in Fig. 4.4. The rationale behind the selection of this input format is discussed further in Subsection 4.2.4.

Apart from the input layer, as illustrated in Fig. 4.4, the FNN also has an output layer and several hidden layers. The output layer directly generates the predicted volumetric loss P_v. The interconnected parameters of the network, which form the core of the FNN's operational mechanics, are mathematically characterized as follows

$$z_i^j = \sigma\left(\sum_{k=1}^{n}\left(w_{k,i}^j \cdot z_k^{j-1} + b_k^j\right)\right) \tag{4.1}$$

where w represents the weight connecting each pair of hidden neurons, while b denotes the bias associated with each hidden neuron. The subscripts indicate the indices of hidden neurons, whereas the superscripts refer to the layer indices. Each hidden neuron employs a nonlinear activation function, $\sigma(x)$, enabling the network with the ability to learn nonlinear relationships. The term z computes the output of each hidden neuron, with its subscript and superscript following the same notation used for w and b. This architecture enables the FNN to effectively model complex relationships in magnetic materials, such as those between B, Frequency, and Temperature, ultimately allowing the output layer to predict power loss precisely.

In this study, as the analyzed $B(t)$ and $H(t)$ waveforms are in a steady state, FFT serves as an efficient method for decomposing these signals. Should non-stationary signals be analyzed in other studies, alternative sophisticated analytical tools, such as Wavelet

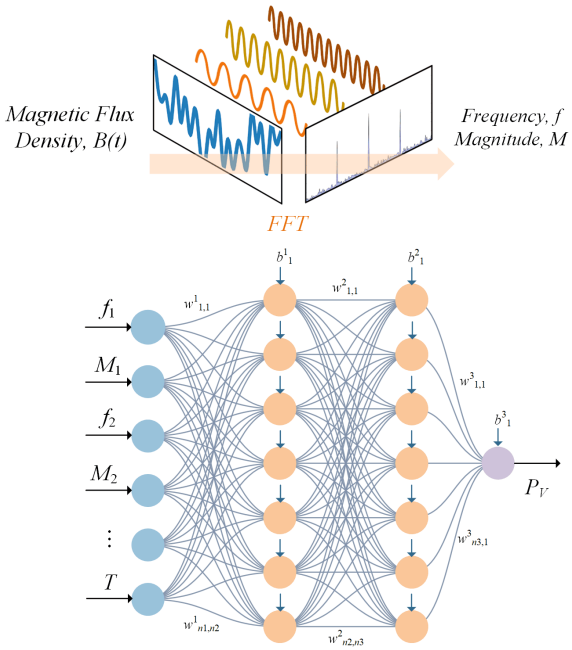


Figure 4.4: Proposed FNN with FFT structure. The magnetic flux density is first decomposed into harmonics using FFT, then fed into the FNN.

Transform, Empirical Mode Decomposition (EMD), and Walsh–Hadamard Transform, could be employed to address their complexity.

4.2.3 Training Process of the Proposed Method

This Section presents an example of the training process and explains the hyperparameters of the model. Suppose the FFT+FNN model aims to predict the N27 material loss, and N27 data is split into 60%, 20%, and 20% for train, validation, and test datasets, respectively.

In this example, we select $[f_1, M_1, f_2, M_2, \ldots, f_{10}, M_{10}, T]$ with ten harmonics information of B as the input format of the FNN. The number of neurons in the hidden layers is determined based on experience, which is (32, 64, 32), and the activation function is ReLU. The batch size is set to 128, which refers to the number of training samples processed before the internal parameters of the model are updated. This size balances the training efficiency and the computational resource requirements. The training optimizer, set as Adam, is an algorithm used to adjust the weights of the neural network to minimize the loss function, thereby improving the performance of the model [145].

The model is trained in PyTorch, an open-source machine learning library widely used for deep learning and neural network modeling applications, known for its flexibility and ease of use [146]. An exponentially decayed learning rate strategy is implemented to yield a better model convergence, where the initial learning rate is 0.004, and the decaying rate is 90% per 150 epochs [123]. In Section 4.4 a hyperparameter optimization will be carried out.

Fig. 4.5 shows an example of the training process. In the model training process, training and validation losses are computed to monitor and enhance performance. Each epoch, defined as a complete pass through the training dataset, involves adjusting model weights to minimize training loss. During each epoch, the training dataset is shuffled to present the data in a randomized order, ensuring that the model does not learn any potential sequence biases and improving its ability to generalize from the training data. Simultaneously, validation loss is evaluated to assess the generalization capabilities of the model. A pattern where validation loss initially decreases and then increases suggests overfitting, indicating that the model excessively captures noise and fluctuations in the training data, impairing its generalization ability.

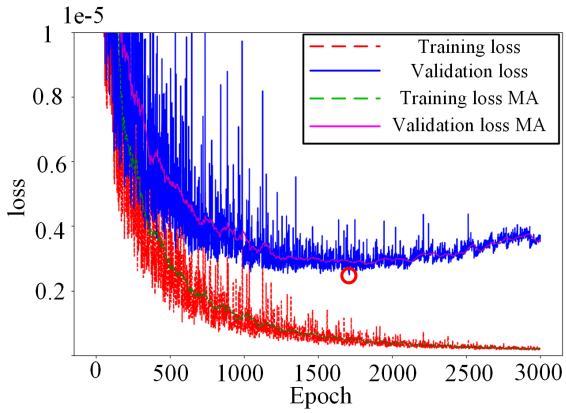


Figure 4.5: Example of training progress and early stopping method, with MA indicating moving average. The red circle marks the epoch with the lowest validation loss, and the corresponding model is saved during training.

To prevent overfitting, an early stopping technique is applied. This approach terminates the training when no improvement in validation loss is observed over a predefined number of epochs, set here as 2000. If the validation loss fails to decrease over these epochs, the model may no longer be improving and could be overfitting. For instance, as illustrated in Fig. 4.5, where the point of lowest validation loss is circled in red, the model corresponding to this epoch is saved as the final model. This ensures that the most efficient version of the model, with optimal generalization capability, is retained for practical application. The early stopping method is used in the following model training process.

Upon finalization of the model, it was applied to the test dataset to evaluate performance. This process entailed comparing the predicted and measured core loss to ascertain model accuracy. Fig. 4.6 presents an example of the error distribution. The error analysis in this study utilizes three key metrics for assessing the accuracy of core loss predictions. *Average Error* is calculated as the mean of the relative differences between predicted and actual values across all data points, providing a general indicator of prediction accuracy. The *95% Error*, defined as the value below which 95% of observed errors fall, offers insight into the typical error range for the majority of predictions. *Maximum Error*, representing the highest error in the dataset, indicates the largest deviation between predictions and actual measurements, illustrating the worst-case scenario in model performance. In subsequent

Sections, these three metrics are presented directly without repeating error distribution diagrams.

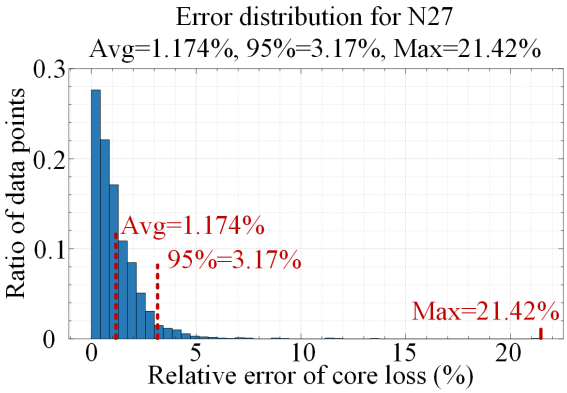


Figure 4.6: Distribution histogram of the N27 core loss relative errors, including average error, 95% error, and maximum error.

4.2.4 Design of Input Layer

Different input formats of FNN can be applied. Apart from the one $[f_1, M_1, f_2, M_2, \ldots, f_n, M_n, T]$ as presented in Fig. 4.4, other input formats also have been considered, for example $[f_1, M_1, \phi_1, f_2, M_2, \phi_2, \ldots, f_n, M_n, \phi_n, T]$, where ϕ_k represents the phase information of the kth harmonic; and $[M_1, M_2, \ldots, M_n, f_1, T]$, where in this case only the fundamental harmonic frequency is included. These three cases are marked as case 0, case 1, and case 2, respectively.

A comparison between these three cases has been carried out based on N27 material. The number of neurons in the hidden layers is determined based on experience. The data split method and other hyperparameters are the same as in Subsection 4.2.3.

Table 4.3 shows the comparison results of the three cases, and there are two conclusions. First, adding harmonics phase information does not help increase loss prediction accuracy. Second, when the model is trained using only a single fundamental frequency as input, its performance is inferior compared to when it is trained with both the frequencies and magnitudes of the harmonic components paired together. This observation holds under the scenario where the network parameters are initially selected based on empirical experience and are not subject to further optimization. Therefore, the inputs for the FNN are chosen to be in the format of $[f_1, M_1, f_2, M_2, \ldots, f_n, M_n, T]$.

A further question is how many numbers of harmonics are suitable to consider for model training and prediction. In the provided data of ten materials, there are three different types of B waveforms, i.e., sinusoidal, triangular, and trapezoidal. For sinusoidal waveforms, only a fundamental component exists. As for triangular and trapezoidal waveforms, two examples are shown in Fig. 4.7. A general impression is that the magnitude is negligible over the third harmonic.

Three different FNN models are built for three, five, and ten harmonic inputs, respectively. A comparison between these three FNNs is shown in Table 4.4. The model training

Table 4.3: Comparison of different FNN input formats. Case 0 represents $[F_1, M_1, F_2, M_2, \ldots, F_N, M_N, T]$, with harmonics magnitudes and frequencies information. Case 1 represents $[F_1, M_1, \Phi_1, F_2, M_2, \Phi_2, \ldots, F_N, M_N, \Phi_N, T]$, with harmonics magnitudes, phases, and frequencies information. Case 2 represents $[M_1, M_2, \ldots, M_N, F_1, T]$, with harmonics magnitudes information and only the fundamental frequency.

Cases	Neurons in hidden layers	Total number of parameters	Avg. relative Error on test set
0	(32, 64, 32)	4929	1.17
1	(64, 64, 64)	10433	2.20
2	(32, 64, 32)	4641	1.69

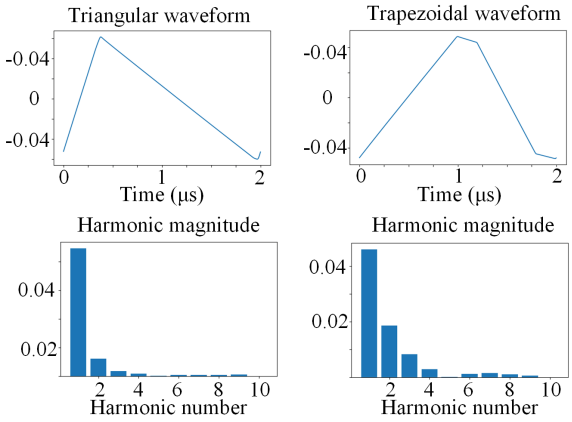


Figure 4.7: B waveform examples and harmonic magnitudes. The triangular and trapezoidal B waveforms are randomly selected from the N27 dataset.

and testing settings are the same as the tests in Table 4.3.

The difference in neuron settings in the middle layer is due to the different number of inputs. As can be seen from the comparison results, though with the total number of parameters differences, the results of using three harmonics, five harmonics, and ten harmonics are similar. Furthermore, observing Fig. 4.7 suggests that reducing the number of considered harmonics is justified, as the magnitudes of higher harmonics appear negligible. For the simplicity of the model structure, which is essential for training and future optimization, three harmonics are chosen for the input. Consequently, the input format for the FNN in this study has been established as $[f_1, M_1, f_2, M_2, f_3, M_3, T]$.

Table 4.4: Comparison of different numbers of harmonics as input

No. harmonics	Neurons in hidden layers	Total number of parameters	Avg. Error on test set	Max. Error on test set
3	(16,32,16)	1217	1.38	7
5	(16,32,16)	1281	1.44	12
10	(32,64,32)	4929	1.17	21

4.3 Comparison with the State of the Art

With the given magnetic flux density $B(t)$, magnetic field strength $H(t)$, frequency f, temperature T, and power loss P information, different AI models can be applied to predict the power loss. Apart from the scalar-to-scalar model presented in this paper, Ref. [123] also offered two other models: a sequence-to-scalar model using LSTM plus FNN, and a sequence-to-sequence model using an encoder-decoder structure with LSTM. This Section compares the methods introduced in this paper with those previously described in [123]. A detailed description of these two methods is provided in [123]. The following Subsections briefly outlines their key concepts.

4.3.1 Sequence-to-Scalar: LSTM + FNN Model

To effectively address the challenge posed by the diverse shapes of B waveforms, an alternative approach is to employ a sequence-based neural network structure.

The LSTM network is a key architecture in regression problems with sequential input. Its unique capability lies in memorizing information across data sequences, making it highly suitable for analyzing time series data. As shown in Fig. 4.8(a), the input gate i_t, forget gate f_t, and output gate o_t are essential to the functionality of the LSTM, which regulate information flow and enable selective memory storage over specific intervals. Detailed math descriptions can be referred to Ref. [123].

Based on the LSTM cell structure, a sequence-to-scalar LSTM-based model is developed, using time sequences of flux density $B(t)$ as input (1024 time steps per cycle) and predicting volumetric power loss as output. Fig. 4.8(b) displays the model structure, where the LSTM is taken as the input layer to process the entire flux density waveform. LSTM outputs are then concatenated with temperature and frequency information to feed into an FNN to perform core loss regression. This specific design features an LSTM with 18 cell states and 18 hidden states, and the FNN consists of three hidden layers (each with 12 neurons), resulting in an output representing the volumetric magnetic core loss. Overall, the model comprises 2089 parameters.

To assess the performance of this LSTM-based core loss model, the network depicted in Fig. 4.8(b) has been synthesized and trained using PyTorch. N27 data are randomly split into 60%, 20%, and 20% for train, validation, and test datasets, respectively. The training results are shown in Table 4.5. In addition, the training time for each model is shown to compare the required computation resources. The neural network trainings are conducted in a PC equipped with an AMD Ryzen 7 5800H processor and an NVIDIA GeForce RTX 3060 graphics card. The results will be analysed in Subsection 4.3.3.

4.3.2 Sequence-to-Sequence: Encoder-Projector-Decoder Model

Beyond the direct prediction of power loss in magnetic components using $B(t)$, Frequency, and Temperature data, an alternative approach involves initially forecasting the time sequence of $H(t)$. Subsequently, both $B(t)$ and $H(t)$ can be utilized to compute the power loss:

$$P_{\mathrm{v}} = \frac{1}{T} \int_{B(0)}^{B(T)} H(t)\, dB(t) \tag{4.2}$$

The encoder-decoder network framework [147], a leading-edge architecture, has gained

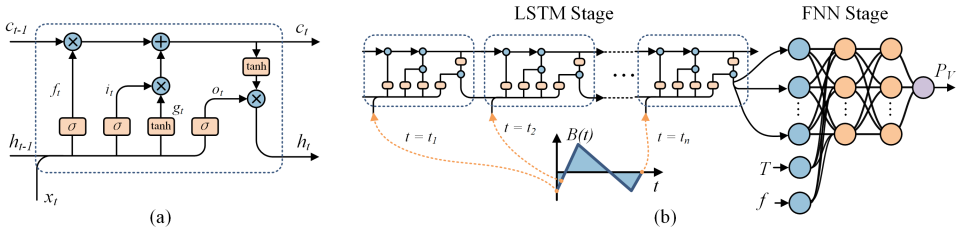


Figure 4.8: Sequence-to-scalar LSTM network structure: (a) basic structure of the LSTM cell, (b) structure of the complete LSTM-FNN. The B waveform is initially input into the LSTM network, and then the output of the LSTM is concatenated with temperature T and frequency f to feed into the FNN.

considerable interest in recent years for its effectiveness in sequence-to-sequence regression challenges. The encoder-decoder network framework can also be applied to this magnetic B–H hysteresis loop prediction target.

To include Temperature and Frequency information, Ref. [123] proposed an encoder-projector-decoder structure as shown in Fig. 4.9. The encoder comprises a single-layer LSTM network with 32 states, employing input, forget, and output gates of LSTM to process the sequence $B(t)$. This processing captures sequence characteristics in hidden and cell states. Additional inputs, i.e., Temperature T and Frequency f, are combined with these states to feed into a projector consisting of two three-layer FNNs with 64 neurons in each layer. The projector adjusts state values in response to these additional inputs, resulting in updated states. These updated states are then utilized to initialize the decoder, which has a structure identical to the encoder's. Utilizing the updated hidden and cell states, the decoder produces the output sequence $H(t)$.

The network employs mean-squared error as the loss function to measure the discrepancy between the predicted and target $H(t)$. This function is used to adjust the weights and biases within the network. To manage the higher computational demands, the $B(t)$ and $H(t)$ are down-sampled to 102 time steps per cycle. Other settings and training environments are the same as the LSTM+FNN model. After the model is finalized, the power loss is calculated according to (4.2) with the input $B(t)$ and the predicted $H(t)$. The results are shown in Table 4.5.

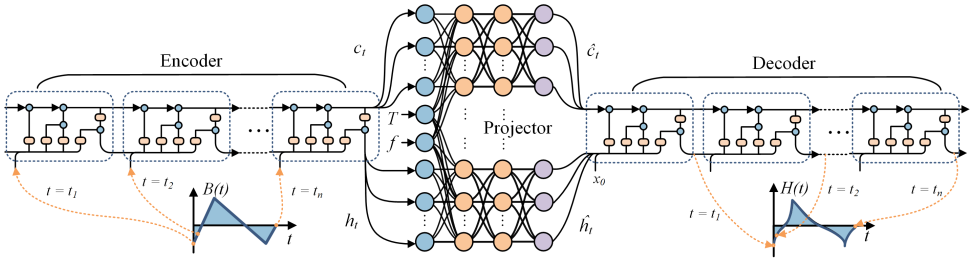


Figure 4.9: Encoder-projector-decoder network structure. Both the encoder and decoder comprise LSTM networks. The projector integrates the encoder's cell and hidden states with temperature T and frequency f as FNN inputs, generating the cell and hidden states for the decoder.

4.3.3 Comparison Results and Analysis

Table 4.5 shows the training results of the LSTM+FNN, the encoder-projector-decoder structure, and the proposed FFT+FNN method. Additionally, the optimized FFT+FNN detailed in Subsection 4.4.1 is also shown for benchmarking.

Table 4.5: Comparison between the FNN, LSTM plus FNN, and Encoder-Decoder based on N27 data. The optimized FFT+FNN represents the MOO results shown in Subsection 4.4.1

Cases		Total number of parameters	Training time	Avg. relative error on the test set
FFT+FNN	Original	1217	~1 hour	1.38%
	Optimized	1419	~1 hour	0.75%
LSTM+FNN		2089	~20 hours	1.37%
Encoder-projector-decoder		28097	~20 hours	3.34%

The encoder-projector-decoder is the most complex model, but the power loss estimation is less accurate than the other two. The reason is that the power loss is not directly generated as the output of the neural network. On the contrary, the power loss is indirectly calculated by integrating $B(t)$ and $H(t)$. A slight phase discrepancy in the predicted $H(t)$ sequence might not cause a significant relative error in sequence-to-sequence regression, yet it could have a substantial effect on the accuracy of core loss prediction [123].

In contrast to the encoder-projector-decoder structure, LSTM+FNN and the original FFT+FNN, which directly correlate B, f, and T data with power loss, show equally high performance. This leads to the first insight: complexity alone does not guarantee higher accuracy in power loss prediction; direct prediction of power loss as the network's output can achieve better results, because in this case any intermediate errors, e.g., phase error of $H(t)$, are avoided.

Although the LSTM+FNN effectively captures detailed information from B waveforms, its performance does not surpass that of FFT+FNN. This observation leads to the second insight: within the scope of the most general waveforms for power-electronic magnetic components, which is covered by the existing dataset, the results from FFT+FNN show that the harmonic magnitudes and frequencies can represent the dominant characteristics influencing the core loss.

Besides, this sequence-to-scalar model presents two disadvantages compared to the proposed scalar-to-scalar model. First, it is more complex and requires longer training time, which is unsuitable for further optimization. Second, in the case of transfer learning using the data measured by other research groups, adjustments like down-sampling/up-sampling or modifying the model structure might be needed for transfer learning, especially when handling data sequences of different lengths.

In comparison, the proposed FNN model is the simplest and quickest for training. With hyperparameter optimization of FNN, the model's performance can significantly increase. Given its simplicity and high accuracy, the proposed FNN has been demonstrated to be suitable for the following development and optimization.

4.4 Multi-Objective Optimization, Transfer Learning and Comparison

The overall model construction and selection methods for the five new materials are presented in Fig. 4.10. In the normal training approach without transfer learning, for the five new materials, the FNN model for each material is first optimized with the MOO tool Optuna, as detailed in the next Section. New materials training data as shown in Table 4.2 are split into 70%, 20%, and 10% for training, validation, and test purposes, respectively. The proportion of the training dataset is slightly higher, at 70%, due to the limited quantity of data. This approach aims to maximize the use of available data for training purposes. Then, the most effective hyperparameter combination with a low number of parameters and low validation loss is selected. The model performance on the test dataset is recorded for later comparison.

Although with MOO, the test performance is relatively satisfactory with the normal training process, due to the low amount of new material data, a better approach is to use transfer learning. This method holds significant importance in real-world scenarios, such as for designers who may lack adequate data on new materials required for normal training models. This part will be analyzed in Subsection 4.4.2. The second approach with transfer learning, as shown in Fig. 4.10, also starts with a MOO for the ten existing materials. This will increase the accuracy of the following step, which uses transfer learning.

The data on the ten existing materials are split into 70%, 15%, and 15% for training, validation, and test purposes, respectively. This distribution strategy differs slightly from the previous one, as in this case, the ten existing materials data are more abundant, providing a more comprehensive basis for analysis. Once the optimal model for each of the ten known materials is determined, the five new materials will be subjected to transfer learning across the ten models through fine-tuning. As a result, 50 new transfer-learned models for the five new materials will be acquired, and the test data results will be recorded. The transfer-learned and normal training results described previously will be compared to select the final best model.

4.4.1 Multi-Objective Optimization

In assessing the neural network model, prediction accuracy and the number of parameters are crucial metrics. While accuracy reflects the model's effectiveness, the parameter count directly indicates its complexity and significantly impacts the time required for training and fine-tuning. To optimize the model considering both values, a MOO is needed.

MOO aims to find the optimal set of parameters, simultaneously optimizing multiple objectives, leading to trade-offs and compromises. Optuna, a popular Python library, provides a comprehensive framework for conducting MOO. Utilizing Optuna for MOO, we focus on two primary objectives: reducing the validation loss to enhance model accuracy and minimizing the number of parameters. Different hyperparameter tuning methods have been analyzed in [148, 149], and NSGA-II (Non-dominated Sorting Genetic Algorithm II) is favored in this study as the optimization engine for its effective balance in ranking and diversity preservation in MOO contexts [150].

The search space is defined as follows: the number of middle layers in the FNN structure varies between 2 and 5, each containing 8 to 64 neurons. The activation functions considered

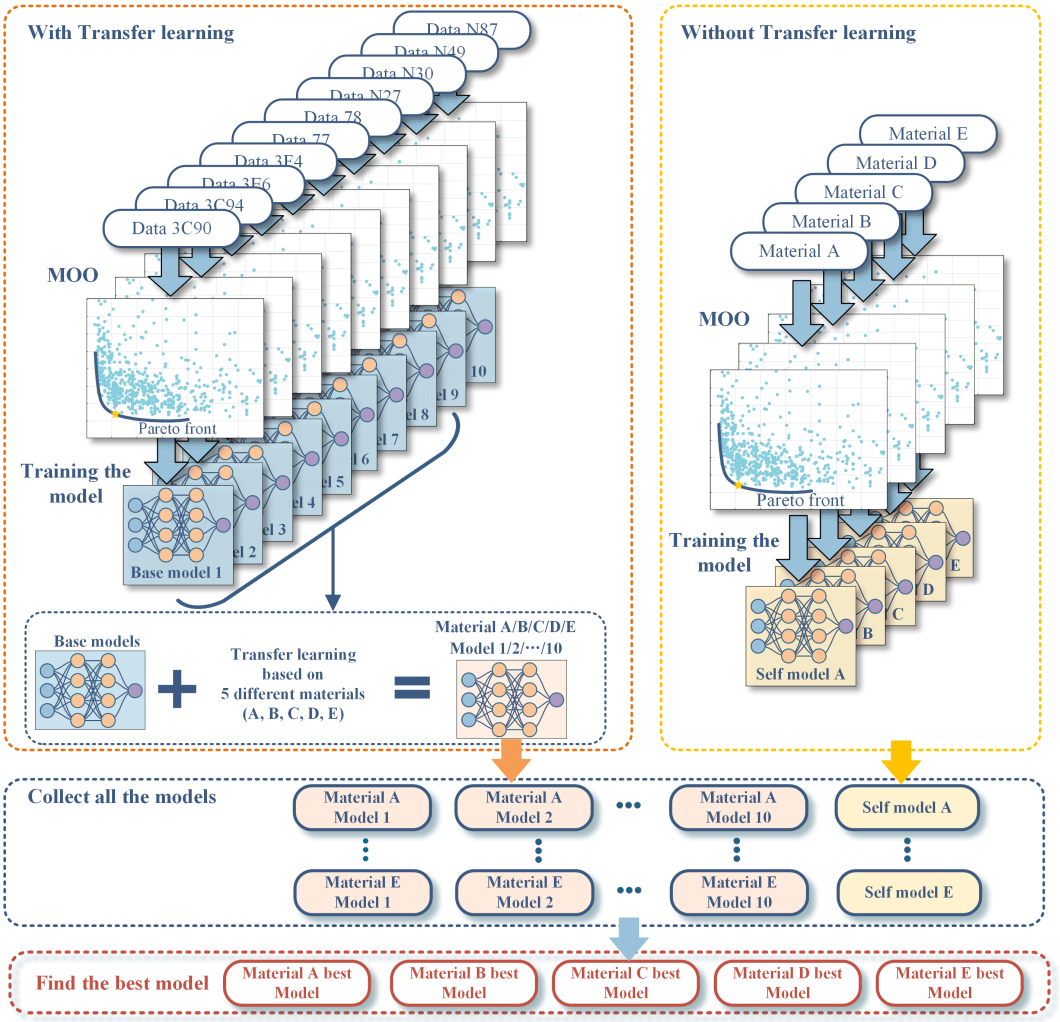


Figure 4.10: Overall model training and comparison process. Two training methods are compared. The first method optimizes and trains on ten existing materials' data before applying transfer learning to the five new materials' data, while the second directly optimizes and trains the model using data from five new materials.

include ReLU, LeakyReLU, Tanh, Sigmoid, ELU, SELU, and SiLU. These activation functions, each with distinct characteristics, play a crucial role in introducing non-linearity into the neural network, enabling it to learn complex patterns in the data [151, 152]. Possible optimizers are Adam, SGD, RMSprop, and AdamW [153]. The batch size options are set at 64, 128, or 256.

For each of the five new materials, MOO involves 500 trials, each comprising 3000 epochs. In contrast, for the ten existing materials, which have much larger datasets, MOO consists of 200 trials with 1000 epochs each. An example MOO result is presented in Fig. 4.11, where yellow and blue stars indicate the possible hyperparameter combinations on the Pareto Front. In addition, the black star represents the previous hyperparameter combinations selected based on experience, as shown in Subsection 4.2.4.

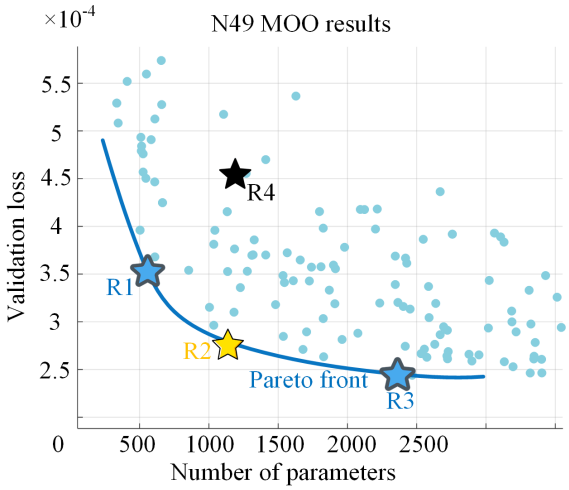


Figure 4.11: MOO result example. The depicted Pareto front represents the optimization boundary, balancing the trade-off between the number of parameters and validation loss, illustrating the most efficient solutions where neither objective can be improved without worsening the other.

The following compares these combinations and describes how to choose the most effective hyperparameter combinations on the Pareto front.

Table 4.6 summarizes these combinations' training results, and Adam is the optimizer for four cases. It is important to note that each trial during the MOO was limited to 1000 epochs. For a fair comparison of the accuracy of the four combinations in Table 4.6, the early stopping method, detailed in Subsection 4.2.3, is employed. As a result, when training these combinations, the epochs go beyond 1000.

Table 4.6 initially suggests that the R4 combination, chosen based on prior experience, does not perform as well as those on the Pareto Front. Despite R4 having more parameters than R1 and R2, it exhibits a higher average error on the test dataset than R1 and R2. This also leads to a lower transfer learning accuracy, a point further elaborated in Subsection 4.4.2. This highlights the necessity of conducting the MOO study and choosing hyperparameter combinations from the Pareto Front.

For R1, R2, and R3 on the Pareto Front, the test dataset of N49 demonstrates that

Table 4.6: Four different points on N49 MOO results shown in Fig. 9

Case	Batch size	Hidden layers neurons	No. params.	Act. Func.	N49 avg.	Material E TF avg.
R1	64	(21, 17)	560	Tanh	2.01%	2.75%
R2	128	(29, 29)	1132	Tanh	1.9%	2.49%
R3	128	(38, 19, 33, 19)	2371	SiLU	1.46%	2.35%
R4	128	(16, 32, 16)	1217	ReLU	2.2%	3%

accuracy increases with the number of parameters. However, to strike a balance between the number of parameters and accuracy, R2 is selected as the most effective choice for further transfer learning. A similar analysis approach is applied to the other materials.

A summary of all MOO results is shown in Table 4.7. The optimizer for all cases is Adam. The optimization results reveal variability in the number of neurons of hidden layers, indicating that optimal network structures differ for each material. The consistent use of the Adam optimizer across models emphasizes its effectiveness in handling the complexities of magnetic material properties. Moreover, the frequent selection of Tanh and SiLU as activation functions reflects their capability in accurately modeling the nonlinear behavior inherent in magnetic materials loss prediction.

Table 4.7: All materials optimized hyper parameters

Material	Batch size	Hidden layers neurons	No. params.	Activation function
N27	64	(30,18,31)	1419	SiLU
N30	64	(33,38,16)	2197	SiLU
N49	128	(29,29)	1132	Tanh
3F4	64	(17,30,45)	2117	Tanh
3E6	64	(18,34,14)	1295	Tanh
3C90	256	(47,35,14,9)	2705	Tanh
3C94	256	(59,27,32)	3021	Tanh
N87	64	(35,26,11)	1525	SiLU
77	128	(44,24,15,38)	2454	Tanh
78	64	(26,17,55,11)	2285	SiLU
A	64	(21,27,31)	1662	Tanh
B	64	(19,19)	552	Tanh
C	256	(36,17)	935	Tanh
D	64	(62,12,13,29)	1857	SiLU
E	64	(42,11,57)	1551	SiLU

4.4.2 Transfer Learning

The transfer learning process is shown in Fig. 4.12. This method typically begins by pre-training a neural network on a large-scale dataset. Following this, a smaller dataset is employed to fine-tune the network's parameters. This fine-tuning step is crucial, as it adjusts the model to align more closely with the specific characteristics of the smaller dataset, enhancing its performance and accuracy in tasks related to this dataset. This approach leverages the generic features learned from the large dataset, applying them effectively to the more specialized requirements of the smaller dataset.

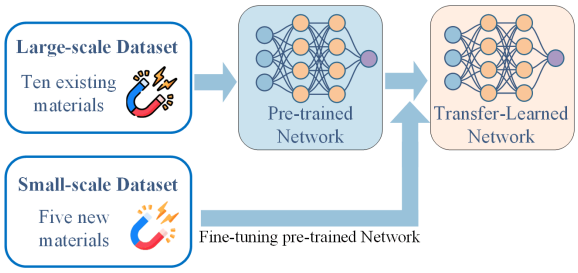


Figure 4.12: Transfer learning process for the five new materials. Once the network is pre-trained, data from the five new materials is used to fine-tune the network parameters of the pre-trained model.

Transfer learning's efficacy hinges on the relatedness of the source and target domains. A substantial discrepancy between these domains can render the transferred knowledge ineffective or even detrimental. In our study, however, the large-scale dataset features ten existing materials, while the small-scale dataset includes five new materials. Both datasets focus on magnetic materials, ensuring a significant correlation in domain-specific characteristics and thus, a high level of applicability for the transferred knowledge. This core similarity greatly reduces the chance of the performance drop-off that usually happens when there's a big gap between the two domains.

Further, to establish the pre-trained network, a critical decision is whether to independently create ten individual pre-trained models using each of the ten existing materials or construct a single pre-trained model by combining datasets from multiple materials.

As shown in Table 4.8, we have experimented with training the base model using a combined dataset of several materials (such as 3C90, N27, and 77). However, the outcomes of transfer learning with this approach did not surpass those achieved when training the base model exclusively with data from a single material (3C90). This observation leads to the speculation that new materials may exhibit closer properties to a specific existing material rather than a collective representation of several. When combining data from multiple materials, there is a potential for inter-data interference, which might hinder the model's ability to learn and predict the properties of a new material accurately. Based on this insight, we have decided to utilize a database of a single material as the starting point for transfer learning to ensure a more focused and effective model training process.

After the MOO, ten base models trained on existing materials are ready for transfer learning. New material data will be directly input into the pre-trained base model to fine-tune the parameters of the network.

A test is conducted to testify the MOO results and the transfer learning effectiveness. Based on N49 trained models, as shown in Table 4.6, the new material E data are applied

Table 4.8: Comparison of transfer learning accuracy with different base materials combinations

Base model training materials	Total number of datapoints	Transfer learning material A accuracy	
		Avg. Error	Max. Error
3C90	40713	2.16%	16.04%
3C90+N27+77	63553	2.86%	19.2%

for fine-tuning. The transfer learning results are shown in the last column of Table 4.6, which yields two key insights.

The first insight is that in the absence of MOO and when hyperparameters are chosen solely based on human experience, transfer learning is less efficient than those derived from the Pareto Front of MOO. This inefficiency is marked by an increased number of network parameters with a concurrent decrease in accuracy.

Second, it can be concluded that for the results on the Pareto Front, an increase in the number of parameters enhances the accuracy of transfer learning results. To strike an optimal balance between the number of parameters and accuracy, the knee point on the Pareto front is identified as the most effective combination of hyperparameters.

4.4.3 Results with and without Transfer Learning Comparison

Based on the overall process shown in Fig. 4.10, the results of the transfer learning approach and the normal training approach for the five new materials are presented in Table 4.9 and Table 4.10.

Table 4.9 compares the transfer learning results for the five new materials, and the best results are highlighted in green. Table 4.10 presents test dataset accuracy for the MOO models for the five new materials to compare with the transfer learning results.

As seen in Table 4.10, from an accuracy perspective, transfer learning results significantly outperform those without transfer learning, mainly due to the limited dataset available for the new materials. Although the number of parameters in transfer learning approaches is slightly higher than in normal training methods, this is not a significant concern for applying transfer learning to new materials. The rapidity of the transfer learning process, as demonstrated in our tests, enables quick adaptation to the characteristics of new materials. Consequently, despite the larger parameter size, the speed of transfer learning makes it a more practical choice. Therefore, considering both the superior accuracy and the efficiency in learning new material properties, the transfer learning models are deemed the most effective for new materials.

To ensure unbiased and reliable prediction results, the transfer learning approach, as discussed in Table 4.10, was subjected to further validation using a 10-fold cross-validation method [154, 155]. This process involves dividing the dataset into 10 equal parts, or “folds”, where each fold is used once as a validation while the remaining 9 folds are used for training. This cycle is repeated 10 times, with each fold serving as the validation set once. The accuracy metrics from each fold are then averaged to produce a composite measure of model performance. The summarized results in Table 4.12 demonstrate the robustness

Table 4.9: Transfer learning results based on MOO models of the ten existing materials. The best-performing model for each new material, after transfer learning, is highlighted in green.

Material (number of parameters)	Self-training result		Material A		Material B		Material C		Material D		Material E	
	Avg. err.	95% err.	Avg. err.	95% err.	Avg. err.	95% err.	Avg. err.	95% err.	Avg. err.	95% err.	Avg. err.	95% err.
N27 (1419)	0.75%	1.97%	2%	6.7%	0.75%	1.89%	1.39%	3.93%	3.16%	10%	2.4%	7.25%
N30 (2197)	0.41%	1.1%	2.08%	7.85%	0.7%	1.65%	1.1%	3.24%	3.7%	10%	2.28%	7%
N49 (1132)	1.9%	5.78%	2.688%	8.9%	0.79%	2.2%	1.37%	3.9%	5.11%	19%	2.49%	7%
3F4 (2117)	1.45%	3.8%	2.58%	7.8%	0.84%	2.17%	1.23%	3.4%	5.2%	15.7%	2.66%	10.9%
3E6 (1295)	0.455%	1.19%	2.25%	6.3%	0.74%	1.98%	1.23%	3.62%	4.26%	10.65%	2.77%	8%
3C90 (2705)	0.83%	2.35%	2.23%	8.1%	0.76%	1.97%	1.2%	3.78%	3.86%	10.9%	2.38%	9.24%
3C94 (3021)	0.75%	2%	3.1%	10.4%	0.75%	2.02%	1.37%	4.2%	5.9%	22.4%	2.63%	7.09%
N87 (1525)	0.74%	2%	2.54%	7.67%	0.73%	1.9%	1.19%	4%	4.6%	14.9%	2.74%	10.7%
77 (2454)	0.77%	2.1%	2.2%	6.37%	0.92%	2.48%	1.21%	3.54%	4.77%	14%	2.2%	6.4%
78 (2285)	0.72%	1.89%	2.19%	7.1%	0.69%	1.9%	1.21%	3.72%	5.23%	15.38%	2.69%	8.17%

Table 4.10: Comparison of the results with and without transfer learning for the five new materials. The training methods with and without transfer learning are corresponding to Fig. 4.10.

New Material	Results without transfer learning			Results with transfer learning			
	Number of parameters	Average error	95% error	Number of parameters	Average error	95% error	Base model
A	1662	2.18%	6.73%	1419	2%	6.7%	N27
B	552	0.9%	2.2%	2197	0.7%	1.65%	N30
C	935	1.65%	4.4%	2197	1.1%	3.24%	N30
D	1857	6.3%	21.8%	1419	3.16%	10%	N27
E	1551	2.47%	7%	2454	2.2%	6.4%	77

Table 4.11: Model performance metrics on new materials with 10-fold cross validation

New Material	Total number of data points	Number of model parameters	Avg. Error	95% Error
A	2432	1419	2.00%	6.75%
B	7400	2197	0.69%	1.81%
C	5357	2197	1.17%	3.39%
D	580	1419	3.53%	10.58%
E	2013	2454	2.12%	6.50%

of the proposed method across new materials, highlighting its effectiveness even with datasets of varying sizes.

A summary of the final model characteristics is provided in Table 4.11. The results from Table 4.11 clearly indicate that, despite the varied number of data points across new materials, the model consistently exhibits low average and 95% errors. This validates the effectiveness of the proposed MOO and transfer learning method.

Table 4.12: Cross-validation average and 95% error results for five materials.

Fold No.	Material A		Material B		Material C		Material D		Material E	
	Avg. Error	95% Error	Avg. Error	95% Error	Avg. Error	95% Error	Avg. Error	95% Error	Avg. Error	95% Error
0	1.92%	6.30%	0.64%	1.76%	1.18%	3.06%	2.90%	9.02%	2.07%	7.57%
1	1.96%	7.34%	0.72%	1.88%	1.15%	3.24%	4.19%	11.48%	2.45%	7.61%
2	2.04%	6.72%	0.58%	1.52%	1.20%	3.72%	2.68%	8.46%	1.99%	5.24%
3	1.96%	7.29%	0.71%	1.78%	1.16%	3.71%	2.75%	6.86%	2.21%	6.92%
4	2.02%	6.80%	0.77%	2.15%	1.25%	3.33%	3.76%	11.37%	1.90%	5.69%
5	2.24%	7.58%	0.75%	2.05%	1.10%	3.02%	4.10%	11.23%	2.48%	6.84%
6	2.01%	6.37%	0.59%	1.51%	1.16%	3.43%	3.16%	8.58%	1.78%	5.39%
7	1.98%	6.34%	0.69%	1.73%	1.16%	3.66%	4.27%	11.89%	1.80%	5.61%
8	1.72%	5.90%	0.70%	1.87%	1.20%	3.32%	3.84%	12.04%	2.19%	7.72%
9	2.10%	6.81%	0.70%	1.85%	1.12%	3.37%	3.67%	14.85%	2.33%	6.45%
Average	2.00%	6.75%	0.69%	1.81%	1.17%	3.39%	3.53%	10.58%	2.12%	6.50%

4.5 Conclusion

This chapter comprehensively presents a neural network-based modelling approach for accurately predicting the power loss of magnetic materials with limited data, incorporating MOO and transfer learning techniques. The fundamental neural network employed in this study is an FNN. Through a detailed comparison of various input structures and the number of harmonics, the chosen inputs are the magnitudes and frequencies of the first, second, and third order harmonics, plus temperature. Compared to other advanced methods, such as LSTM or encoder-decoder models, the proposed method achieves satisfactory accuracy with lower complexity. The model's performance is further enhanced by MOO, targeting both a reduction in the number of parameters and an increase in accuracy. Finally, a comparative analysis between results with and without transfer learning, both integrated with MOO, is conducted for new materials with limited data. The transfer learning shows a better performance with considerably lower error and marginal increase in the number of parameters.

Our proposed methodology, combining MOO and transfer learning, not only establishes a benchmark for similar studies in power electronics but also provides a versatile foundation for further extension toward practical SST applications. Future work will focus on adapting the proposed framework to medium-frequency transformer loss modeling in MW-scale SSTs, where the operating frequency is typically in the range of several hundred hertz to a few kilohertz. By generating loss data through high-fidelity 3D finite-element simulations and retraining the neural-network models via transfer learning, the approach can be tailored to the relevant frequency range and material sets, enabling accurate and computationally efficient loss prediction for SST transformer design and their integration into system-level optimization workflows.

5

Conclusion

This thesis investigates the design, control, and modeling aspects of solid-state transformers (SSTs) tailored for large-scale hydrogen electrolyzer applications, with the goal of improving system compactness, efficiency, and predictive design accuracy. It addresses three key research questions that reflect critical challenges in topology selection, control strategy development, and magnetic component modeling. The work is organized into three main chapters: Chapter 2 focuses on the comparative evaluation of SST topologies under practical constraints such as insulation distance and thermal management; Chapter 3 develops a simplified and high-performance control strategy for modular multilevel resonant converters; and Chapter 4 presents a compact data-driven framework for power loss estimation in magnetic materials under limited data scenarios. The core contributions and findings associated with each question are summarized below.

Q1 *What are the most suitable topology and operating frequency considering the size, weight, and loss performance for the solid-state transformer in MW-scale hydrogen electrolyzer applications?*

Chapter 2 presents the frequency-sweep comparison of MMC-SST, MMR-SST, and ISOP-SST in terms of loss, size, and weight. With increasing frequency, converter losses increase due to switching losses, which are pronounced for the hard-switched MMC-SST and remain much lower for the soft-switched MMR-SST and ISOP-SST, although not fully eliminated because of the DC-biased arm current in MMR-SST and the turn-off losses in ISOP-SST. Transformer losses show a non-monotonic behavior, first decreasing with reduced core size and mean length per turn, and then increasing when proximity and skin effects become dominant. Transformer size and weight decrease monotonically with frequency, while the relative contribution of the chiller becomes more significant at high frequency. Considering the combined loss, thermal, and volumetric trade-offs, the optimal operating frequencies are identified as 400 Hz for MMC-SST and 1000 Hz for both MMR-SST and ISOP-SST.

At these optimal frequencies, the MMC-SST is the bulkiest and heaviest solution and also exhibits the highest losses. In contrast, the ISOP-SST and MMR-SST show complementary advantages: the ISOP-SST achieves the lowest losses and the most compact structure, whereas the MMR-SST provides the lowest weight. These differences are mainly attributed

to the operating frequency, switching characteristics, and structural configuration. Higher frequencies in MMR-SST and ISOP-SST increase transformer copper losses due to proximity effects compared to MMC-SST, while the ISOP-SST benefits from reduced switching losses enabled by soft switching, in contrast to the MMR-SST where DC-biased arm current prevents full soft-switching operation. The compactness of the ISOP-SST is associated with its small module count and single-rack integration, whereas the use of fewer and larger transformers makes the MMR-SST more weight-efficient than topologies relying on multiple smaller units.

Q2 *How to develop a concise control strategy for the modular multilevel resonant-based solid-state transformer to improve performance while reducing control complexity?*

Chapter 3 addresses this question by focusing on the Modular Multilevel Resonant (MMR) converter and identifying the main source of control complexity in existing MMR-SST implementations. Although the topology offers soft-switching capability and modular scalability for high-power unidirectional applications such as hydrogen electrolyzers, conventional control strategies for the MMR often involve multiple control loops—such as frequency modulation, phase shift adjustment, and adjusting the number of inserted submodules—which introduce significant implementation complexity. Additionally, methods that rely on varying the switching frequency can lead to high transformer magnetizing currents, resulting in elevated core losses and increased thermal burden on the transformer.

To address these challenges, a novel continuous modulation index control strategy is proposed. This approach utilizes a double-step staircase waveform and maintains a fixed operating frequency at the resonant point, enabling the use of a transformer with higher magnetizing inductance and thereby reducing magnetizing current. The entire control scheme is centered around a single modulation variable, substantially simplifying controller parameter design and digital implementation. Moreover, by setting the phase shift angle among submodules to a small, fixed value, the proposed method minimizes resonant current total harmonic distortion (THDi), especially under rated power conditions. The simulation and scaled-down experimental validation demonstrate that the proposed strategy achieves improved overall efficiency, fast dynamic response, and lower power losses compared to state-of-the-art control methods. These results highlight the method's potential for practical deployment in medium-voltage SST systems for hydrogen electrolyzer applications.

Q3 *How to push forward loss estimation accuracy of magnetic components with data-driven approaches?*

Chapter 4 explores this question by investigating neural network–based methods for estimating the power loss of magnetic components, particularly under conditions of limited data availability. Traditional approaches—such as the Steinmetz Equation and its extensions (iGSE, i2GSE)—remain dominant in magnetic loss modeling but suffer from limited accuracy and generalization, especially across varying waveforms and material types. Motivated by the MagNet Challenge 2023 and the growing need for accurate, low-complexity modeling tools, this work proposes a compact, data-driven framework that leverages neural networks to directly predict core losses using waveform characteristics. A key innovation lies in extracting harmonic information from the flux density waveform via Fast Fourier Transform (FFT), and using the first few dominant harmonics as structured inputs to a feedforward

neural network (FNN). Compared to more complex models such as LSTM or encoder-decoder networks, the proposed FFT+FNN structure achieves comparable or better accuracy with significantly reduced training time and model complexity.

Beyond the core architecture, the model design is further enhanced by integrating Multi-Objective Optimization (MOO), which systematically explores the trade-off between prediction accuracy and neural network size. Using the Optuna optimization framework, Pareto-optimal solutions are identified to guide hyperparameter tuning in a principled manner. Additionally, transfer learning is employed to improve prediction performance on new magnetic materials with limited data, reusing the knowledge learned from well-characterized materials. This approach leads to better generalization and lower error while incurring only a marginal increase in model complexity.

Overall, the proposed FFT+FNN method—combined with MOO and transfer learning—offers a robust, computationally efficient, and practical solution for loss modeling in power magnetics. It not only demonstrates strong performance on benchmark datasets but also serves as a scalable template for other power electronics applications where accurate prediction and limited data remain a challenge. For example, the framework is applicable to medium-frequency transformer core loss modeling in MW-scale SSTs. By combining high-fidelity simulation data with transfer learning, the proposed approach can be adapted to the relevant frequency range and material set, enabling accurate and computationally efficient loss estimation for system-level design and optimization.

Recommendations for Future Work

In summary, this thesis addresses the comparative evaluation of candidate SST topologies, the development of a simplified control strategy for MMR-SST, and a data-driven methodology for magnetic loss modeling. Nevertheless, several aspects remain open for further investigation, and the following directions are identified as promising topics for future work.

First, future work can extend the topology comparison in Chapter 2 by incorporating cost as an additional key metric. While the present study focuses on efficiency, size, and weight, the practical feasibility of the candidate topologies also strongly depends on their overall cost. By establishing cost models for key components, including power semiconductor devices, medium-frequency transformers, cooling systems, and auxiliary equipment, the existing design and evaluation framework can be further developed into a more comprehensive assessment.

In addition, another promising direction is the investigation of fully modular ISOP-based SST architectures, in which cascaded power modules are directly connected to the medium-voltage grid to achieve the required voltage and power levels, similar to recent medium-voltage data-center power supply concepts that have attracted increasing attention. Compared with the 12-pulse diode rectifier topology employing a centralized phase-shifting autotransformer, such fully modular systems can avoid single-point-of-failure components and inherently provide redundancy, scalability, and ease of module replacement. A systematic comparison in terms of efficiency, size, weight, and cost would help clarify whether this architecture offers benefits for large-scale electrolyzer plants.

From a control perspective, future work may also investigate the application of the extended describing function method to derive analytical small-signal models for the MMR-

based SST. Although the simulation-based small-signal perturbation approach adopted in Chapter 3 enables accurate extraction of the frequency response and leads to stable and fast PI controller designs, it relies on repeated time-domain simulations for each operating point and parameter set. By contrast, an analytically derived transfer function based on the extended describing function framework would allow a more systematic insight into the dynamic behavior of the converter and facilitate controller design and robustness analysis. Moreover, such an analytical model would enable efficient evaluation of the impact of system parameter variations, without the need for time-consuming re-identification of the small-signal response through perturbation simulations.

Finally, the data-driven magnetic loss modeling framework developed in Chapter 4 is based on the MagNet Challenge dataset, which covers a frequency range from 50 kHz to 800 kHz, whereas the operating frequency of medium-voltage, MW-scale SSTs is typically in the order of several hundred hertz to a few kilohertz. To adapt the neural-network models to the frequency range relevant for the target SST applications, high-fidelity 3D finite-element simulations can be used to generate loss data, which can then be combined with transfer learning to retrain the proposed models, thereby enabling fast and flexible development of accurate loss models without relying on extensive experimental characterization. This would further allow accurate and computationally efficient loss prediction for practical SST transformer designs and facilitate their integration into system-level optimization workflows.

Bibliography

References

[1] International Energy Agency, "Global Energy Review 2025." https://www.iea.org/reports/global-energy-review-2025, 2025. IEA, Paris. Licence: CC BY 4.0.

[2] Z. Allam, S. E. Bibri, and S. A. Sharpe, "The Rising Impacts of the COVID-19 Pandemic and the Russia–Ukraine War: Energy Transition, Climate Justice, Global Inequality, and Supply Chain Disruption," *Resources*, vol. 11, no. 11, 2022.

[3] D. Parra, L. Valverde, F. J. Pino, and M. K. Patel, "A review on the role, cost and value of hydrogen energy systems for deep decarbonisation," *Renewable and Sustainable Energy Reviews*, vol. 101, pp. 279–294, 2019.

[4] J. Yap and B. McLellan, "A Historical Analysis of Hydrogen Economy Research, Development, and Expectations, 1972 to 2020," *Environments*, vol. 10, no. 1, 2023.

[5] P. A. Østergaard, N. Duic, Y. Noorollahi, H. Mikulcic, and S. Kalogirou, "Sustainable development using renewable energy technology," *Renewable Energy*, vol. 146, pp. 2430–2437, 2020.

[6] Wikipedia contributors, "Hydrogen production." https://en.wikipedia.org/wiki/Hydrogen_production, 2025. Accessed: 2025-07-29.

[7] J. Bartlett and A. Krupnick, "Investment Tax Credits and Hydrogen Storage." https://www.rff.org/publications/issue-briefs/investment-tax-credits-hydrogen-storage/, 2024. Accessed: August 4, 2025.

[8] International Renewable Energy Agency (IRENA), "Green Hydrogen: A Guide to Policy Making," 2020. Accessed: August 4, 2025.

[9] TNO, "CO2 Reduction in the Netherlands: Measures and Innovations," 2025. Accessed: 2025-08-06.

[10] "Flexible Offshore Wind Hydrogen Power Plant Module (FlexH2)." https://growâĂŚflexh2.nl/, 2025. Project duration: April 2022–March 2026; supported by Dutch Ministry of Energy and Climate (MOOI grant 52103). Led by Shell, TU Delft contributes solid-state transformer WP.

[11] T. Guillod, D. Rothmund, and J. W. Kolar, "10kV SiC MOSFETs for Solid-State Transformers: Opportunities and Challenges." Tutorial, X-Power Electronics Conference, May 2019.

[12] B. Engel, M. Victor, G. Bachmann, and A. Falk, "15 kV/16.7 Hz energy supply system with medium frequency transformer and 6.5 kV IGBTs in resonant operation," in *Proc. EPE*, pp. 2–4, 2003.

[13] J. Taufiq, "Power Electronics Technologies for Railway Vehicles," in *2007 Power Conversion Conference - Nagoya*, pp. 1388–1393, 2007.

[14] M. Glinka, "Prototype of multiphase modular-multilevel-converter with 2 MW power rating and 17-level-output-voltage," in *2004 IEEE 35th Annual Power Electronics Specialists Conference (IEEE Cat. No.04CH37551)*, vol. 4, pp. 2572–2576 Vol.4, 2004.

[15] M. Steiner and H. Reinold, "Medium frequency topology in railway applications," in *2007 European Conference on Power Electronics and Applications*, pp. 1–10, 2007.

[16] N. Hugo, P. Stefanutti, M. Pellerin, and A. Akdag, "Power electronics traction transformer," in *2007 European Conference on Power Electronics and Applications*, pp. 1–10, 2007.

[17] J. Clare, "Advanced power converters for universal and flexible power management in future electricity networks," in *2009 13th European Conference on Power Electronics and Applications*, pp. 1–29, 2009.

[18] T. Kjellqvist, S. Ostlund, S. Norrga, and K. Ilves, "Thermal evaluation of a medium frequency transformer in a line side conversion system," in *2009 13th European Conference on Power Electronics and Applications*, pp. 1–10, 2009.

[19] M. K. Das, C. Capell, D. E. Grider, S. Leslie, J. Ostop, R. Raju, M. Schutten, J. Nasadoski, and A. Hefner, "10 kV, 120 A SiC half H-bridge power MOSFET modules suitable for high frequency, medium voltage applications," in *2011 IEEE Energy Conversion Congress and Exposition*, pp. 2689–2692, 2011.

[20] N. Soltau, R. U. Lenke, and R. W. de Doncker, *High-Power DC-DC Converter / Nils Soltau, Robert Ulrich Lenke, Rik W. de Doncker; First Edition*, vol. 5,5 of *E.ON Energy Research Center series.* Aachen: E.ON Energy Research Center, RWTH Aachen Univ., 2013. Zweitveröffentlicht auf dem Publikationsserver der RWTH Aachen University 2016.

[21] C. Zhao, D. Dujic, A. Mester, J. K. Steinke, M. Weiss, S. Lewdeni-Schmid, T. Chaudhuri, and P. Stefanutti, "Power Electronic Traction Transformer—Medium Voltage Prototype," *IEEE Transactions on Industrial Electronics*, vol. 61, no. 7, pp. 3257–3268, 2014.

[22] C. Zhu, "High-Efficiency, Medium-Voltage-Input, Solid-State-Transformer-Based 400-kW/1000V/400A Extreme Fast Charger for Electric Vehicles." Technical Report, Delta Electronics (Americas) Ltd., Livonia, MI, July 2023. Prepared for U.S. Department of Energy. DOI: 10.2172/1987553.

[23] C. Zhu, "High-Efficiency, Medium-Voltage Input, Solid-State, Transformer-Based 400-kW/1000-V/400-A Extreme Fast Charger for Electric Vehicles." Technical Report,

Delta Electronics (Americas) Ltd., Fremont, CA, June 2021. Prepared for the U.S. Department of Energy, Office of Energy Efficiency and Renewable Energy. ELT241.

[24] J. E. Huber, J. Böhler, D. Rothmund, and J. W. Kolar, "Analysis and cell-level experimental verification of a 25 kW all-SiC isolated front end 6.6 kV/400 V AC-DC solid-state transformer," *CPSS Transactions on Power Electronics and Applications*, vol. 2, no. 2, pp. 140–148, 2017.

[25] D. Wang, J. Tian, C. Mao, J. Lu, Y. Duan, J. Qiu, and H. Cai, "A 10-kV/400-V 500-kVA Electronic Power Transformer," *IEEE Transactions on Industrial Electronics*, vol. 63, no. 11, pp. 6653–6663, 2016.

[26] H.-J. Yun, D.-K. Jeong, H.-S. Kim, M. Kim, J.-W. Baek, J.-Y. Kim, and H.-J. Kim, "Implementation of a single-phase SST for the interface between a 13.2 kV MVAC network and a 750 V bipolar DC distribution," *Electronics*, vol. 7, no. 5, p. 62, 2018.

[27] European Commission, "MESHPOWER: Modular and Efficient Solid-state High power converters for POweR grid and railway applications." https://cordis.europa.eu/project/id/616344, 2014. Accessed: 2025-07-29.

[28] J. W. Kolar, "Solid State Transformer (SST) Applications-A Glimpse Into the Future," in *2nd International Conference on Smart Grid and Renewable Energy (SGRE 2019)*, 2019.

[29] K. Li, W. Wen, Z. Zhao, L. Yuan, W. Cai, X. Mo, and C. Gao, "Design and Implementation of Four-Port Megawatt-Level High-Frequency-Bus Based Power Electronic Transformer," *IEEE Transactions on Power Electronics*, vol. 36, no. 6, pp. 6429–6442, 2021.

[30] Q. Fu, B. Li, X. Zhao, S. Mao, D. Xu, and L. Han, "Voltage Balancing Methods for Inner and Outer Switches of Three-level Resonant DC-DC Converter for Solid State Transformers," in *2020 IEEE 9th International Power Electronics and Motion Control Conference (IPEMC2020-ECCE Asia)*, pp. 517–522, 2020.

[31] M. Adamowicz and J. Szewczyk, "SiC-Based Power Electronic Traction Transformer (PETT) for 3 kV DC Rail Traction," *Energies*, vol. 13, no. 21, 2020.

[32] T. Liu, X. Yang, W. Chen, Y. Xuan, Y. Li, L. Huang, and X. Hao, "High-Efficiency Control Strategy for 10-kV/1-MW Solid-State Transformer in PV Application," *IEEE Transactions on Power Electronics*, vol. 35, no. 11, pp. 11770–11782, 2020.

[33] A. Makkieh, G. Burt, R. P. Alzola, G. Jambrich, N. Fuchs, A. Kazerooni, A. Allais, C. Preve, E. Bećirović, J. Yu, J. Vočko, J. Dai, J. Cho, J. Kim, K.-D. Haim, K. Lorenzo, M.-R. Haghifam, M. Rose, M. M. Chowdhury, M. Bartonek, N. Murdoch, R. Montano, R. Rabinovici, R. Braunstein, R. Majumder, S. Rupp, U. Schichler, V. Kleftakis, Y. yuan Xie, Y. Kamelia, and Z. Lin, "DC Networks on the Distribution Level – New Trend or Vision?," technical report, CIRED Working Group, sep 2021.

[34] L. Y. W. P. Y. Y. Gao Fanqiang, Li Zixin, "10kV-3MVA Four-Port Power Electronic Transformer for AC-DC Hybrid Power Distribution Applications," *Transactions of China Electrotechnical Society*, vol. 36, no. 16, p. 3331, 2021.

[35] G. Fortes, P. Ladoux, J. Fabre, and D. Flumian, "Characterization of a 300 kW Isolated DCDC Converter using 3.3 kV SiC-MOSFETs," in *PCIM Europe digital days 2021; International Exhibition and Conference for Power Electronics, Intelligent Motion, Renewable Energy and Energy Management*, pp. 1–8, 2021.

[36] Y. Liu, X. Liu, and Z. Wang, "Topology and start strategy for DC-DC transformer based on voltage balancing circuit," in *2023 IEEE International Conference on Control, Electronics and Computer Technology (ICCECT)*, pp. 313–319, 2023.

[37] ScottishPower Energy Networks, "LV Engine Project." https://www.spenergynetworks.co.uk/pages/lv_engine.aspx, 2022. Accessed: 2025-07-29.

[38] P. Czyz, T. Guillod, D. Zhang, F. Krismer, J. Huber, R. Färber, C. M. Franck, and J. W. Kolar, "Analysis of the Performance Limits of 166 kW/7 kV Air- and Magnetic-Core Medium-Voltage Medium-Frequency Transformers for 1:1-DCX Applications," *IEEE Journal of Emerging and Selected Topics in Power Electronics*, vol. 10, no. 3, pp. 2989–3012, 2022.

[39] A. Anurag, S. Acharya, S. Bhattacharya, T. R. Weatherford, and A. A. Parker, "A Gen-3 10-kV SiC MOSFET-Based Medium-Voltage Three-Phase Dual Active Bridge Converter Enabling a Mobile Utility Support Equipment Solid State Transformer," *IEEE Journal of Emerging and Selected Topics in Power Electronics*, vol. 10, no. 2, pp. 1519–1536, 2022.

[40] European Commission, "TIGON: Towards Intelligent DC-based hybrid Grids Optimizing the Network performance." https://cordis.europa.eu/project/id/957769, 2020. Accessed: 2025-07-29.

[41] J. Yu, C. Luo, J. Duan, C. Wang, R. Lu, A. Trujillo, C. Li, and W. Li, "Design and Validation of A 2MW 10KV Medium-voltage Solid State Transformer," in *2024 IEEE Energy Conversion Congress and Exposition (ECCE)*, pp. 1426–1433, 2024.

[42] D. Dujic and M. Mogorovic, "High Power MFT Design Optimization," in *19th International Symposium on Power Electronics (Ee 2017)*, (Novi Sad, Serbia), École Polytechnique Fédérale de Lausanne, Power Electronics Laboratory, October 19–21 2017. Presentation.

[43] B. L. Nguyen, M. Panwar, R. Hovsapian, K. Nagasawa, and T. V. Vu, "Power Converter Topologies for Electrolyzer Applications to Enable Electric Grid Services," in *IECON 2021–47th Annual Conference of the IEEE Industrial Electronics Society*, pp. 1–6, IEEE.

[44] R. Mirzadarani, M. G. Niasar, Z. Li, Z. Qin, P. Vaessen, P. Bauer, and L. V. Lieshout, "Three-Phase Medium-Voltage Medium-Frequency Transformer for SST in Green Hydrogen Production," in *IECON 2023- 49th Annual Conference of the IEEE Industrial Electronics Society*, pp. 1–6.

[45] B. Yodwong, D. Guilbert, M. Phattanasak, W. Kaewmanee, M. Hinaje, and G. Vitale, "AC-DC converters for electrolyzer applications: State of the art and future challenges," *Electronics*, vol. 9, no. 6, p. 912, 2020.

[46] E. S. Lee, J. H. Park, M. Y. Kim, and J. S. Lee, "High Efficiency Module Design of Solid-State Transformers for Railway Vehicles," *IEEE Transactions on Transportation Electrification*, 2021.

[47] P. Kjaer, Y. Chen, and C. Dincan, "DC collection: Wind power plant with medium voltage dc power collection network," in *ECPE Workshop Smart Transf. Traction Future Grid Appl.*

[48] I. Syed and V. Khadkikar, "Replacing the grid interface transformer in wind energy conversion system with solid-state transformer," *IEEE Transactions on Power Systems*, vol. 32, no. 3, pp. 2152–2160, 2016.

[49] N. Doerry and K. McCoy, "Next generation integrated power system: NGIPS technology development roadmap," *Naval Sea Systems Command*, 2007.

[50] Y. Du, S. Baek, S. Bhattacharya, and A. Q. Huang, "High-voltage high-frequency transformer design for a 7.2 kV to 120V/240V 20kVA solid state transformer," in *IECON 2010-36th Annual Conference on IEEE Industrial Electronics Society*, pp. 493–498, IEEE.

[51] T. Zhao, G. Wang, S. Bhattacharya, and A. Q. Huang, "Voltage and Power Balance Control for a Cascaded H-Bridge Converter-Based Solid-State Transformer," *IEEE Transactions on Power Electronics*, vol. 28, no. 4, pp. 1523–1532, 2013.

[52] C. Lu, W. Hu, H. Wu, and F. C. Lee, "Quasi-Two-Level Bridgeless PFC Rectifier for Cascaded Unidirectional Solid State Transformer," *IEEE Transactions on Power Electronics*, vol. 36, no. 10, pp. 12033–12044, 2021.

[53] Z. Pei, D. Kong, C. Liu, C. Liu, D. Guo, D. Zhu, Y. Sun, and M. L. Heldwein, "Hybrid Isolated Modular Multilevel Converter Based Solid-State Transformer Topology With Simplified Power Conversion Process and Uneven Voltage Ratio," *IEEE Transactions on Power Electronics*, vol. 38, no. 10, pp. 12757–12773, 2023.

[54] Z. Bu, W. Zhao, M. Zhang, J. Teng, X. Li, and X. Sun, "Dynamic Performance Evaluation and Optimization of Common HFAC Bus Lightweight MMC-SST," *IEEE Transactions on Power Electronics*, pp. 1–16, 2023.

[55] G. Zheng, Y. Chen, and Y. Kang, "A Modular Multilevel Converter (MMC) Based Solid-State Transformer (SST) Topology With Simplified Energy Conversion Process and Magnetic Integration," *IEEE Transactions on Industrial Electronics*, vol. 68, no. 9, pp. 7725–7735, 2021.

[56] Z. Li, Z. Qin, R. Mirzadarani, M. G. Niasar, M. Itraj, L. V. Lieshout, and P. Bauer, "Comparison of Modular Multilevel Converter Based Solid State Transformer for AC/DC Application," in *IECON 2023- 49th Annual Conference of the IEEE Industrial Electronics Society*, pp. 1–6.

[57] Z. Lu, L. Lin, X. Wang, and C. Xu, "LLC-MMC Resonant DC-DC Converter: Modulation Method and Capacitor Voltage Balance Control Strategy," in *2020 IEEE Applied Power Electronics Conference and Exposition (APEC)*, pp. 2056–2061.

[58] H. Saeedifard and A. Yazdani, "Modeling and Soft-Switching Operation of an Isolated Modular-Multilevel-Converter-Based DC-DC Converter," in *2022 IEEE Energy Conversion Congress and Exposition (ECCE)*, pp. 1–8.

[59] S. Belkhode, P. Rao, A. Shukla, and S. Doolla, "Comparative Evaluation of Silicon and Silicon-Carbide Device-Based MMC and NPC Converter for Medium-Voltage Applications," *IEEE Journal of Emerging and Selected Topics in Power Electronics*, vol. 10, no. 1, pp. 856–867, 2022.

[60] G. Abeynayake, G. Li, T. Joseph, J. Liang, and W. Ming, "Reliability and Cost-Oriented Analysis, Comparison and Selection of Multi-Level MVdc Converters," *IEEE Transactions on Power Delivery*, vol. 36, no. 6, pp. 3945–3955, 2021.

[61] S. Shao, Y. Li, J. Sheng, C. Li, W. Li, J. Zhang, and X. He, "A Modular Multilevel Resonant DC–DC Converter," *IEEE Transactions on Power Electronics*, vol. 35, no. 8, pp. 7921–7932, 2020.

[62] Z. Yi, S. Shaolei, DianguoXu, and Y. Rongfeng, "Comparison and review of DC transformer topologies for HVDC and DC grids," in *2016 IEEE 8th International Power Electronics and Motion Control Conference (IPEMC-ECCE Asia)*, pp. 3336–3343.

[63] L. Camurca, T. Pereira, F. Hoffmann, and M. Liserre, "Analysis, Limitations, and Opportunities of Modular Multilevel Converter-Based Architectures in Fast Charging Stations Infrastructures," *IEEE Transactions on Power Electronics*, vol. 37, no. 9, pp. 10747–10760, 2022.

[64] A. Marzoughi, R. Burgos, D. Boroyevich, and Y. Xue, "Design and Comparison of Cascaded H-Bridge, Modular Multilevel Converter, and 5-L Active Neutral Point Clamped Topologies for Motor Drive Applications," *IEEE Transactions on Industry Applications*, vol. 54, no. 2, pp. 1404–1413, 2018.

[65] B. Zhao, Q. Song, J. Li, X. Xu, and W. Liu, "Comparative Analysis of Multilevel-High-Frequency-Link and Multilevel-DC-Link DC–DC Transformers Based on MMC and Dual-Active Bridge for MVDC Application," *IEEE Transactions on Power Electronics*, vol. 33, no. 3, pp. 2035–2049, 2018.

[66] Infineon, "Bipolar Semiconductor-Technical Information." https://www.infineon.com/dgdl/Infineon-AN20012_01_Bipolar_Technical_Information-ApplicationNotes-v01_00-EN.pdf?fileId=db3a304412b407950112b40ec42b126a, 2012. Accessed: 2025-06-20.

[67] P. In Gyu and K. Seon Ik, "Modeling and analysis of multi-interphase transformers for connecting power converters in parallel," in *PESC97. Record 28th Annual IEEE Power Electronics Specialists Conference. Formerly Power Conditioning Specialists Conference 1970-71. Power Processing and Electronic Specialists Conference 1972*, vol. 2, pp. 1164–1170 vol.2.

[68] T. E. Slettbakk, *Development of a Power Quality Conditioning System for Particle Accelerators*. Thesis, 2018.

[69] K. Sharifabadi, L. Harnefors, H. P. Nee, S. Norrga, and Teodorescu, *Design, Control and Application of Modular Multilevel Converters for HVDC Transmission Systems*. 2016.

[70] International Electrotechnical Commission, "IEC 60076-1: Power Transformers – Part 1: General." https://webstore.iec.ch/en/publication/588, 2011. Accessed: 2025-06-20.

[71] ELECTRONICON, "57 / E59 / SR17 AC and DC Capacitors with Large Capacitances." https://www.electronicon.com/fileadmin/inhalte/PDF-Dateien/Kataloge_und_Broschueren/200.003-020070_E56-SR17.pdf, 2022. Accessed: 2025-06-20.

[72] Hitachi Energy, "Dry Capacitors for Voltage Source Converters." https://www.hitachienergy.com/products-and-solutions/capacitors-and-filters/high-voltage-capacitors-and-filters/capacitor-units/dc-dry-type-capacitors-drydcap, 2022. Accessed: 2025-06-20.

[73] G. P. Lourduraj, *Feasibility study of oil immersed power electronic based high voltage test source for onsite testing purpose*. Thesis, 2019.

[74] PPC Insulators, "Solid Core Post Insulators BIL 60–95 kV." https://ppcinsulators.com/, 2024. Accessed: 2025-06-20.

[75] M. J. H. P. Franklin, *The J P transformer book : a practical technology of the power transformer*. Burlington, MA: Newnes, 2007.

[76] J. H. Harlow, *Electric Power Transformer Engineering*. Baton Rouge, UNITED STATES: Taylor Francis Group, 2012.

[77] Metglas, "Magnetic Materials." https://metglas.com/magnetic-materials/, 2023. Accessed: Dec. 9, 2023.

[78] S. Meier, T. Kjellqvist, S. Norrga, and H. P. Nee, "Design considerations for medium-frequency power transformers in offshore wind farms," in *2009 13th European Conference on Power Electronics and Applications*, pp. 1–12.

[79] C. Yang, H. Hu, P. Tian, J. Shi, Z. Wang, and C. Zhang, "Study on the Loss Characteristics of Dry-Type Power Transformers Considering Stray Losses," in *2023 IEEE 4th China International Youth Conference On Electrical Engineering (CIYCEE)*, pp. 1–5.

[80] B. Liu, Y. Takahashi, K. Fujiwara, and S. Imamori, "Stray Loss Evaluation of Power Transformers Using Simplified Air-Core Model With Tank and Frame," *IEEE Transactions on Magnetics*, vol. 59, no. 11, pp. 1–6, 2023.

[81] K. H. Park, H. J. Lee, and S. C. Hahn, "Finite-Element Modeling and Experimental Verification of Stray-Loss Reduction in Power Transformer Tank With Wall Shunt," *IEEE Transactions on Magnetics*, vol. 55, no. 12, pp. 1–4, 2019.

[82] M. A. P. G. J. Duc, B. Poulin, "Loss prophet, Predicting stray losses in power transformers and optimization of tank shielding using FEM," report, ABB, 2016.

[83] X. M. Lopez-Fernandez and L. A. Alvarez-Gomez, "Calculation of stray losses in continuously transposed conductor cable transformer windings by multi-slice methodology," *International Journal of Electrical Power Energy Systems*, vol. 111, pp. 25–33, 2019.

[84] International Electrotechnical Commission, "IEC 60076-2: Power Transformers – Part 2: Temperature Rise for Liquid-Immersed Transformers." https://webstore.iec.ch/en/publication/599, 2011. Accessed: 2025-06-20.

[85] P. T. F. D. M. S. Robert M. Del Vecchio, Bertrand Poulin and R. Ahuja, *Transformer Design Principles*. New York, NY: CRC Press, 3rd ed., 2018.

[86] L. W. Pierce, "An investigation of the thermal performance of an oil filled transformer winding," *IEEE Transactions on Power Delivery*, vol. 7, no. 3, pp. 1347–1358, 1992.

[87] D. S. Lehtonen and M., "Dynamic thermal modeling of power transformers: further Development-part II," *IEEE Transactions on Power Delivery*, vol. 21, no. 4, pp. 1971–1980, 2006.

[88] International Electrotechnical Commission, "IEC 60156: Insulating Liquids – Determination of the Breakdown Voltage at Power Frequency – Test Method." https://webstore.iec.ch/en/publication/66317, 2018. Accessed: 2025-06-20.

[89] F. H. Kreuger, *Industrial high voltage / [Vol. III], Industrial high DC voltage : 1. Fields, 2. Breakdowns 3. Tests*. Delft: Delft University Press, 1995.

[90] International Electrotechnical Commission, "IEC 60076-3: Power Transformers – Part 3: Insulation Levels, Dielectric Tests and External Clearances in Air." https://webstore.iec.ch/en/publication/62880, 2021. Accessed: 2025-06-20.

[91] Delta-Temp, "Reliable Chillers for Industrial Air Conditioning and Process Cooling." https://delta-temp.com/en_int/cooling-rental/mobile-chiller-rental/, 2023. Accessed: 2025-06-20.

[92] K. H. Chen, J. Y. Lin, Y. F. Lin, Y. C. Chang, and H. J. Chiu, "Design of Three Phase Wye-Delta LLC Converter with Time Domain Analysis," in *2019 10th International Conference on Power Electronics and ECCE Asia (ICPE 2019 - ECCE Asia)*, pp. 1–6.

[93] H. Huang, "Designing an LLC resonant half-bridge power converter," in *2010 Texas Instruments Power Supply Design Seminar, SEM1900, Topic*, vol. 3, pp. 2010–2011, Texas Instruments Incorporated Dallas, TX, USA.

[94] Y. Nakakohara, H. Otake, T. M. Evans, T. Yoshida, M. Tsuruya, and K. Nakahara, "Three-Phase LLC Series Resonant DC/DC Converter Using SiC MOSFETs to Realize High-Voltage and High-Frequency Operation," *IEEE Transactions on Industrial Electronics*, vol. 63, no. 4, pp. 2103–2110, 2016.

[95] K. Murata and F. Kurokawa, "An Interleaved PFM LLC Resonant Converter With Phase-Shift Compensation," *IEEE Transactions on Power Electronics*, vol. 31, no. 3, pp. 2264–2272, 2016.

[96] zez silko, "INDUCTION HEATING CAPACITORS," report, 2023.

[97] L. Gong, Y. Peng, C. Cui, J. Chen, L. Jiang, X. Fang, J. Wang, J. Xu, and Y. Wang, "An Ultrafast and Wide-Safe-Range Start-Up Method of DAB Converters With Straightforward Frequency-Phase Closed-Loop Control," *IEEE Transactions on Power Electronics*, vol. 39, no. 11, pp. 14161–14166, 2024.

[98] L. Gong, Y. Peng, C. Cui, J. Chen, L. Jiang, J. Xu, X. Fang, and Y. Wang, "A Hybrid Phase-Frequency Control of Dual Active Bridge Converters for Hold-Up Time Extension in More Electric Aircrafts Applications," *IEEE Transactions on Power Electronics*, vol. 39, no. 11, pp. 14135–14141, 2024.

[99] I. A. Gowaid, G. P. Adam, S. Ahmed, D. Holliday, and B. W. Williams, "Analysis and Design of a Modular Multilevel Converter With Trapezoidal Modulation for Medium and High Voltage DC-DC Transformers," *IEEE Transactions on Power Electronics*, vol. 30, no. 10, pp. 5439–5457, 2015.

[100] W. Cui, S. Shao, T. Wu, W. Chen, and J. Zhang, "A Bidirectional Modular Multilevel Resonant DC–DC Converter for Wide Voltage Range Medium-Voltage Power Conversion," *IEEE Transactions on Power Electronics*, vol. 38, no. 10, pp. 12743–12756, 2023.

[101] J. Sheng, X. Xiang, B. Li, R. Lu, C. Li, X. Zhang, W. Li, and X. He, "High-Efficient Operation for Modular Multilevel Resonant DC–DC Converters in Medium Voltage Applications With Wide Input Range and Wide Load Condition," *IEEE Transactions on Power Electronics*, vol. 38, no. 10, pp. 12180–12194, 2023.

[102] J. Pan and M. Wang, "An improved quasi-square-wave modulation suitable for isolated modular multilevel DC-DC converter," *CSEE Journal of Power and Energy Systems*, pp. 1–13, 2022.

[103] S. P. Martin, X. Dong, and H. Li, "Model Development and Predictive Control of a Low-Inertia DC Solid State Transformer (SST)," *IEEE Journal of Emerging and Selected Topics in Power Electronics*, 2022.

[104] S. Yin, Z. Zeng, S. Debnath, and M. Saeedifard, "Modeling and ZVS Operation of the Isolated Modular Multilevel DC–DC Converter With a Unified Trapezoidal Wave Modulation," *IEEE Transactions on Power Electronics*, vol. PP, pp. 1–17, 2024.

[105] J. Sheng, C. Chen, R. Lu, C. Li, X. Xiang, W. Li, and X. He, "Control Optimization of Modular Multilevel Resonant DC Converters for Wide-Input-Range MVdc to LVdc Applications," *IEEE Transactions on Power Electronics*, vol. 37, no. 5, pp. 5284–5298, 2022.

[106] Z. Li, Z. Qin, R. Mirzadarani, M. G. Niasar, M. Itraj, L. Van Lieshout, and P. Bauer, "Comparison of Modular Multilevel Converter Based Solid State Transformer for AC/DC Application," in *IECON 2023-49th Annual Conference of the IEEE Industrial Electronics Society*, pp. 1–6, IEEE.

[107] J. Cao, X. Zhang, P. Rao, S. Zhou, F. Zhou, and Q. Zhang, "Design of Three-Phase Delta-Delta LLC Resonant Converter," in *2020 IEEE Vehicle Power and Propulsion Conference (VPPC)*, pp. 1–5.

[108] S. Shao, M. Jiang, J. Zhang, and X. Wu, "A Capacitor Voltage Balancing Method for a Modular Multilevel DC Transformer for DC Distribution System,"

[109] B. Yang, *Topology investigation of front end DC/DC converter for distributed power system.* PhD thesis, Virginia Polytechnic Institute and State University, Blacksburg, Virginia, USA, September 2003.

[110] S. Tian, *Equivalent Circuit Model of High Frequency Pulse- Width-Modulation (PWM) and Resonant Converters.* PhD thesis, Virginia Polytechnic Institute and State University, 08 2015.

[111] J. Wang, D. Fu, Z. Yang, and W. Pei, "Three-phase llc small-signal modeling and fast-response control design," in *2022 IEEE International Power Electronics and Application Conference and Exposition (PEAC)*, pp. 1234–1239, 2022.

[112] C.-H. Chang, E.-C. Chang, C.-A. Cheng, H.-L. Cheng, and S.-C. Lin, "Small signal modeling of llc resonant converters based on extended describing function," in *2012 International Symposium on Computer, Consumer and Control*, pp. 365–368, 2012.

[113] M. Iurich, S. Calligaro, and R. Petrella, "Accurate and computationally-optimized small-signal model identification of llc resonant converter based on machine learning techniques," in *2022 IEEE Energy Conversion Congress and Exposition (ECCE)*, pp. 1–6, 2022.

[114] Y.-H. Hsieh and F. C. Lee, "Accurate small-signal model for llc resonant converters," in *2019 IEEE Energy Conversion Congress and Exposition (ECCE)*, pp. 660–665, 2019.

[115] Y.-H. Hsieh and F. C. Lee, "Accurate small-signal modeling for charge-controlled llc resonant converter," in *2021 IEEE Energy Conversion Congress and Exposition (ECCE)*, pp. 3052–3059, 2021.

[116] M. Mohammadi, F. Degioanni, M. Mahdavi, and M. Ordonez, "Small-signal modeling of llc converters using homopolarity cycle," *IEEE Transactions on Power Electronics*, vol. 35, no. 4, pp. 4076–4093, 2020.

[117] Y. Ai, J. Liu, S. Chen, and C. Pei, "A small-signal modeling method for llc resonant converter based on time-domain correction," *IEEE Transactions on Power Electronics*, vol. 39, no. 9, pp. 10792–10806, 2024.

[118] Z. Li, R. Mirzadarani, M. G. Niasar, M. Itraj, L. van Lieshout, P. Bauer, and Z. Qin, "Medium-Voltage Solid-State Transformer Design for Large-Scale H 2 Electrolyzers," *IEEE Open Journal of Power Electronics*, 2024.

[119] R. Mirzadarani, Z. Li, Z. Qin, P. Vaessen, P. Bauer, and M. G. Niasar, "Symmetrical Transformer for Medium-Voltage Medium-Frequency ISOP Three-Phase LLC SST," in *2024 IEEE 10th International Power Electronics and Motion Control Conference (IPEMC2024-ECCE Asia)*, pp. 3246–3251, IEEE.

[120] T. Guillod, "Equation-Based Baseline Models." IEEE MagNet Challenge Webinar, May 2023.

[121] H. Li, D. Serrano, S. Wang, and M. Chen, "MagNet-AI: Neural Network as Datasheet for Magnetics Modeling and Material Recommendation," *IEEE Transactions on Power Electronics*, vol. 38, no. 12, pp. 15854–15869, 2023.

[122] D. S. e. al., "Why MagNet: Quantifying the Complexity of Modeling Power Magnetic Material Characteristics," *IEEE Transactions on Power Electronics*, vol. 38, no. 11, pp. 14292–14316, 2023.

[123] H. L. e. al., "How MagNet: Machine Learning Framework for Modeling Power Magnetic Material Characteristics," *IEEE Transactions on Power Electronics*, vol. 38, no. 12, pp. 15829–15853, 2023.

[124] S. Quondam Antonio, F. Riganti Fulginei, A. Laudani, A. Faba, and E. Cardelli, "An effective neural network approach to reproduce magnetic hysteresis in electrical steel under arbitrary excitation waveforms," *Journal of Magnetism and Magnetic Materials*, vol. 528, p. 167735, 2021.

[125] C. Grech, M. Buzio, M. Pentella, and N. Sammut, "Dynamic Ferromagnetic Hysteresis Modelling Using a Preisach-Recurrent Neural Network Model," *Materials*, vol. 13, no. 11, p. 2561, 2020.

[126] N. Rasekh, J. Wang, and X. Yuan, "Artificial Neural Network Aided Loss Maps for Inductors and Transformers," *IEEE Open Journal of Power Electronics*, vol. 3, pp. 886–898, 2022.

[127] X. Liu, M. Wei, M. Qiu, S. Yang, D. Cao, X. Lyu, and Y. Li, "Convolutional Neural Network (CNN) based Planar Inductor Evaluation and Optimization," in *2022 IEEE Applied Power Electronics Conference and Exposition (APEC)*, pp. 1506–1511.

[128] J. Deng, W. Wang, P. Venugopal, J. Popovic, and G. Rietveld, "Knowledge-aware Artificial Neural Network for Loss Modeling of Planar Magnetic Components," in *2022 IEEE Energy Conversion Congress and Exposition (ECCE)*, pp. 1–6.

[129] J. Deng, W. Wang, Z. Ning, P. Venugopal, J. Popovic, and G. Rietveld, "High-Frequency Core Loss Modeling Based on Knowledge-Aware Artificial Neural Network," *IEEE Transactions on Power Electronics*, vol. 39, no. 2, pp. 1968–1973, 2024.

[130] D. Santamargarita, G. Salinas, D. Molinero, E. J. Bueno, and M. Vasić, "Tradeoff Between Accuracy and Computational Time for Magnetics Thermal Model Based on Artificial Neural Networks," *IEEE Journal of Emerging and Selected Topics in Power Electronics*, vol. 11, no. 6, pp. 5658–5674, 2023.

[131] D. Santamargarita, D. Molinero, E. Bueno, M. Marrón, and M. Vasić, "On-Line Monitoring of Maximum Temperature and Loss Distribution of a Medium Frequency Transformer Using Artificial Neural Networks," *IEEE Transactions on Power Electronics*, vol. 38, no. 12, pp. 15818–15828, 2023.

[132] X. Shen, H. Wouters, and W. Martinez, "Deep Neural Network for Magnetic Core Loss Estimation using the MagNet Experimental Database," in *2022 24th European Conference on Power Electronics and Applications (EPE'22 ECCE Europe)*, pp. 1–8.

[133] E. A. Juarez-Balderas, J. Medina-Marin, J. C. Olivares-Galvan, N. Hernandez-Romero, J. C. Seck-Tuoh-Mora, and A. Rodriguez-Aguilar, "Hot-Spot Temperature Forecasting of the Instrument Transformer Using an Artificial Neural Network," *IEEE Access*, vol. 8, pp. 164392–164406, 2020.

[134] X. Shen and W. Martinez, "Machine Learning Model for High-Frequency Magnetic Loss Predictions Based on Loss Map by a Measurement Kit," in *2023 25th European Conference on Power Electronics and Applications (EPE'23 ECCE Europe)*, pp. 1–8.

[135] T. Guillod, P. Papamanolis, and J. W. Kolar, "Artificial Neural Network (ANN) Based Fast and Accurate Inductor Modeling and Design," *IEEE Open Journal of Power Electronics*, vol. 1, pp. 284–299, 2020.

[136] Z. Xiao, Y. Jiang, T. Sun, Y. Wu, and Y. Tang, "Refining Power Converter Loss Evaluation: A Transfer Learning Approach," *IEEE Transactions on Power Electronics*, vol. 39, no. 4, pp. 4313–4324, 2024.

[137] M. Chen, D. Serrano, and H. Li, "MagNet AI for Research, Education and Design." https://mag-net.princeton.edu/, 2023. Accessed: Dec. 30, 2023.

[138] Y. Yu, X. Si, C. Hu, and J. Zhang, "A review of recurrent neural networks: LSTM cells and network architectures," *Neural computation*, vol. 31, no. 7, pp. 1235–1270, 2019.

[139] K. Cho, B. Van Merriënboer, C. Gulcehre, D. Bahdanau, F. Bougares, H. Schwenk, and Y. Bengio, "Learning phrase representations using RNN encoder-decoder for statistical machine translation," *arXiv preprint arXiv:1406.1078*, 2014.

[140] S. Roth, A. Gepperth, and C. Igel, "Multi-objective neural network optimization for visual object detection," *Multi-Objective Machine Learning*, pp. 629–655, 2006.

[141] T. Akiba, S. Sano, T. Yanase, T. Ohta, and M. Koyama, "Optuna: A next-generation hyperparameter optimization framework," in *Proceedings of the 25th ACM SIGKDD international conference on knowledge discovery data mining*, pp. 2623–2631.

[142] Z. Xu, C. Sun, T. Ji, J. H. Manton, and W. Shieh, "Feedforward and Recurrent Neural Network-Based Transfer Learning for Nonlinear Equalization in Short-Reach Optical Links," *Journal of Lightwave Technology*, vol. 39, no. 2, pp. 475–480, 2021.

[143] C. Tan, F. Sun, T. Kong, W. Zhang, C. Yang, and C. Liu, "A survey on deep transfer learning," in *Artificial Neural Networks and Machine Learning–ICANN 2018: 27th International Conference on Artificial Neural Networks, Rhodes, Greece, October 4-7, 2018, Proceedings, Part III 27*, pp. 270–279, Springer.

[144] M. Chen, E. Deleu, and H. Li, "MagNet Challenge 2023: IEEE PELS-Google-Enphase-Princeton MagNet Challenge." https://github.com/minjiechen/magnetchallenge?tab=readme-ov-file#magnet-challenge-2023, 2023. Accessed: Dec. 30, 2023.

[145] D. P. Kingma and J. Ba, "Adam: A method for stochastic optimization," *arXiv preprint arXiv:1412.6980*, 2014.

[146] A. Paszke, S. Gross, F. Massa, A. Lerer, J. Bradbury, G. Chanan, T. Killeen, Z. Lin, N. Gimelshein, and L. Antiga, "Pytorch: An imperative style, high-performance deep learning library," *Advances in neural information processing systems*, vol. 32, 2019.

[147] Y. Wu, M. Schuster, Z. Chen, Q. V. Le, M. Norouzi, W. Macherey, M. Krikun, Y. Cao, Q. Gao, and K. Macherey, "Google's neural machine translation system: Bridging the gap between human and machine translation," *arXiv preprint arXiv:1609.08144*, 2016.

[148] N. Shawki, R. R. Nunez, I. Obeid, and J. Picone, "On Automating Hyperparameter Optimization for Deep Learning Applications," in *2021 IEEE Signal Processing in Medicine and Biology Symposium (SPMB)*, pp. 1–7.

[149] P. Nair, V. Vakharia, M. Shah, Y. Kumar, M. Woźniak, J. Shafi, and M. Fazal Ijaz, "AI-Driven Digital Twin Model for Reliable Lithium-Ion Battery Discharge Capacity Predictions," *International Journal of Intelligent Systems*, vol. 2024, p. 8185044, 2024.

[150] Y. Li, Z. Xie, S. Yang, and Z. Ren, "A Hybrid Algorithm Based on NSGA-II and MOPSO for Multi-Objective Designs of Electromagnetic Devices," *IEEE Transactions on Magnetics*, vol. 59, no. 5, pp. 1–4, 2023.

[151] S. R. Dubey, S. K. Singh, and B. B. Chaudhuri, "Activation functions in deep learning: A comprehensive survey and benchmark," *Neurocomputing*, 2022.

[152] C. Nwankpa, W. Ijomah, A. Gachagan, and S. Marshall, "Activation functions: Comparison of trends in practice and research for deep learning," *arXiv preprint arXiv:1811.03378*, 2018.

[153] R. Castro, I. Pineda, and M. E. Morocho-Cayamcela, "Hyperparameter tuning over an attention model for image captioning," in *Conference on Information and Communication Technologies of Ecuador*, pp. 172–183, Springer.

[154] J. D. Rodriguez, A. Perez, and J. A. Lozano, "Sensitivity Analysis of k-Fold Cross Validation in Prediction Error Estimation," *IEEE Transactions on Pattern Analysis and Machine Intelligence*, vol. 32, no. 3, pp. 569–575, 2010.

[155] V. Vakharia, V. K. Gupta, and P. K. Kankar, "A comparison of feature ranking techniques for fault diagnosis of ball bearing," *Soft Computing*, vol. 20, pp. 1601–1619, 2016.

Curriculum Vitæ

Zhengzhao Li was born in Hebei, China, in 1996. He received the B.Sc. degree in Electrical Engineering from Tongji University, Shanghai, China, in 2018, and the M.Sc. degree in Electrical Engineering from Shanghai Jiao Tong University, Shanghai, China, in 2021, where his research focused on impedance-based stability analysis and control of power electronic converters in weak grid conditions. From August 2021 to December 2021, he was a research assistant at McMaster University, Hamilton, Canada. He is currently pursuing the Ph.D. degree with the DC Systems, Energy Conversion and Storage Group at Delft University of Technology, Delft, the Netherlands. His research focuses on the design, modelling, and control of solid-state transformers for hydrogen applications.

List of Publications

Journal:

J1. **Z. Li**, R. Mirzadarani, M. G. Niasar, M. Itraj, L. van Lieshout, P. Bauer, and Z. Qin, "Medium-voltage solid-state transformer design for large-scale H_2 electrolyzers," *IEEE Open Journal of Power Electronics*, vol. 5, pp. 936–955, 2024.

J2. **Z. Li**, L. Wang, R. Liu, R. Mirzadarani, T. Luo, D. Lyu, M. G. Niasar, and Z. Qin, "A data-driven model for power loss estimation of magnetic materials based on multi-objective optimization and transfer learning," *IEEE Open Journal of Power Electronics*, vol. 5, pp. 605–617, 2024.

J3. **Z. Li**, R. Mirzadarani, J. van der Weg, W. Heyns, R. van der Sande, M. G. Niasar, A. Shekhar, P. Bauer, and Z. Qin, "A Control Approach for Performance Improvement of MMR-Based SST in H_2 Electrolyzer Applications," *IEEE Journal of Emerging and Selected Topics in Power Electronics*, under review.

J4. R. Mirzadarani, **Z. Li**, Z. Qin, P. Vaessen, P. Bauer, and M. G. Niasar, "Current Balancing Technique for the High-Current Windings of Medium-Frequency Transformers," *IEEE Transactions on Industrial Electronics*, early access.

J5. R. Mirzadarani, **Z. Li**, Z. Qin, and M. G. Niasar, "Partial Discharge Mitigation of Medium-Voltage, Medium-Frequency Dry-Type Transformers Using Semiconductive Screening," *IEEE Open Journal of Power Electronics*, under review.

J6. R. Mirzadarani, L. Bolzonella, **Z. Li**, Z. Qin, P. Vaessen, P. Bauer, and M. G. Niasar, "Medium-Frequency Transformer for SST Applications: Design and Optimization," *IEEE Open Journal of Industrial Electronics*, under review.

J7. M. Chen, H. Li, S. Wang, T. Guillod, D. Serrano, …, Z. Li, …, "MagNet Challenge for Data-Driven Power Magnetics Modeling," *IEEE Open Journal of Power Electronics*, vol. 6, pp. 883–898, 2025.

Award:

A1. **Z. Li**, R. Mirzadarani, R. Liu, L. Wang, T. Luo, D. Lyu, M. G. Niasar, and Z. Qin, "Excellent Innovation Award, 2nd Place," IEEE International Challenge in Design Methods for Power Electronics, awarded by the IEEE Power Electronics Society, 2023.

Conference:

C1. **Z. Li**, Z. Qin, R. Mirzadarani, M. G. Niasar, M. Itraj, L. van Lieshout, and P. Bauer, "Comparison of modular multilevel converter based solid state transformer for AC/DC application," in *IECON 2023–49th Annual Conference of the IEEE Industrial Electronics Society*, 2023, pp. 1–6.

C2. **Z. Li**, R. Mirzadarani, J. van der Weg, W. Heyns, M. G. Niasar, P. Bauer, and Z. Qin, "A Control Approach for Performance Improvement of MMR-Based SST in H_2 Electrolyzer Applications," in *PCIM Europe 2025; International Exhibition and Conference for Power Electronics, Intelligent Motion, Renewable Energy and Energy Management*, Nürnberg, Germany, 2025.

C3. R. Mirzadarani, M. G. Niasar, **Z. Li**, Z. Qin, P. Vaessen, P. Bauer, and L. van Lieshout, "Three-phase medium-voltage medium-frequency transformer for SST in green hydrogen production," in *IECON 2023–49th Annual Conference of the IEEE Industrial Electronics Society*, 2023, pp. 1–6.

C4. R. Liu, D. Zhang, **Z. Li**, P. Bauer, and Z. Qin, "Feature Extraction from Electrochemical Impedance Spectroscopy for State of Health Estimation of Lithium-Ion Batteries Under Different Temperatures," in *2024 IEEE 10th International Power Electronics and Motion Control Conference (IPEMC2024-ECCE Asia)*, 2024, pp. 3374–3378.

C5. R. Mirzadarani, **Z. Li**, Z. Qin, P. Vaessen, P. Bauer, and M. G. Niasar, "Symmetrical Transformer for Medium-Voltage Medium-Frequency ISOP Three-Phase LLC SST," in *2024 IEEE 10th International Power Electronics and Motion Control Conference (IPEMC2024-ECCE Asia)*, 2024, pp. 3246–3251.

C6. M. G. Niasar, R. Mirzadarani, F. Muñoz Muñoz, **Z. Li**, Z. Qin, and P. Vaessen, "Exploring 3D-Printed Solutions for Medium-Voltage Insulation Applications," in *2025 24th International Symposium on High Voltage Engineering (ISH)*, 2025.

Patent:

P1. R. Mirzadarani, M. G. Niasar, Z. Qin, and **Z. Li**, "Power Transformer and Method for Current Balancing," filed with the Netherlands Patent Office (NL), status: filed, 2025.

Acknowledgments

Reaching this milestone has been both demanding and fulfilling. I am sincerely thankful to all those who have supported me throughout this journey. Your encouragement, thoughtful guidance, and unwavering support have been instrumental in helping me navigate challenges and arrive at this achievement.

Maliya, my incredible girlfriend, thank you for standing by my side throughout my PhD journey. You were there for me during the happiest moments, and more importantly, through times of sadness, stress, and struggle. Your patience, calmness, and unwavering support taught me how to slow down, stop overthinking the past, and worry less about the future. Without you, I could not have made it through this journey. I am deeply grateful for everything you've done.

Prof. Bauer, I am sincerely grateful for your guidance and support as my promoter throughout my PhD. Your deep expertise, vision, and dedication to the field have been a continual source of motivation. Your trust allowed me the freedom to explore, while your insights helped shape both my research direction and personal development. I truly appreciate the opportunities and encouragement you have generously offered along the way.

Zian, it has been a true pleasure to have you as my supervisor. I feel fortunate to have been selected as the PhD candidate for this unique project, and I have learned so much from you throughout this journey. You have always been kind and approachable, and working with you has felt more like a collaboration between colleagues than a traditional student–supervisor relationship. Your depth of knowledge and quick thinking never cease to impress me—each time I approached you with a technical question, I could almost see your mind racing, far ahead of mine. I am deeply grateful for the opportunities you have given me—through the project, research, and competitions, I've had the chance to collaborate with many people and quickly gain skills across different domains. Thank you for your trust, guidance, and the inspiration you've provided throughout these years.

Mohamad, collaborating with you on this project has been both enjoyable and enriching. Your guidance and insights—both in research and in the practical aspects of the work—have been consistently valuable and deeply appreciated. I have been particularly impressed by your tireless work ethic combined with your energy and enthusiasm, which created a motivating and positive environment. Thank you for your continuous support and for setting a great example through your dedication and engagement.

Reza, you are one of the most positive and energetic people I have ever worked with, and it has been a real pleasure collaborating with you on project, research topics, and competition. Your dedication and work ethic—often working more hours than most people—have been truly inspiring. We've shared many enjoyable and rewarding moments, and even when we occasionally disagreed or had heated discussions, we could always speak openly and resolve issues quickly. I deeply appreciate your honesty, drive, and the strong sense of teamwork you bring.

Yawen, one of the things I feel truly fortunate about during my PhD journey is having you as a friend and colleague. From our first meeting, I sensed your sincerity, warmth, and willingness to help others without hesitation. Talking to you has always been uplifting—your calm and positive energy helped me stay grounded during stressful times. You are hardworking, focused, and solution-oriented, never letting overthinking get in the way. Your mindset and attitude have been a source of inspiration for me throughout these years.

Sohrab, you are the most cheerful presence in our office room 700. It's been a real pleasure sharing the space with you—your positivity has been a constant source of inspiration throughout my journey.

Lu, it has been both a pleasure and a privilege to work with you and learn from you. I've gained a great deal from you—not only academically, but also in practical matters like financial advice, which has been unexpectedly helpful. You are someone who clearly knows what you want and has the determination to pursue it. Our conversations have often brought me relief and clarity, and have helped me feel more confident about my future direction.

Junjie, I truly admire your dedication—you're one of the most committed and driven people I've ever met. You not only have a clear goal, but also the determination to pursue it with everything you have. I have no doubt you'll achieve your academic, career, and life ambitions. And when you get supercar(s), please don't forget to save me a seat!

Ruijun, I sincerely admire your high scientific standards and the excellent quality of your research. You are very hardworking and determined. I am also very grateful for all the help you have given me, especially your support during my surgery in the U.S. I truly admire the rich and colorful life you lead beyond research and study. It has been a great pleasure working with you and attending conferences together. I am confident that you will achieve outstanding success in your career.

Yang, I truly enjoyed all the dinners, BBQs, and trips we shared in the U.S.—those moments have become some of my favorite memories. Beyond that, our conversations in the corridors and common room have always been relaxing and encouraging. I'm especially grateful for your help and care when I had surgery in the U.S.—your support during that time meant a lot to me. Your positivity, dedication, and sincerity have left a lasting impression—I'm excited to see where your path takes you next.

Weichuan, thank you for our interactions and exchanges during my doctoral studies. I sincerely appreciate your time, support, and valuable input, and I wish you every success in your future career.

Jundong, I've truly enjoyed working together in the lab and sharing meals in the cafeteria—we had many joyful moments. With your capabilities and dedication, I'm confident you'll achieve academic success and find a highly fulfilling job in the future.

Robin, your help in the lab was truly invaluable—without you, my experiments would have easily taken two or three times longer. You are an exceptionally thoughtful and capable researcher, a quick thinker and an even faster doer; I still remember watching you assemble a complete banana connector while walking from one room to another, finishing it before we even arrived. I wish you all the best in your future endeavors.

Jonas, you were the first—and so far the only—master's student I've had the chance to work with, and it was truly a pleasure. I was impressed by the speed and efficiency with which you approached and solved problems. I wish you every success in your future career

in Germany.

Sharmila, thank you for your consistent kindness and support in helping me handle various administrative matters. Your patience, understanding, and efficiency in responding to my many requests made a real difference during my PhD. I truly appreciate your help, especially amidst your busy schedule.

Mladen, **Joris**, **Bart**, and **Harrie**, thank you for your assistance with the experimental setup. Your technical expertise, problem-solving mindset, and dedication were invaluable.

Dingsihao, your lifestyle and work ethic are truly inspiring. I'm also very grateful for your guidance and support regarding my career. **Hitesh**, whether in the lab or during chats, I always appreciated your thoughtful perspective and the engaging conversations we shared. **Shibo**, I really enjoyed our trip to Denmark together. **Ao**, I admire your outstanding academic ability, and I am confident that you will thrive in your PhD journey ahead. **Fan**, you are a very kind and generous friend. Thank you for all the help and kindness you have shown me. **Heshi**, thank you for sharing your knowledge of bodybuilding. I am confident that you will become an expert in solid-state transformers. **Yichao**, it was a pleasure traveling with you in the United States. Fingers crossed that your fortune-telling for me will turn out to be accurate. **Haoyuan**, **Yongpeng**, and **Guangyao**, it was a pleasure having lunches and chatting with you in the common room. I'm grateful for your company and the light moments we shared. **Adnan**, I truly admire your resilience and inner drive. I have no doubt that your persistence will lead you to a successful future. **Julian**, it's always a joy to run into you in the corridor or lab—you're an inspiring presence. **Nikos**, I really enjoyed the time we spent together in China. **Calvin**, thank you for your kindness and for your help in the laboratory.

Jarno, **Werner**, **Mahesh**, **Lou**, and **Remco**, colleagues from VONK, it has been a pleasure working with you throughout the entire FlexH2 project. Our collaboration covered all phases of the project, from conceptual discussions to implementation and validation. Your strong industrial perspective and many insightful ideas significantly influenced the development of key concepts and innovative aspects of the work, while your active involvement in their realization and validation helped ensure both technical soundness and practical relevance. Working with you greatly strengthened the link between academic research and industrial application. I wish you all the best in your future endeavors.

Songda, **Lucia**, **Dhanashree**, **Reza**, and **Yin**, colleagues from Shell, it has been a pleasure working with you and receiving your guidance throughout the FlexH2 project. During the project implementation and deployment phases, your probing questions, extensive domain knowledge, and constructive feedback consistently helped clarify key concepts and identify practical constraints. These interactions not only promoted me to think more critically, but also played an important role in refining the execution of the project and improving both the research quality and its real-world relevance.

Zheran, colleague from TU Eindhoven, I truly admire your dedication, work ethic, and capabilities. I learned a lot from you during the project, and I'm confident that you will achieve excellent research outcomes and a successful career.

Chengqi, I truly admire your courage and determination to pivot and move forward in your career. Your capability and drive are inspiring, and I have no doubt you'll make a real impact at Tesla.

Colleagues from ABB, **DNV**, **GE Vernova**, **TKF**, and **TNO**, thank you for the in-

spiring discussions during the FlexH2 meetings. They have greatly helped me deepen my understanding of the subject matter.

The DCES group has been a big, supportive team where everyone cares for and helps one another. I am genuinely grateful to have been part of this warm and inspiring environment. My heartfelt thanks to **Laura**, **Jianning**, **Gautham**, **Aditya**, **Sebastián**, **Hani**, **Wenli**, **Ibrahim**, **Gautam**, **Joel**, **Sachin**, **István**, **Felipe**, **Zichen**, **Rohan**, **Carina**, **Faezeh**, **Koen**, **Alvaro**, **Margo**, **Farshid**, **Bagas**, **Manfredo**, **Leila**, **Siddhesh**, **Sourabh**, **Darío**, **Abdourahim**, **Tayebeh**, **Shadi**, **Hossein**, **Christoforos**, and **Yiannis**.

Gangwei, **Miad**, **Francesca**, **Marco**, **Wiljan**, and **Yunhe**, it was a pleasure to be your colleague in the group. I'm certain you'll bring great value and make a meaningful contribution in your next roles.

Zhifeng, **Xuliang**, **Yu**, **Muhammad**, **Jawad**, and **Tiantian**, it was nice getting to know you and sharing good moments together.

I owe the completion of this journey to the unconditional love and unwavering support of my family. **To my mom and dad**: your trust in me, your continuous encouragement, and the many sacrifices you've made have laid the foundation for everything I've achieved. I am especially thankful for the understanding and strength you offered during the difficult period after I completed my master's degree in China and before I left for the Netherlands. That time was particularly challenging, and your presence gave me the courage to keep moving forward. Being home always brings me a sense of calm—like returning to a safe harbour. Though I was able to visit China twice during my PhD, I started missing your cooking the very next day after returning to the Netherlands. Your belief in me has been a quiet force, pushing me through moments of doubt. This journey has been long and difficult, but your support has never wavered. For that, I am deeply grateful. This achievement is not mine alone; it belongs to you as well.

There are far too many people to name individually, but if you're reading this, I hope you know that I am sincerely grateful to you. Your kindness, guidance, and encouragement have left a lasting impact on my journey.

Zhengzhao
Delft, Nov 2025